MULTI-SCALE MODELING OF THERMOCHEMICAL BEHAVIOR OF NANO-ENERGETIC MATERIALS

A Dissertation
Presented to
The Academic Faculty

by

Dilip Srinivas Sundaram

In Partial Fulfillment
of the Requirements for the Degree
Doctor of Philosophy in the
School of Aerospace Engineering

Georgia Institute of Technology
December 2013

MULTI-SCALE MODELING OF THERMOCHEMICAL BEHAVIOR OF NANO-ENERGETIC MATERIALS

Approved by:

Dr. Vigor Yang, Advisor
School of Aerospace Engineering
Georgia Institute of Technology

Dr. Timothy C. Lieuwen
School of Aerospace Engineering
Georgia Institute of Technology

Dr. Jerry M. Seitzman
School of Aerospace Engineering
Georgia Institute of Technology

Dr. Richard A. Yetter
Department of Mechanical and Nuclear Engineering
The Pennsylvania State University

Dr. Jechiel I. Jagoda
School of Aerospace Engineering
Georgia Institute of Technology

Date Approved: July 15, 2013

ACKNOWLEDGEMENTS

This work was supported by Air Force Office of Scientific Research (AFOSR) under contract number FA9550-11-1-0002. The support and encouragement of Dr. Mitat Birkan is greatly appreciated.

I wish to express my heartfelt thanks to my thesis advisor Prof. Vigor Yang for his valuable guidance, continuous support and encouragement throughout the course of this work. His rigorous pursuit of perfection, true interest in student's well-being, responsiveness, and super-active work style are model attributes that I will aspire to in my life. I would also like to thank Profs. Jerry Seitzman, Jechiel Jagoda, Timothy Lieuwen, and Richard Yetter for agreeing to serve on my thesis committee and providing helpful comments on the work.

Special thanks to Prof. Seitzman for his important contributions to my education at Georgia Tech. I appreciate his help in sending the lectures and arranging special midterm exams during my stay in India in 2009. I was also fortunate to take two of his courses (Kinetics and Thermodynamics of Gases and Gas Dynamics). His contagious inquisitiveness, patient and helpful discussions during and after the coursework transformed my approach towards scientific research. I would also like to thank Prof. Jagoda, Margaret Ojala, Susan Jackson, and staff of School of Aerospace Engineering for their patient assistance at numerous occasions during my studies at Georgia Tech.

I wish to thank Prof. Richard Yetter for his support, helpful feedback, and comments over the last six years. Thanks to Prof. Grant Risha and Terry Connell for their help.

Numerous thanks to Drs. Piyush Thakre and Puneesh Puri for showing me the door to Prof. Yang’s group and helping me during the early stages of my Ph.D. program. I would also like to thank my colleagues and friends for their support and help.

TABLE OF CONTENTS

CHAPTER

LIST OF TABLES

LIST OF FIGURES

LIST OF SYMBOLS AND ABBREVIATIONS

a	lattice constant
A	surface area
B	particle mass density
C_p	specific heat
d	diameter, scaled position vector
D	diffusion coefficient, diameter
D_o	pre-exponential constant
E	mechanical energy
E_A	activation energy
E_c	cohesive energy
F	force
f	fraction of exposed core area/surface atoms
H	Hamiltonian, enthalpy
h	Planck’s constant, enthalpy
h_{fg}	enthalpy of water vaporization
h_{sl}	enthalpy of melting of ice
i	stoichiometric fuel-air mass ratio
I	radiation intensity
K	kinetic energy
k	chemical rate constant
k_a	absorption coefficient
k_s	scattering coefficient

k_t	extinction coefficient
Kn	Knudsen number
L	Lagrangian
l_1	vapor zone thickness
l_2	liquid zone thickness
L_{fus}	latent heat of fusion
M	molecular weight, mass, fictitious mass
m	mass, refraction index
MW	molecular weight
N	number of atoms
N_A	Avogadro's number
N_p	particle number density
N_{step}	number of time integration steps
p	momentum, pressure, vapor pressure
Q	energy, heat
Q_a	absorption efficiency
Q_s	scattering efficiency
q	generalized coordinate, heat loss rate, radiation heat source
R	outer radius, gas constant, radius
r	inner radius, position vector, radius
r_b	burning rate
t	time, thickness
T	temperature
U	potential energy
v	velocity

V	volume
X	concentration, mole fraction
x	position vector, spatial coordinate
X_{eff}	effective oxidizer concentration
Y	mass fraction
y	normalized spatial coordinate

Greek

γ	adiabatic constant
ε	emissivity
μ	normalized heat release rate, molar mass
η	normalized particle size
θ	normalized temperature
δ	oxide layer thickness, Lindemann index
σ	surface tension, Stefan-Boltzmann constant, size parameter
α	thermal diffusivity, accommodation coefficient
λ	translational order parameter, thermal conductivity, mean free path
Φ	volume fraction
ψ	wave function
τ_b	burn time
δ_s	shell thickness
δ_t	thermal displacement
Λ_{th}	Debroglie wavelength
δ_v	liquid zone thickness
ρ	density

Subscripts

ad	adiabatic
am	amorphous
b	bulk, burn, boiling, black body
c	conduction, core
ch	chemical
cm	center of mass
d	diffusion
e	external
f	flame, fluid
g	gas
G	gaseous reaction zone
I	ice
i	interface, atom index
ign	ignition
kin	kinetics
lw	liquid water
m	melting, mixture
mol	molecular
ox	oxidation, oxidizer, oxide
p	particle
$prod$	products
r	radiation, reaction
$reac$	reactants
s	shell

u	unburned
v	vapor, vaporization
V	water vapor zone
vap	vaporization
w	water
W	liquid water zone
wv	water vapor

SUMMARY

Conventional energetic materials which are based on monomolecular compounds such as trinitrotoluene (TNT) have relatively low volumetric energy density. The energy density can be significantly enhanced by the addition of metal particulates. Among all metals, aluminum is popular because of its high oxidation enthalpy, low cost, and relative safety. Micron-sized aluminum particles, which have relatively high ignition temperatures and burning times, have been most commonly employed. Ignition of micron-sized aluminum particles is typically achieved only upon melting of the oxide shell at 2350 K, thereby resulting in fairly high ignition delay. Novel approaches to reduce the ignition temperatures and burning times and enhance the energy content of the particle are necessary.

Recently, there has been an enormous interest in nano-materials due to their unique physicochemical properties such as lower melting and ignition temperatures and shorter burning times. Favorably, tremendous developments in the synthesis technology of nano-materials have also been made in the recent past. Several metal-based energetic materials with nano-sized particles such as nano-thermites, nano-fluids, and metalized solid propellants are being actively studied. The “green” reactive mixture of nano-aluminum particles and water/ice mixture (ALICE) is being explored for various applications such as space and underwater propulsion, hydrogen generation, and fuel-cell technology. Strand burning experiments indicate that the burning rates of nano-aluminum and water mixtures surpass those of common energetic materials such as ammonium

dinitramide (ADN), hydrazinium nitroformate (HNF), and cyclotetramethylene tetranitramine (HMX). Sufficient understanding of key physicochemical phenomena is, however, not present. Furthermore, the most critical parameters that dictate the burning rate have not been identified. A multi-zone theoretical framework is established to predict the burning properties and flame structure by solving conservation equations in each zone and enforcing the mass and energy continuities at the interfacial boundaries. An analytical expression for the burning rate is derived and physicochemical parameters that dictate the flame behavior are identified. An attempt is made to elucidate the rate-controlling combustion mechanism. The effect of bi-modal particle size distribution on the burning rate and flame structure are investigated. The results are compared with the experimental data and favorable agreement is achieved.

The ignition and combustion characteristics of micron-sized aluminum particles can also be enhanced by replacing the inert alumina layer with favorable metallic coatings such as nickel. Experiments indicate that nickel-coated aluminum particles ignite at temperatures significantly lower than the melting point of the oxide film, 2350 K due to the presence of inter-metallic reactions. Nickel coating is also attractive for nano-sized aluminum particles due to its ability to maximize the active aluminum content. Understanding the thermo-chemical behavior of nickel-aluminum core-shell structured particles is of key importance to both propulsion and material synthesis applications. The current understanding is, however, far from complete. In the present study, molecular dynamics simulations are performed to investigate the melting behavior, diffusion characteristics, and inter-metallic reactions in nickel-coated nano-aluminum particles. Particular emphasis is on the effects of core size and shell thickness on all important phenomena. The properties of nickel-coated aluminum particles and aluminum-coated nickel particles are also compared.

Considerable uncertainties pertaining to the ignition characteristics of nano-aluminum particles exist. Aluminum particles can spontaneously burn at room temperature, a phenomenon known as pyrophoricity. This is a major safety issue during particle synthesis, handling, and storage. The critical particle size below which nascent particles are pyrophoric is not well known. Energy balance analysis with accurate evaluation of material properties (including size dependent properties) is performed to estimate the critical particle size for nascent particles. The effect of oxide layer thickness on pyrophoricity of aluminum particles is studied. The ignition delay and ignition temperature of passivated aluminum particles are also calculated. Specific focus is placed on the effect of particle size. An attempt is made to explain the weak dependence of the ignition delay on particle size at nano-scales.

CHAPTER 1

INTRODUCTION

1.1 Metal-Based Energetic Materials

Energetic materials liberate large amounts of chemical energy in the form of heat upon combustion. The fuel and oxidizer groups may be present within a single molecule (Tillotson et al. 2001). A common example of such monomolecular energetic materials is trinitrotoluene (TNT). Figure 1.1 shows the chemical structure of TNT. Chemical kinetics can control the rate of energy release, since the fuel and oxidizer groups are chemically linked (Tillotson et al. 2001). This results in a fairly high rate of energy release. The volumetric energy densities of monomolecular energetic materials are, however, significantly limited. Energetic materials can also be prepared by physical mixing of fuel

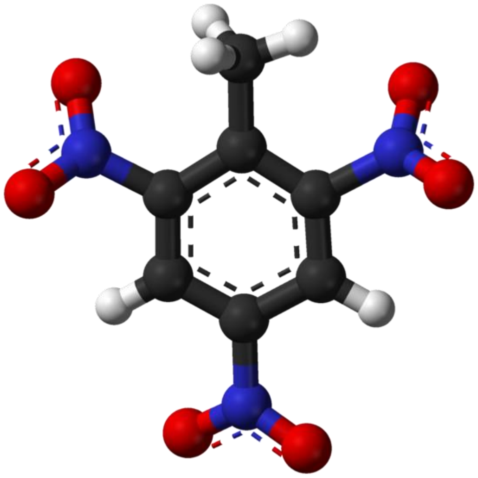

Figure 1.1: Chemical structure of trinitrotoluene (TNT) (Red – oxygen, blue – nitrogen, black – carbon, white – hydrogen) (Mills 2009).

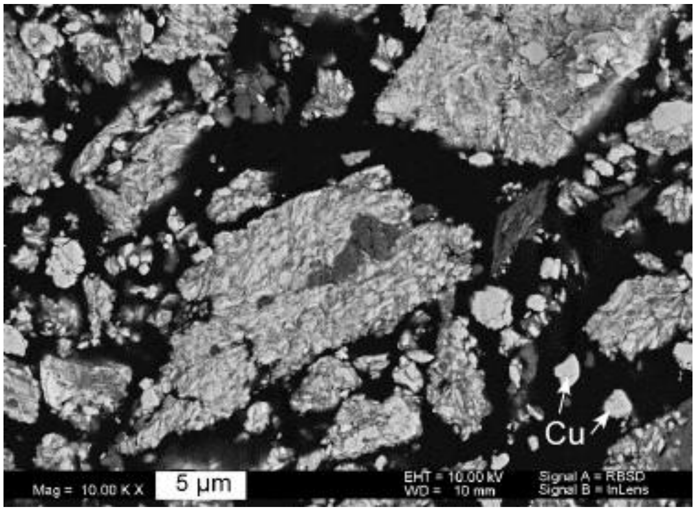

Figure 1.2: High magnification scanning electron microscopy image of nanocomposite consisting of aluminum (dark) and copper oxide (bright) particles synthesized using arrested reactive milling (Umbrajkar, Schoenitz & Dreizin 2006).

and oxidizer entities (particles). Figure 1.2 shows the nano-composite consisting of aluminum and copper oxide particles after milling time of 60 minutes (Umbrajkar, Schoenitz & Dreizin 2006). The combustion of composite energetic materials can be controlled by mass transport phenomena, since the fuel and oxidizer particles are separate entities (Tillotson et al. 2001). The resulting energy release rate is lower than the corresponding value that could be attained in a kinetically-controlled process. The addition of metal particles increases the overall energy density of the mixture. Figure 1.3 shows the energy densities of various monomolecular energetic materials and metals (Dreizin 2009). The energy densities of metals are typically greater than those of monomolecular compounds. Metals such as beryllium, boron, and aluminum have relatively high enthalpy of combustion. Beryllium is seldom used due to its toxicity, relative scarcity, and high cost (Sutton & Biblarz 2010). Among all the metals, boron has

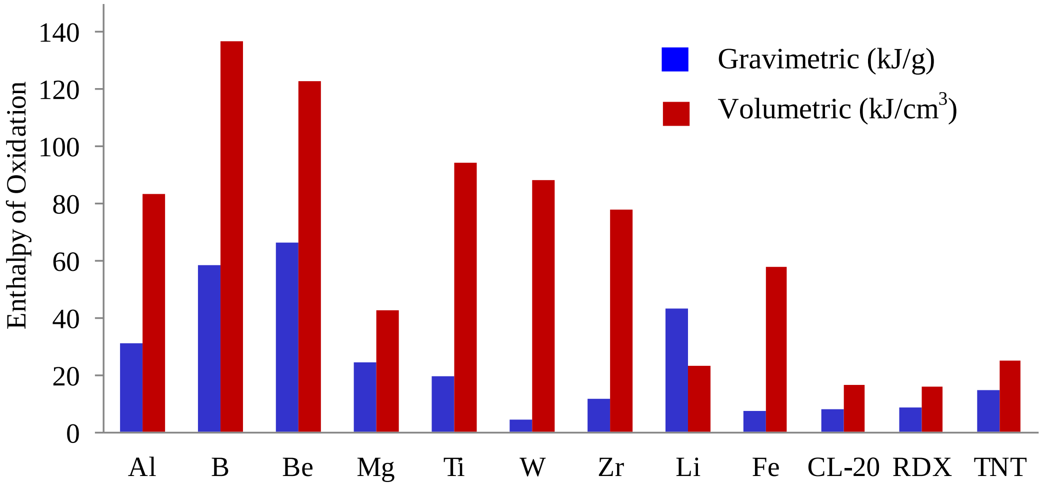

Figure 1.3: Volumetric and gravimetric heats of oxidation of monomolecular energetic materials and metals (adapted from Dreizin 2009).

the highest volumetric energy density. Combustion of boron particles must occur heterogeneously at the particle surface due to the high boiling point of boron, 4139 K (Young et al. 2009). The reaction is further inhibited due to the formation of meta-stable HBO_2 species (Young et al. 2009). As a result, the application of boron particles in propulsion and energy-conversion devices has been limited. Aluminum is the most abundant metal and is relatively safe to use. Micron-sized aluminum particles have been used extensively in propulsion, explosion, and pyrotechnic applications due to their high oxidation enthalpy, relative safety, and low cost (Price & Sigman 2000). Recently, nanoaluminum particles are being studied with renewed interest due to their favorable physicochemical properties and rapid progress in the synthesis technology (Yetter, Risha & Son 2009). In the following sections, some of the important concepts pertaining to the ignition and combustion of micro- and nano-sized aluminum particles are discussed in detail.

1.2 Ignition and Combustion of Micron-Sized Aluminum Particles

1.2.1 Alumina-Coated Aluminum Particles

Nascent aluminum particles undergo oxidation reactions spontaneously in room-temperature air, thereby resulting in the formation of a 2-4 nm thick oxide (Al_2O_3) layer (Trunov, Schoenitz & Dreizin 2006). Figure 1.4 shows the scanning electron micrograph of a quenched 210 μm aluminum particle (Bucher, Ernst & Dryer 2000). An oxide layer covering the particle surface is clearly seen. One of the main issues concerning the oxidation of micron-sized aluminum particles is their high ignition temperatures (Huang et al. 2009). Figure 1.5 shows the effect of particle size on the ignition temperature of aluminum particles in oxygenated environments (Puri 2008). Micron-sized particles with diameters greater than 100 μm ignite only upon melting of the oxide shell at 2350 K. The oxide shell convolves to form a cap due to the effects of surface tension, thereby exposing the aluminum core and igniting the particle. The ignition temperature decreases

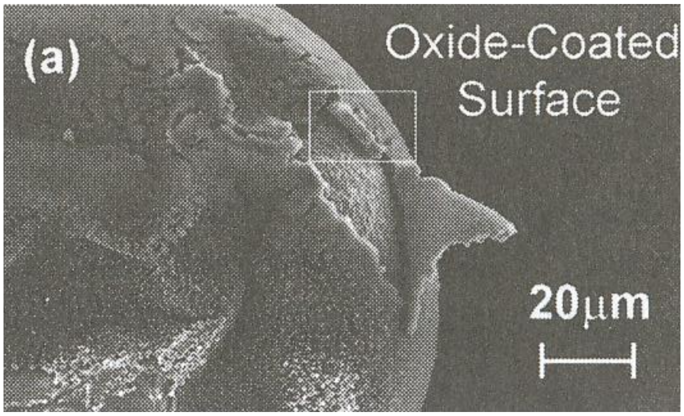

Figure 1.4: Scanning electron micrograph of a quenched 210 μm aluminum particle (Bucher, Ernst & Dryer 2000).

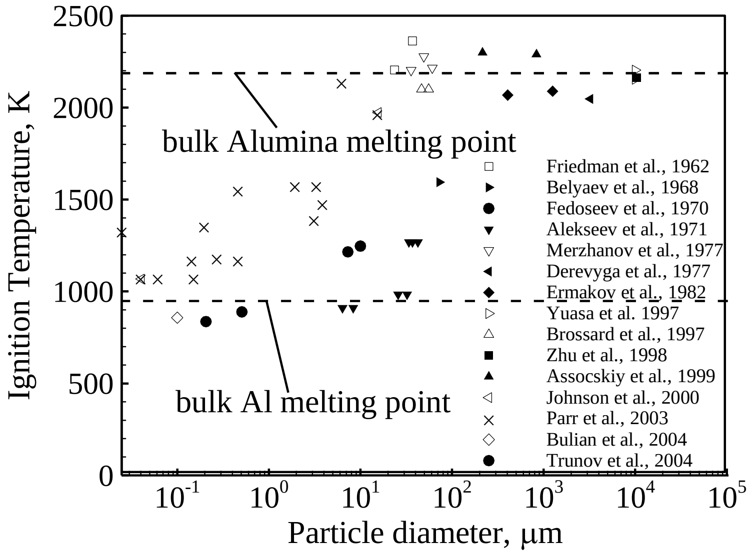

Figure 1.5: Effect of particle size on ignition temperature of aluminum particles in oxygenated environments (Puri 2008).

from a value of 2350 K at 100 µm to 1000 K at 100 nm. Note that the ignition temperature depends on various parameters such as heating rate, concentration of the oxidizer, and particle morphology. As a result, quantitative comparison of the ignition temperatures measured in different experiments is not meaningful. Nevertheless, the observed trend is expected to be qualitatively valid. The size-dependence of the ignition temperature of aluminum particles is explained by the theory of polymorphic phase transformations in the oxide layer (Trunov, Schoenitz & Dreizin 2006). Figure 1.6 shows the sequence of oxidation of 10-14 µm aluminum particles in oxygen obtained using thermo-gravimetric analyzer. The particles were heated at relatively low rates in the range of 5-40 K/min. The oxidation begins with the growth of the natural amorphous oxide layer, which is controlled by the outward diffusion of aluminum cations through the growing oxide layer. The energy of the metal-oxide interface can stabilize the

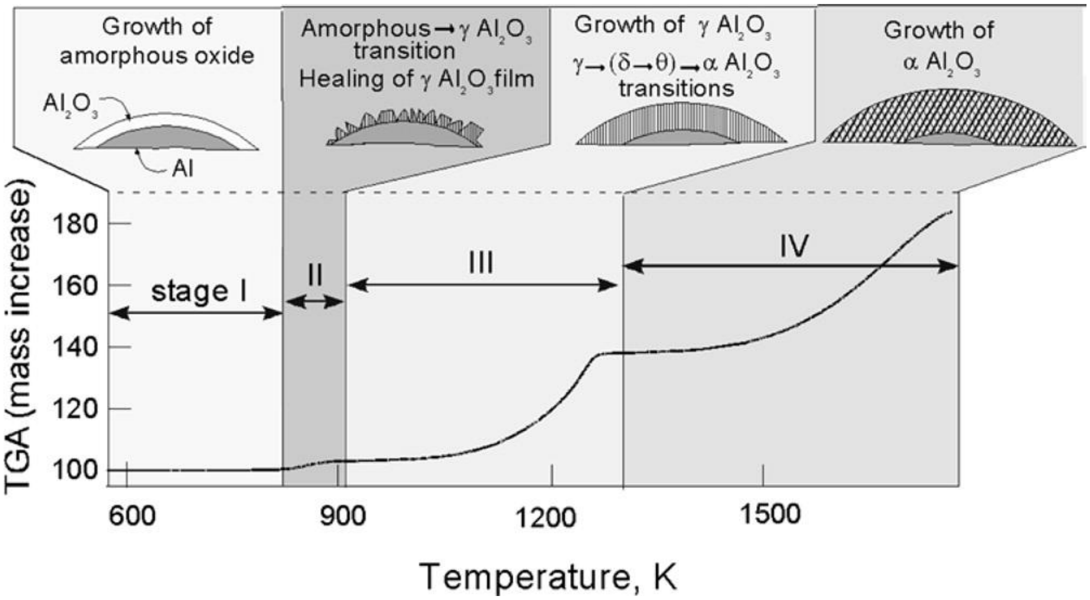

Figure 1.6: Sequence of oxidation of 10-14 μm aluminum particles in oxygen (Trunov, Schoenitz & Dreizin 2006).

amorphous oxide layer only up to a thickness of 5 nm. When the critical thickness is attained or when the temperature is sufficiently high, the amorphous alumina transforms to the γ polymorph. The γ-alumina does not form a continuous covering of the surface due to its higher density. The resulting pores or openings allow direct oxidation of aluminum core, thereby increasing the oxidation rate. The openings in the oxide layer heal while only a small fraction of the metal is oxidized. The rate of oxidation decreases, since the healed oxide layer offers significant diffusion resistance. The growth of γ-alumina layer is followed by transformation of gamma-alpha phase transformation and growth of α-alumina. Nano-sized aluminum particles can ignite due to the chemical energy release as a result of amorphous-gamma phase transformation owing to their lower volumetric heat capacity. Ignition of particles in the intermediate size range is caused by gamma-alpha phase transformation. Micron-sized and larger particles, however, ignite only upon melting of the oxide shell at 2350 K.

Upon ignition, aluminum can vaporize and burn homogenously with the oxidizing gas or undergo heterogeneous reactions at the particle surface. Heterogeneous reactions, which typically occur before ignition, may be the dominant mode of combustion provided metal vaporization cannot take place. Early studies (Von Grosse & Conway 1958, Glassman 1996) identified two relevant issues: (1) volatility of the metal relative to that of its oxide; (2) relationship between the energy required to vaporize the metal and

Table 1.1: Properties of metals and their oxides (Yetter, Risha & Son 2009).

Metal	T_{bp} (K)	Oxide	T_{vol} (K)	$\Delta H_{f,298}$	ΔH_{vol}	$H_{T,vol} - H_{298} + \Delta H_{vol}$
					(kJ/mol)	
Al	2791	$A1_2O_3$	4000	-1676	1860	2550
B	4139	B_2O_3	2340	-1272	360	640
Be	2741	BeO	4300	-608	740	1060
Cr	2952	Cr_2O_3	3300	-1135	1160	1700
Fe	3133	FeO	3400	-272	610	830
Hf	4876	HfO_2	5050	-1088	1014	1420
Li	1620	Li_2O	2600	-599	400	680
Mg	1366	MgO	3350	-601	670	920
Ti	3631	Ti_3O_5	4000	-2459	1890	2970
Zr	4703	ZrO_2	4570	-1097	920	1320

T_{vol} = volatilization temperature of oxide, T_{bp} = metal boiling point at 1atm oxide and the overall heat of the reaction. Table 1.1 shows the properties of different metals and their oxides (Yetter, Risha & Son 2009). The heat of reaction is typically lower than the amount of energy required to heat the oxide to its boiling point and vaporize the oxide. The adiabatic flame temperature is, thus, limited to the boiling point of the oxide. For aluminum, since the boiling point of the metal is lower than that of its oxide, possibility of homogeneous gas-phase combustion exists. Accordingly, Be, Cr, Fe, Hf, Li, Mg, and Ti should also have the ability to burn as vapor-phase diffusion flames at 1 atm in pure O_2. For metals such as boron, although there is sufficient energy to vaporize the oxide, there is insufficient amount of energy to raise the temperature to the boiling point of metal and change its phase. Heterogeneous chemical reactions are, thus, expected to occur. Figure 1.7 shows the observed flame structures for 210 μm aluminum particles burning in air and water vapor environments (Yetter & Dryer 2001). A detached

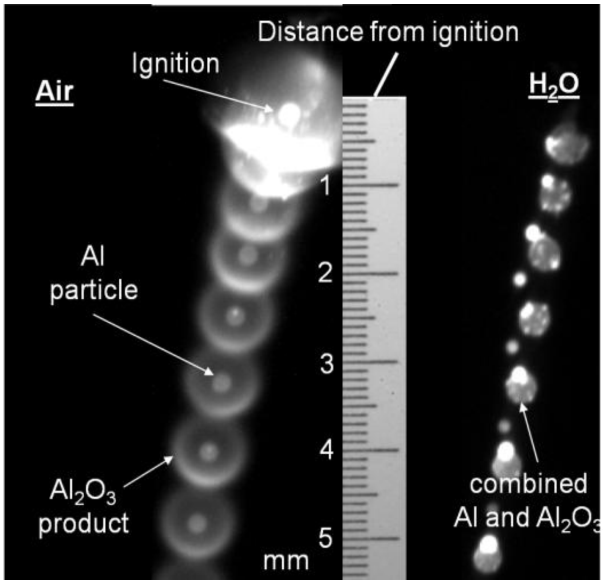

Figure 1.7: Streak photographs of 210 μm aluminum particle burning in air and water vapor environments (Yetter & Dryer 2001).

vapor-phase diffusion flame is seen in air, which is consistent with the Glassman's criterion. Note that an oxide smoke consisting of sub-micron particles surrounds the particle. The gas-phase sub-oxides are transported to the particle by thermophoresis and diffusion, thereby altering the flame structure. The steady-state vapor-phase combustion stage is followed by asymmetric combustion stage, which is characterized by brightness oscillations, jetting, spinning, and particle fragmentation (Dreizin 1996). The combustion of micron-sized aluminum particles is well described by Dreizin's three-stage theory (Dreizin 1996). The presence of a detached diffusion flame is diminished in water vapor environment. Figure 1.8 shows the effect of pressure on the adiabatic flame temperature of aluminum particles in different oxidizers obtained using NASA chemical equilibrium code (Mcbride & Gordon 1996). The flame temperature is lower than the vaporization temperature for pressures over a "cut-off" value. The cut-off pressure is ~ 2, 5, and 70

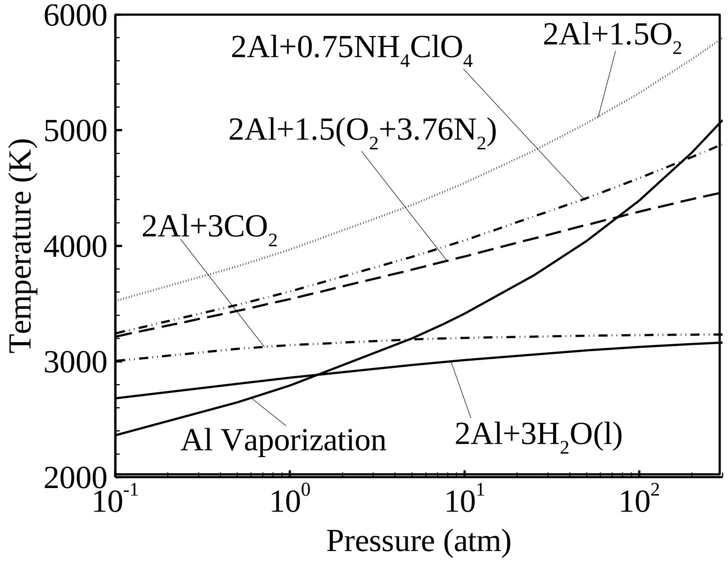

Figure 1.8: Effect of pressure on adiabatic flame temperature of aluminum particles in different oxidizers.

atm for water, carbon dioxide, and air, respectively. It is, thus, not surprising that vapor-phase combustion is more readily observed in air than in water vapor. The rate of combustion of micron-sized aluminum particles is controlled by diffusion of reactant species through the gaseous mixture (Beckstead 2005). One of the important parameters that characterize the combustion of metal particles is the burning time. Beckstead (Beckstead 2005) assimilated numerous experimental data and obtained the following correlation for the burning time of aluminum particles for diameters greater than 20 μm:

$$\tau_b = \frac{c_1 d_p^{1.8}}{X_{eff}\, p^{0.1} T_0^{0.2}}, \tag{1.1}$$

where X_{eff} is the effective oxidizer mole fraction, $X_{eff} = C_{O_2} + 0.6\, C_{H_2O} + 0.22\, C_{CO_2}$, τ_b the burning time in seconds, p the pressure in atm, d_p the particle diameter in μm, T_0 the temperature in Kelvin, and c_1 a constant ($=7.35\times10^{-6}$). Note that the burning time exhibits near quadratic dependence on the particle size and is weakly dependent on the temperature and pressure of the gas. This is consistent with the “diffusion-limited” combustion phenomenon. The relatively poor oxidation characteristics of micron-sized aluminum particles coupled with low rates of energy release in composite energetic materials necessitate the development of novel energetic materials that offer enhanced and controlled energy release rates without compromising the affordability and safety characteristics.

1.2.2 Nickel-Coated Aluminum Particles

Several approaches are available to promote the reactivity of micron-sized aluminum particles. Encapsulation of aluminum particles with a nickel shell is one of the promising methods to enhance the ignition characteristics of aluminum particles

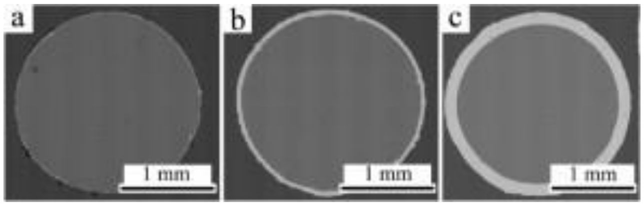

Figure 1.9: SEM images of nickel-coated aluminum particles of diameter 2.38 mm: (a) 6 wt. % Ni, (b) 29 wt. % Ni, and (c) 58 wt. % Ni (Andrzejak, Shafirovich & Varma 2007).

(Andrzejak, Shafirovich & Varma 2007). Particle encapsulation was achieved by cyclic electroplating process. Prior to coating, the particles were treated to remove any aluminum oxide on their surface. Figure 1.9 shows the images of unreacted, cross-sectioned samples obtained using scanning electron microscopy, indicating the presence of uniform nickel coating. Shafirovich et al. (Shafirovich et al. 2005) studied the ignition characteristics of nickel-coated aluminum particles at a pressure of 1 atm using the electrodynamic levitation and furnace setups shown in Fig. 1.10. The electrodynamic levitation setup was used to measure the ignition delay and the furnace setup was employed to measure the ignition temperature of the particles. In the former case, the suspended particles were ignited using a 50-W CO_2-laser with the beam split and focused onto opposite sides of the particle. A video camera and telescope were used to adjust the position of the levitated particle at the focal point of the laser. A photographic multiplier tube measured the light emission intensity of the burning particle, variation of which allowed the determination of the ignition delay. The laser was interrupted when the light emission intensity reaches a threshold, which was fixed to be the same in all the experiments. This facilitated the desired self-sustained burning process. The time from starting the laser to its interruption was defined as the ignition delay. The furnace set up

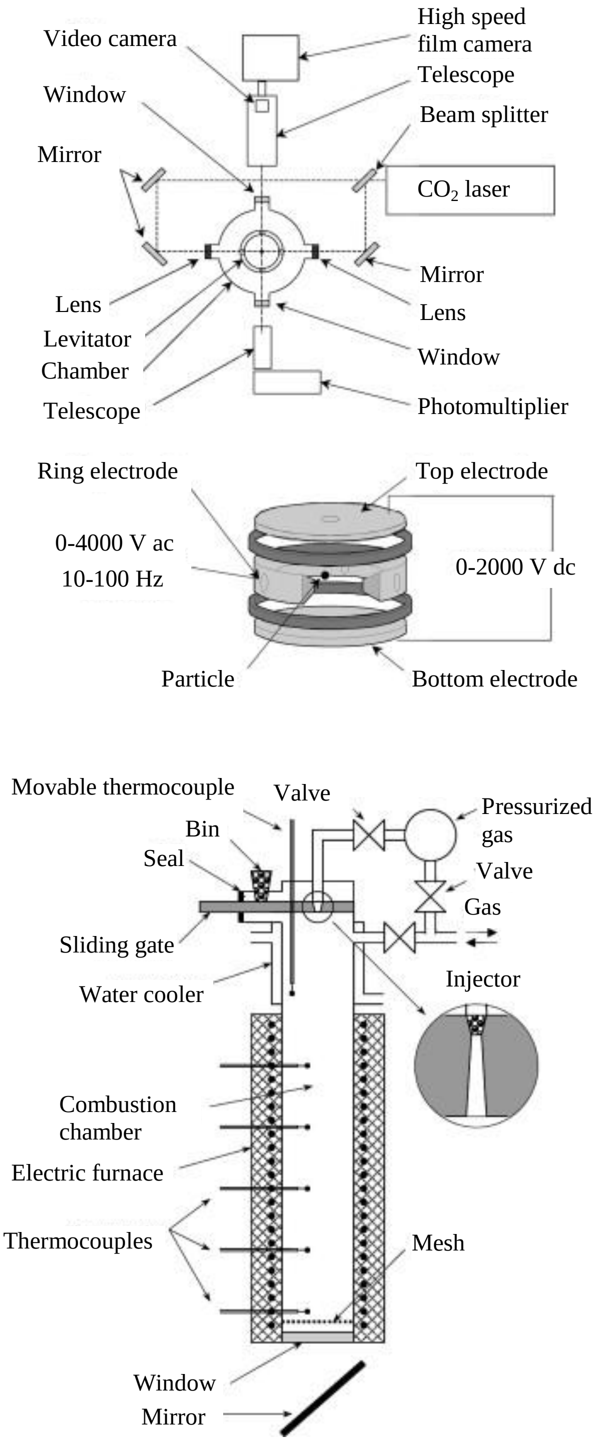

Figure 1.10: Schematic of (a) electrodynamic levitation and (b) furnace setups used to analyze the ignition of nickel-coated aluminum particles (Shafirovich et al. 2005).

consists of a combustion chamber, which is a vertical stainless-steel tube with an inner diameter of 4.8 cm and height of 100 cm. The lower part of tube was placed inside a cylindrical electric furnace, while the upper part of the tube was water-cooled. The bottom of the tube wasclosed by a quartz window protected by a wire mesh to catch the falling particles. The particle injection system, placed in the top part of the chamber, includes a powder bin, a sliding gate with an injector and a 100-ml vessel with a slightly pressurized gas. Prior to the injection of particles, the reactor was evacuated (10^{-2} Torr), filled with the gas, and preheated up to required temperature. Twelve chromel/alumel thermcouples were used to measure temperature at different locations. The critical ignition temperature was defined as the minimum gas temperature at which particles ignite during their fall. The ignition delays were measured for atomized aluminum powders (32-40 μm in size, The Metal Powder Company, Madurai, India), which were nickel-coated at Technion – Israel Institute of Technology. The thickness of the nickel coating was varied in the range of 17-301 nm (0.93-14.4 wt.% Ni). The ignition temperatures were measured for commerically available nickel-coated aluminum particles (100-125 μm in size, Westaim, Canada). The thickness of the nickel coating is ~5 μm. Figure 1.11a shows the effect of mass fraction of nickel in the particle on the ignition delay. The ignition delay decreases with increasing nickel mass fraction in the range of 0-3 % and decreases negligibly with further increase in the nickel content of the particle. Figure 1.11b shows the ignition temperatures of nickel-coated aluminum particles in oxygenated environments as a function of mole fraction of oxygen in gas. The measured ignition temperatures of nickel-coated aluminum particles are substantially lower than those of alumina-coated aluminum particles (2350 K). In another study

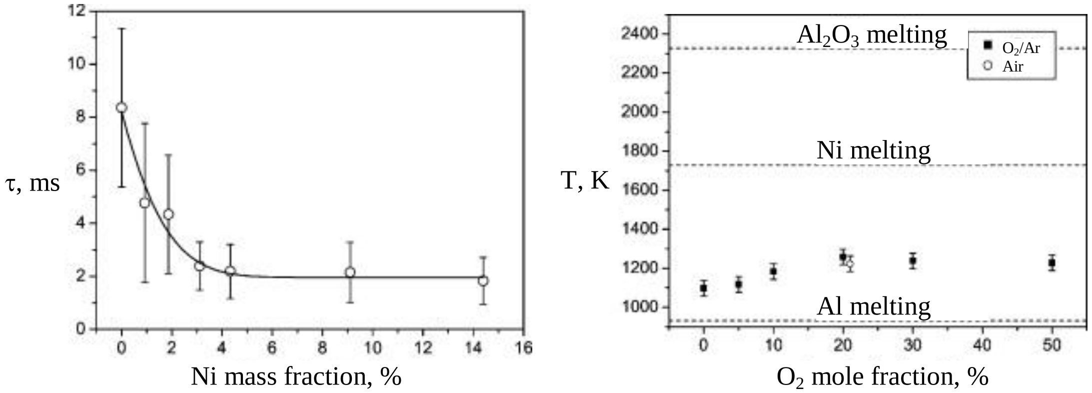

Figure 1.11: (a) Ignition delay of nickel-coated aluminum particles as a function of mass fraction of nickel in the particle; (b) ignition temperature of nickel-coated aluminum particles for varying oxygen mole fraction (Shafirovich et al. 2005).

(Andrzejak, Shafirovich & Varma 2007), the ignition temperature of 2.5 mm nickel-coated aluminum particles was measured to be 1325 °C, irrespective of the ambient gas (Ar or CO_2) and nickel content. Particle ignition was attributed to exothermic inter-metallic reactions between aluminum and nickel atoms and phase transformations of different Ni-Al compounds. Figure 1.12 shows the schematic describing the ignition mechanism of nickel coated aluminum particles. Upon melting of the aluminum core at 660 °C, aluminum-rich $NiAl_3$ is formed along the core-shell interface. Solid Ni_2Al_3 begins to form at temperatures exceeding the melting point of $NiAl_3$ (854 °C). As the temperature surpasses 1133 °C, Ni_2Al_3 melts, allowing the formation of NiAl. NiAl penetrates deep into the solid nickel shell, thereby increasing the interfacial area and igniting the particle. The formation of inter-metallic species and their phase transformation, thus, plays a crucial role in the ignition of nickel-coated aluminum particles. Detailed insight on the underlying physicochemical phenomena can be obtained

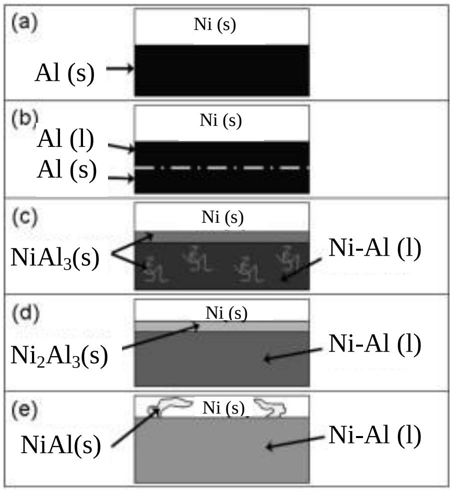

Figure 1.12: Schematic illustrating the ignition mechanism of nickel-coated aluminum particles (Andrzejak, Shafirovich & Varma 2007).

through high fidelity numerical simulations. Another method by which the reactivity of aluminum particles can be enhanced is by the reduction of the particle size from micron to nano-meter scale. In the following section, the physicochemical properties of nano-sized aluminum particles are briefly discussed.

1.3 Nano-Sized Aluminum Particles

Nano particles are studied with renewed interest for propulsion and energy conversion applications due to their favorable physicochemical properties and significant progress in the synthesis technology in the recent past. Particle synthesis involves not only the manufacture of nascent particles but also controlled passivation of these particles. Manufacture of nano-sized particles is an active research field and tremendous progress in the synthesis technology is expected in the near future. Some of the commonly used techniques include electric explosion of wires (Kotov 2003), inert gas condensation (Swihart 2003), combustion synthesis (Woolridge 1998), wet chemistry methods (Turkevich, Stevenson & Hillier 1951), and mechanical milling (Eckert et al. 1993). Detailed discussions on the various synthesis methods are available in Dreizin's review paper (Dreizin 2009).

1.3.1 Size Dependence of Thermophysical Properties

Nano materials have unique physicochemical properties. This can be attributed to the presence of a large number of atoms on the particle surface and excess energy associated with these atoms (Klabunde et al. 1996). Figure 1.13 shows the effect of the particle size on the percentage of atoms on the surface layer of an aluminum particle. It increases from 5 to 50 %, when the particle size decreases from 30 to 3 nm. In a nano-composite energetic material, the reduced diffusion length scale results in higher mass transport rates between the fuel and oxidizer particles. Nano particles have lower melting points than micron-sized counterparts (Puri & Yang 2007). Figure 1.14 shows the effect of particle size on melting temperature of aluminum particles. The melting temperature of aluminum particles takes a value of 400 K at 2 nm, which is significantly lower than the bulk value of 933 K. The experimental data of Eckert et al. (Eckert et al. 1993) and theoretical predictions of Zhang et al. (Zhang, Lu & Jiang 1999) follow a qualitatively similar trend. The ignition temperatures and burning times of nano-sized aluminum particles are also lower than those of micron-sized particles (Huang et al. 2009). Significant enhancements in the burning rates are thus achieved when nano-sized particles are substituted for micron-sized counterparts in the energetic materials (Yetter, Risha & Son 2009).

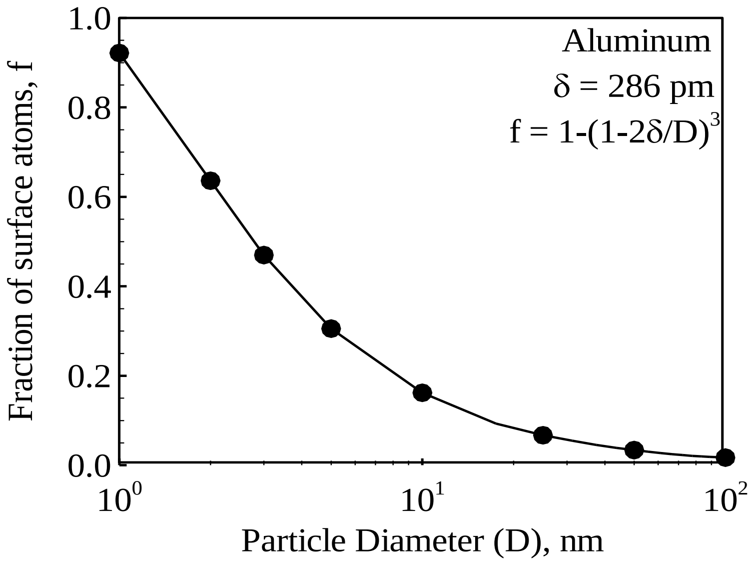

Figure 1.13: Effect of particle size on the fractions of atoms on the surface layer of aluminum particle.

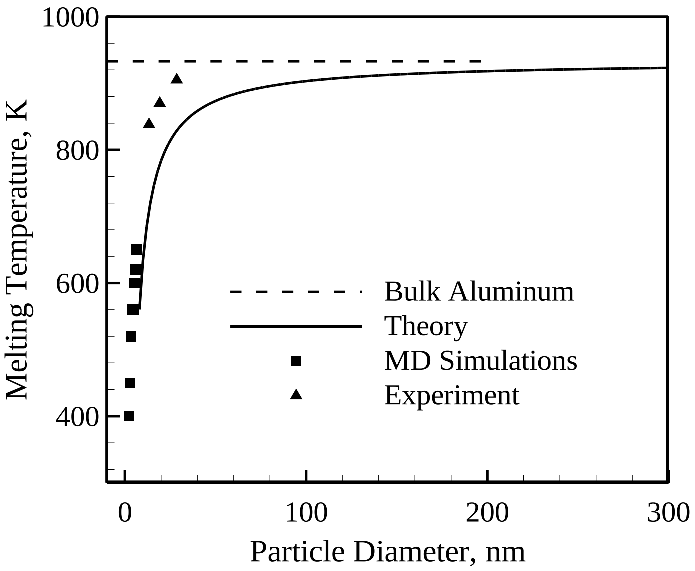

Figure 1.14: Effect of particle size on melting temperature of aluminum particles (Huang et al. 2009).

1.3.2 Ignition and Combustion Characteristics

The ignition and combustion characteristics of nano-aluminum particles are significantly different from those of micron-sized counterparts. Nanoaluminum particles ignite at temperatures as low as 1000 K, which are substantially lower than the ignition temperatures of micron-sized particles (2350 K). Trunov et al. (Trunov, Schoenitz & Dreizin 2006) developed a theoretical model based on the concept of polymorphic phase transformations to calculate the ignition temperature of nano-aluminum particles. The predicted values are greater than the experimental data. For example, the ignition temperature of 100 nm aluminum particle is predicted to be 1250 K, which is greater than the experimental value by ~300 K. The disparity was attributed to the fact that the measured ignition temperatures correspond to a collection of particles (powder) rather than an isolated particle. Further studies are necessary to ascertain if additional physicochemical processes must be considered in the analysis. The predicted values must

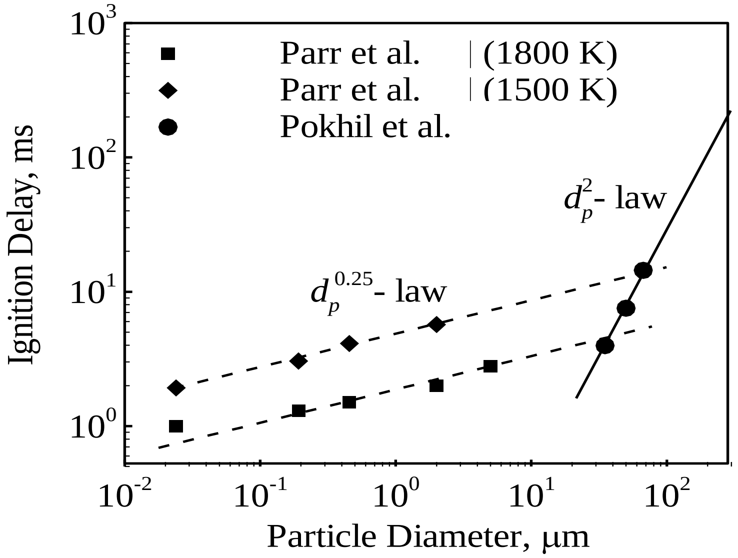

Figure 1.15: Effect of particle size on ignition delay of aluminum particles (Sundaram, Puri & Yang 2013).

also be compared with the experimental data for a wide range of particle sizes. Ignition delay is yet another important property of concern. The effect of particle size on the ignition delay of aluminum particles has not been studied. The available experimental data (Parr et al. 2003, Pokhil, Belyaev & Frolov 1972) can be gathered to plot the ignition delay as a function of particle size. This is shown in Fig. 1.15. For micron-sized particles, the ignition delay bears quadratic dependence on the particle size. The diameter exponent in the ignition delay relationship decreases from 2.0 to 0.25, when the particle size decreases from micron to nano scales. It will be useful to conduct a theoretical analysis to determine the effect of particle size on the ignition delay.

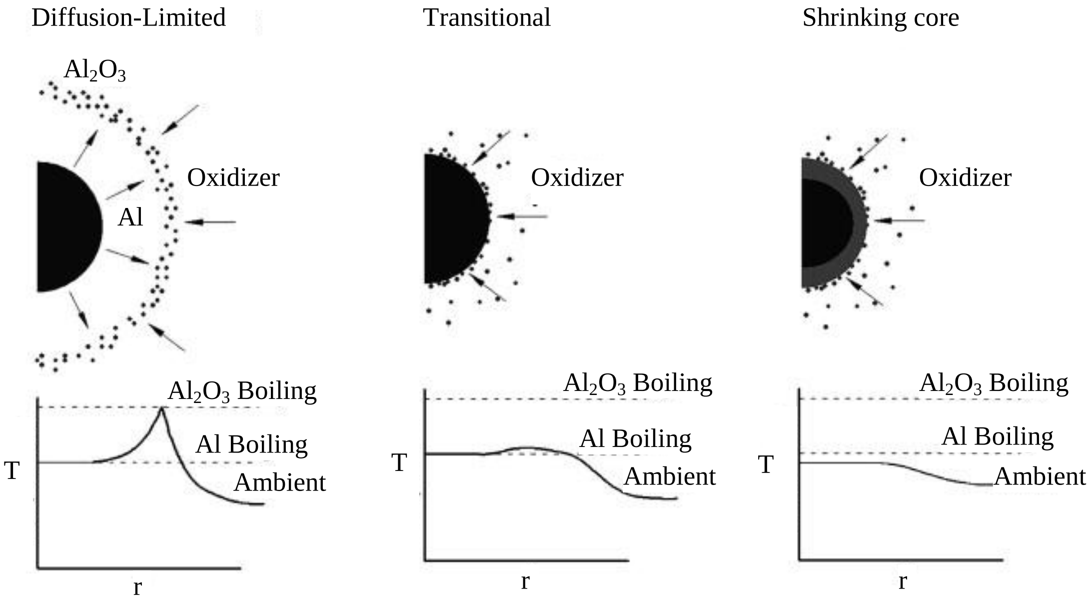

Figure 1.16: Schematic representation of flame structures and temperature distribution during combustion of aluminum particles in air (a) gas-phase reactions; (b) combined gas-phase and surface reactions; (c) surface reactions (Bazyn, Krier & Glumac 2007).

The combustion of nano-aluminum particles is still an unsettled problem. Figure 1.16 shows the hypothesized flame structures of aluminum particles in air for different particle sizes (Bazyn, Krier & Glumac 2007). Homogeneous gas-phase combustion characterized by the detached diffusion flame is observed for particles larger than 20 μm. The temperature reaches its maximum value of the oxide boiling point at the flame sheet. The particle temperature is equal to the boiling point of aluminum. For particles in the transitional regime, surface reactions become important and the flame front is located near the particle surface. The peak temperature is approximately equal to the boiling point of aluminum. Mohan et al. (Mohan, Trunov & Dreizin 2009) conducted heat transfer analysis of vapor phase combustion of metal particles. Figure 1.17 shows the

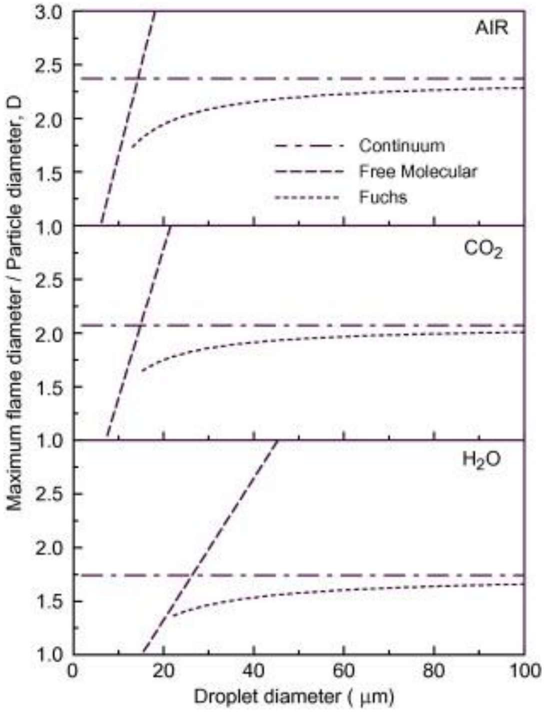

Figure 1.17: Ratio of maximum flame diameter to particle diameter as a function of particle size in different gas environments (Mohan, Trunov & Dreizin 2009).

ratio of maximum flame diameter to particle diameter (dimensionless flame diameter) as a function of particle size at a pressure of 1 atm. At a critical particle size (e.g., 6 μm in air), the dimensionless flame diameter is equal to unity (or the flame is located at the particle surface). This phenomenon is attributed to the transition from continuum to free-molecular heat transfer regime. For nano-sized particles, heterogeneous reactions inside the particle or at the particle surface are the principal mode of combustion. The surface tension forces causethe oxide layer to adhere to the particle surface. The flame (or particle) temperature may not be significantly greater than the ambient value due to the effects of heat losses to the surrounding environment (Bazyn, Krier & Glumac 2006, Badiola, Gill & Dreizin 2011). Species diffusion processes across the oxide layer may become important (Bazyn, Krier & Glumac 2007). Park et al. (Park et al. 2005) suggested that species diffusion through the oxide layer controls the rate of combustion of nano-

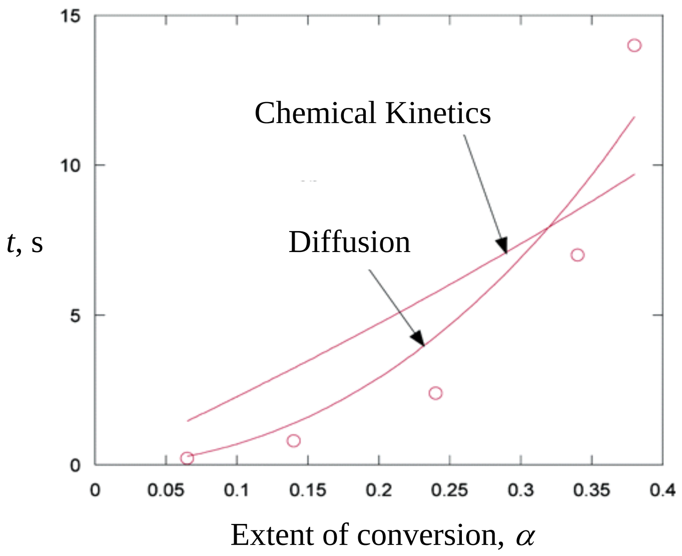

Figure 1.18: Extent of conversion (oxidation) vs. time for a 50 nm aluminum particle at a temperature of 1100 °C (Park et al. 2005).

aluminum particles. In their experiments, particles were oxidized in a tube furnace at various temperatures (25-1100°C). The residence time of the particle was on the order of 1 s and the heating rate was ~ 10^3 K/s. The composition and size of the particles were analyzed using the single particle mass spectrometer (SPMS). Figure 1.18 shows the extent of conversion (or oxidation) vs. time for a 50 nm aluminum particle at a furnace temperature of 1100 °C. The two curves represent the reaction time scales corresponding to diffusion and kinetically controlled combustion models. The experimental trend is better represented by diffusion controlled model. The diffusion coefficient is estimated to be on the order of 10^{-8} cm^2/s at a temperature of 1173 K. Note that the particle is not oxidized completely over a time period of 15 seconds. It important to recognize that the above results were obtained at relatively low heating rates and low ambient temperatures. In the shock tube experiments (Bazyn, Krier & Glumac 2006), the heating rates are in the range of 10^6-10^8 K/s and the particles completely burned within few milliseconds. Levitas (Levitas 2009) proposed the melt dispersion mechanism to explain the dependence of the burning time of nano-aluminum particles on the heating rate. Figure 1.19 shows the schematic illustrating the melt-dispersion mechanism, which is valid only at high heating rates (>10^6 K/s). The melting of aluminum core is accompanied by 6 % volume dilation, which creates dynamic pressure on the order of 1-3 GPa. The shell experiences hoop stresses that exceed the theoretical strength, thereby resulting in dynamic spallation. As a result, the aluminum core is exposed to the ambient pressure and an unloading tensile wave propagates towards the center of the particle. This results in the ejection of the molten aluminum clusters at very high velocities. It was speculated that this phenomenon is responsible for the enhanced reactivity of nano-aluminum

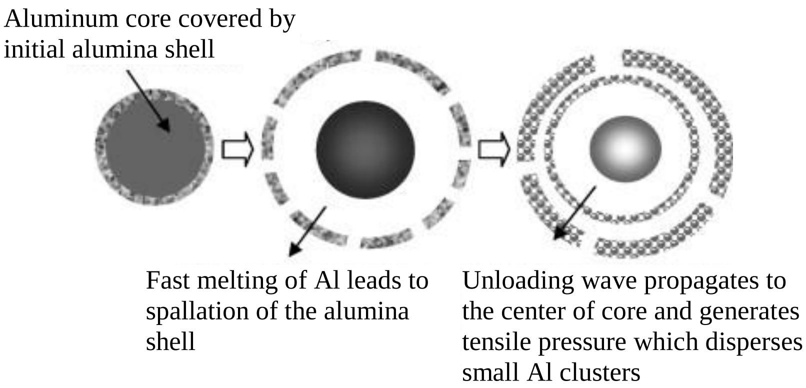

Figure 1.19: Schematic of the melt-dispersion mechanism (Levitas 2009).

particles at heating rates encountered in the shock tube experiments. The melt dispersion mechanism remains a theoretical concept, since no experimental evidence of the dispersion of aluminum clusters is present. Henz et al. (Henz, Hawa & Zachariah 2010) conducted molecular dynamics simulations and suggested that oxidation of nano-aluminum particles can occur by diffusion processes rather than spallation of the oxide shell. The calculated diffusion coefficients are on the order of 10^{-4} cm^2/s, which are about four orders of magnitude greater than the value obtained by Park et al. (Park et al. 2005). Simulations, however, indicate that melt dispersion is prone to occur for a heterogeneously heated particle, since the core pressure is three times greater than the counterpart for a homogeneously heated particle (Henz 2009). It is not yet understood if nano-aluminum particles burn through diffusion or explosive process. Further studies are warranted. The burning time of nano-aluminum particles is strongly dependent on the pressure and temperature of the gas (Bazyn, Krier & Glumac 2006) and weakly dependent on the particle size (Huang et al. 2009). This is contradictory to the trend observed for micron-sized particles ($d > 20$ μm). Some researchers (Bazyn, Krier &

Glumac 2007) attribute the former trend to transition of the combustion mode from diffusion to kinetically controlled conditions. The characteristic time scale for diffusion and chemical kinetics are given by (Yetter, Risha & Son 2009)

$$t_d = \frac{\rho_p d_p^{\,2}}{8\rho_g D i Y_{O,\infty}}, \tag{1.2}$$

$$t_{kin} = \frac{\rho_p d_p}{2MW_p k p X_{O,\infty}}, \tag{1.3}$$

where ρ_p is the particle density, d_p the particle diameter, D the diffusivity, i the stoichiometric ratio of the fuel-to-oxidizer mass, ρ_g the gas density, $Y_{O,\infty}$ the far-field mass fraction of oxygen, MW_p is the molecular weight of aluminum, p the pressure, k the rate constant, and X the mole fraction. The gas-phase diffusion time scale bears quadratic dependence on the particle size and is independent of the gas pressure, since the diffusivity is inversely proportional to pressure. The chemical kinetics time scale is inversely proportional to pressure and bears linear dependence on the particle size. As a result, the burn time is expected to have a relative weak dependence on the particle size under kinetically controlled combustion regime. The proposed explanation, however, contradicts the findings of Park et al. (Park et al. 2005), which indicate diffusion-limited combustion for nano-sized particles. This is further supported by the results of Aita's and Rai et al.'s theoretical studies (Aita 2005, Rai et al. 2006). The characteristic time scale for species diffusion through the oxide layer takes a form similar to that of Eq. (1.2), except that the solid-state diffusivity replaces the gas-phase counterpart (Levenspiel 1962). It is, however, unknown why the burning time is weakly dependent on the particle size, should a diffusion-limited combustion prevail at nano-scales. Badiola and Dreizin (Badiola & Dreizin 2012) speculate that the weak dependence of burn time on particle size is caused by the transition of the heat and mass transport modes from continuum to free-molecular regime. Young et al. (Young et al. 2009) believes sintering and agglomeration of particles may be yet another contributing factor. It is, thus, evident that the combustion mechanism of nano-aluminum particles is still disputed and not well understood. Further studies are necessary on this subject.

1.3.3 Nickel-Coated Nanoaluminum Particles

Nanoaluminum particles are covered by an inert oxide layer, which have thickness in the range of 2-4 nm (Trunov, Schoenitz & Dreizin 2006). The issue of active aluminum content becomes more important at nano-scales. Figure 1.20 shows the mass fraction of the oxide layer in the particle as a function of particle size. The thickness of the oxide layer is assumed to be equal to 3 nm based on the experimental data (Risha et al. 2007). The mass fraction of the oxide layer increases with decreasing particle size. The experimental data indicates that the active aluminum content of a 38 nm aluminum

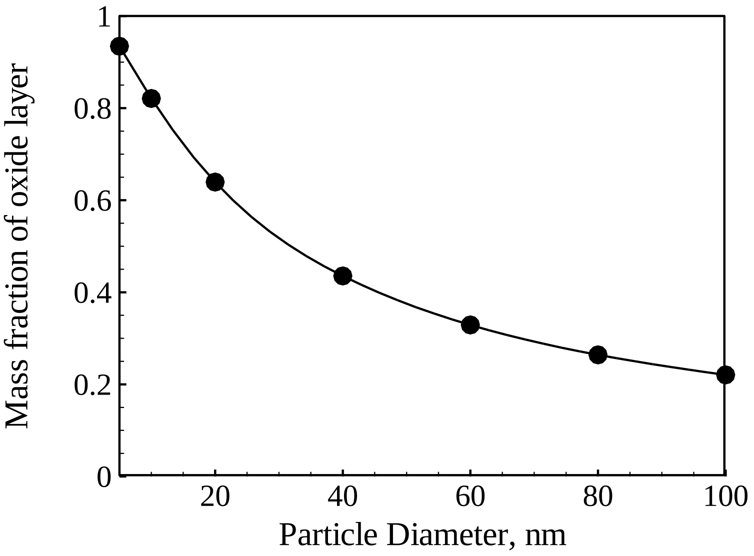

Figure 1.20: Mass fraction of aluminum oxide layer as a function of particle size.

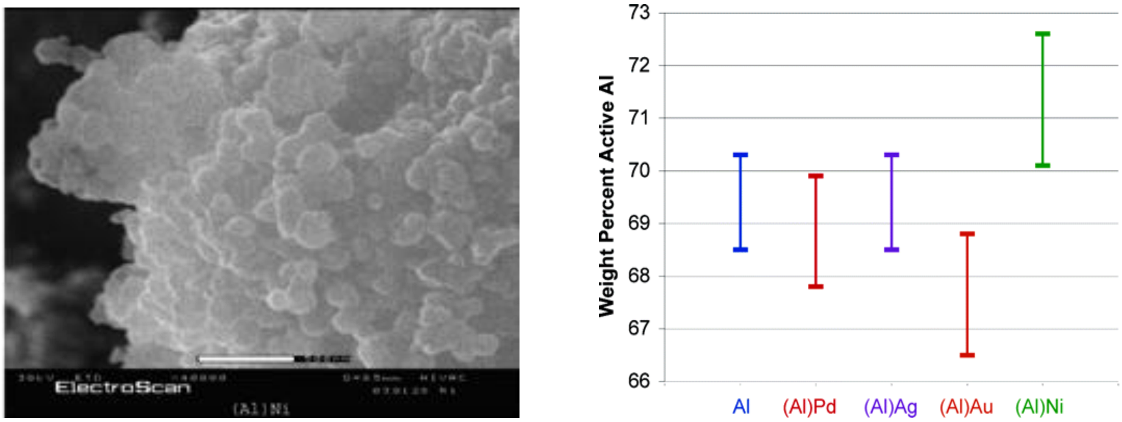

Figure 1.21: (a) Scanning electron micrographs of nickel-coated nanoaluminum powder (b) active aluminum content of particles encapsulated by different transition metals (Foley, Johnson & Higa 2005).

particle is 54.3 wt. % (Risha et al. 2007). As a result, the energy content of the particle is significantly diminished at nano scales. Encapsulation of nano-aluminum particles with nickel may result in higher active aluminum content (Foley, Johnson & Higa 2005). Nickel-coated nanoaluminum particles were synthesized using the wet-chemistry method. Nascent aluminum particles were slurried with dimethyl ether (DME). In a separate flask, acetylacetonate of transition metals was dissolved in DME. The resulting solution was added to the stirred aluminum slurry and allowed to react for 12 hours. The powders were then passivated in air. Figure 1.21 shows the scanning electron micrographs of nickel-coated nanoaluminum powders and the active aluminum content of the particles for different metal coatings. Nickel-coated nanoaluminum particles have the highest aluminum content among all samples considered in the study. Palladium, silver, and gold did not afford a similar enhancement in the active aluminum content due to their heavier atomic weight. Note that nickel coating may also assist particle ignition through inter-metallic reactions.

The consolidated blend of aluminum and nickel powders is widely used in the combustion synthesis of nickel aluminides (Ni_xAl_{1-x}), which are attractive structural materials for many engineering systems (Morsi 2001). The reactant powders are ignited at one end and a self-sustaining combustion wave propagates through the packed mixture. The profound interest in the combustion synthesis is due to the simplicity and cost effectiveness of the process (Aruna & Mukasyan 2008). The combustion products have relatively low impurity content, since the flame vaporizes volatile contaminants (Li 2003). Recently, nano-scale powders are being explored for combustion synthesis of nickel aluminides (Hunt, Plantier & Pantoya 2004). Micro-structural images of the compacted powder blend indicate that the nickel particles are embedded in a continuous aluminum matrix or vice-versa (Farber, Klinger & Gotman 1998). The geometry of the system is thus usually simplified as a core-shell structure, where the shell represents the surrounding matrix (Farber, Klinger & Gotman 1998, Levchenko et al. 2010). Note that nickel-coated aluminum powders can also be directly employed to synthesize nickel-aluminides (Andrzejak, Shafirovich & Varma 2007, Thiers, Mukasyan & Varma 2002). Understanding the physicochemical characteristics of Ni/Al core-shell systems is, thus, important for both propulsion and material synthesis applications.

The thermochemical behavior of nickel coated nanoaluminum particles can be studied effectively using molecular dynamics simulations. Previous studies (Delogu 2007, Henz, Hawa & Zachariah 2009) provided some insight on the melting phenomenon of the aluminum core and its mechanical effect on the nickel shell. Delogu’s study (Delogu 2007) considered particles with a fixed diameter of 8 nm and three different shell thickness of 0.5, 1.0, and 2.0 nm. The melting temperature of the aluminum core was found to be greater than that of a nascent aluminum particle due to the cage-like effect imposed by the nickel shell. Melting of the core resulted in fragmentation of the shell, especially for thinner shells. Physicochemical processes after melting of the core was not studied. Henz et al.'s study (Henz, Hawa & Zachariah 2009) considered particles with a core diameter of 5 nm and shell thickness of 1 and 2 nm. For a shell thickness of 1 nm, melting of the core was followed by outward diffusion of core atoms. No such phenomenon was observed for 2 nm shell. In both cases, fragmentation of the shell was not observed. The physicochemical processes that occur after melting of the aluminum core (such as diffusion processes, shell melting, and inter-metallic reactions) have not been studied in sufficient detail. Furthermore, systematic studies on the effects of core size and shell thickness on relevant physiochemical processes are yet to be conducted. These are of paramount interest for both propulsion and material synthesis applications.

1.3.4 Safety Issues

The enhanced reactivity of nanoaluminum particles poses significant safety hazards. If the size of the nascent (unpassivated) particle is decreased below a critical value, the nascent particle could ignite when exposed to an oxidizing gas at room temperature, a phenomenon known as pyrophoricity (Glassman, Papas & Brezinsky 1992). It is a major safety issue during particle manufacture, handling, and storage. It can also be employed for useful applications like decoy flare for defending heat-seeking missiles (Yang, Brill & Ren (eds.) 2000). Reliable measurements or predictions of the critical particle size for pyrophoricity are of paramount interest. Theoretical studies on metal pyrophoricity are limited. Glassman et al. (Glassman, Papas & Brezinsky 1992) postulated that a metal particle is pyrophoric if the chemical energy release during the formation of the natural oxide layer (thickness of ~ 2.5 nm) is sufficient to vaporize the metal. This is motivated by the fact that homogeneous gas-phase combustion is observed for micron-sized aluminum particles. The analysis neglected heat losses to the ambient environment and size-dependence of physicochemical properties. Under these assumptions, the critical condition for metal pyrophoricity was obtained by equating the chemical heat release to the sum of the energies needed to heat the particle to the boiling point and vaporize the metal

$$\frac{\left(1-(\delta/R)_{cr}\right)^{3}}{\left\{1-\left(1-(\delta/R)_{cr}\right)^{3}\right\}}=\frac{\rho_{Al_2O_3}\left\{\left(-H^{o}_{ox}\right)-\left(H^{o}_{T_b}-H^{o}_{298}\right)\right\}_{Al_2O_3}}{\rho_{Al}\left(H^{o}_{T_b}-H^{o}_{298}+L_{vap}\right)_{Al}}, \tag{1.4}$$

where δ is the oxide layer thickness, R the particle radius, ρ the density, T_b the boiling point of aluminum, L_{vap} the enthalpy of vaporization of aluminum, and H the enthalpy. The subscripts *ox* and *cr* refer to oxidation and critical condition, respectively. For aluminum, the critical particle diameter was calculated to be 23 nm. Puri (Puri 2008) recognized the fact that nano-aluminum particles undergo heterogeneous surface reactions, incorporated the effect of heat losses, and employed size-dependent properties in transient energy balance analysis. The oxidation was assumed to be controlled by diffusion of oxygen molecules through the gas-phase mixture to the particle surface. The growing oxide layer is, thus, assumed to offer negligible diffusion resistance. The estimated critical particle size was 20 nm. It is worth noting that once a monomolecular oxide layer is formed, the oxidation of nano-aluminum particles is governed by the Mott-Cabrera oxidation kinetics (Jeurgens et al. 2002). In other words, the presence of growing oxide layer cannot be neglected. An essential feature of this model is that the metal electrons transverse the thin oxide layer either by thermionic emission or tunneling. The electrons ionize the adsorbed oxygen atoms to create an electrostatic potential between the oxide-oxidizer and oxide-metal interfaces. The presence of electric field aids the diffusion of metal cations through the oxide layer. Recently, the Mott-Cabrera oxidation kinetics was employed to study the pyrophoricity of nascent aluminum particles (Mohan, Ermoline & Dreizin 2012). These are discussed in detail in Chapter 7. The critical particle diameter was estimated to be 68 nm, which is significantly greater than the values predicted by Glassman et al. (Glassman, Papas & Brezinsky 1992) and Puri (Puri 2008). The experimental data also indicate that the critical particle is about 30 nm (Glassman, Papas & Brezinsky 1992). Mohan et al.'s study did not consider the size dependence of physicochemical properties of the particle, which is important at nano-scales. The effect of the passivating oxide layer also needs examination.

1.4 Combustion of Nanoaluminum-Water Mixtures

Several novel energetic materials based on nanoaluminum particles are being explored. These include thermites (metal/metal oxide mixtures), metalized composite solid propellants, nanofluids, and gels (Yetter, Risha & Son 2009). Gels are liquids whose rheological properties altered by the addition of gelling agents (Yetter, Risha & Son 2009). Gelled propellants share some of the advantageous properties of liquid and solid propellants. Gelling reduces the risk of leakages, while maintaining their ability to be pumped and throttled. Gelled propellants are not susceptible to cracking and are less sensitive to impact, friction, and electrostatic discharge. There are two general classes of gelling agents: particulates and polymers (Hammond 2001). An example of a particulate gellant is fumed silica (Sabourin et al. 2009). Nano-sized metal particles can act as a gellant by themselves due to their higher specific surface area, thereby replacing traditional low energy gellants (Sabourin et al. 2009). Nano-aluminum particles have been mixed with liquid water at higher particle loading densities to form a thick paste and mixtures that appear as dry powders (Risha et al. 2007). The reactive mixture of nanoaluminum particles and liquid water is rapidly gaining the attention of the scientific community due to its simplicity, high energy density, and "green" exhaust products (no chlorine containing compounds). The aluminum-water reaction can be expressed as

$$2\mathrm{Al} + 3\mathrm{H_2O} \rightarrow \mathrm{Al_2O_3} + 3\mathrm{H_2} \tag{1.5}$$

The reaction products consist of aluminum oxide particles and hydrogen gas. As a result, it is also attractive for production of hydrogen gas (Shafirovich, Diakov & Varma 2006). The mixture is also of interest to underwater propulsion, since water need not be carried on-board (Foote, Thompson & Lineberry 2002). Ivanov et al. (Ivanov et al. 1994, Ivanov et al. 2000) conducted one of the first experimental studies on the combustion of aluminum-water mixtures in the presence of thickening agent, polyacrylamide (3%). The specific surface area of the particles was ~18 m^2/g. It was claimed that a gelling agent was necessary to achieve self-sustained deflagration. The burning rate increased from 0.1 to 1.1 cm/s, when the pressure increased from 0.1 to 7 MPa. The measured combustion efficiencies were in the range of ~50-60 %. Incomplete combustion was attributed to boiling out of water from the reaction zone. Risha et al. (Risha et al. 2007) were able to achieve deflagration of nanoaluminum-water mixtures without additional gelling agents. The specific surface area of the particles ranged from 16.5-54.1 m^2/g. Figure 1.22 shows the captured images of nanoaluminum-water mixtures (Risha et al. 2007). The consistency of the mixtures depends on the particle size and equivalence ratio. A greater

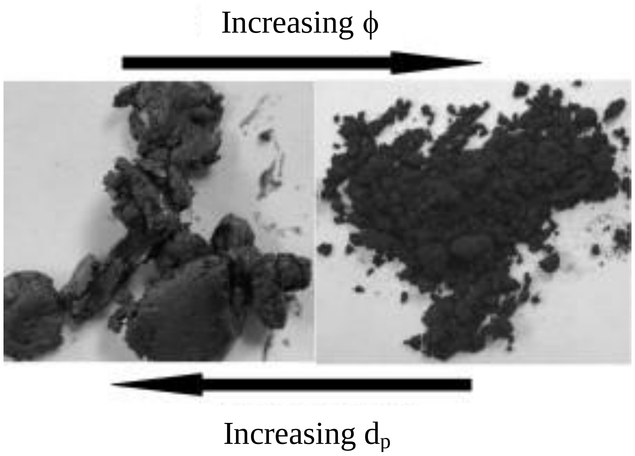

Figure 1.22: Consistency of nanoaluminum-water mixtures as a function of particle size and equivalence ratio (Risha et al. 2007).

number of water molecules are absorbed on the surface of a smaller particle due to its higher specific surface area, resulting in a powder-like consistency. For larger particles, paste-like consistency was obtained. The burning rates were obtained using a constant volume optical pressure vessel under well-controlled operating conditions in an argon environment, as shown schematically in Fig. 1.23. The chamber, constructed from 316 stainless steel, was equipped with four optical viewing ports each having a 15.2 × 2.54 cm field of view. The 61-cm long chamber has an inner diameter of 22 cm and a total free volume of 23 L to minimize the pressure variation caused by the generation of gaseous combustion products during an experiment. The base plate has six feed through ports to provide pathways into the chamber for electrical-signal and gas lines. One of the optical viewing ports was backlit through an optical diffuser, which evenly distributes the light emitted from the light source located outside the test chamber. The opposite viewing port of the diffuser was used for real-time recording of the burning process by a digital video camera. The particles were obtained from Technanogy and Nanotechnologies and

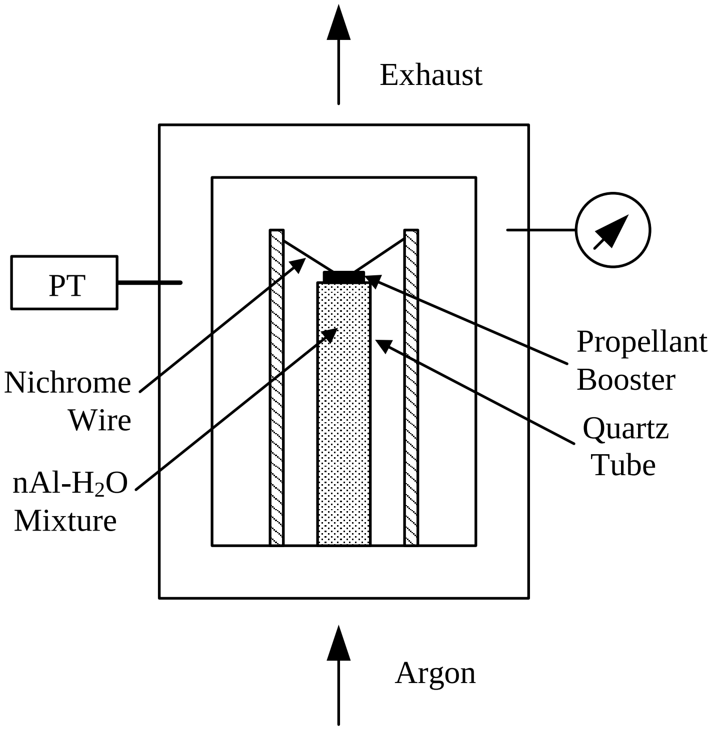

Figure 1.23: Schematic of the constant volume optical vessel employed to study combustion of nanoaluminum-water mixtures (Risha et al. 2007).

ranged in sizes from 38 to 130 nm in diameter. The active aluminum content varied from approximately 54–84% by mass. The nanoaluminum particles were mixed in small batches with distilled water in a sealed plastic bag. Stoichiometry was calculated based upon the active aluminum content in the particle. The mixture was then loaded into a quartz tube with a 10 mm OD (8 mm ID) × 75 mm length. A small ignition booster made of a homogeneous, double-base gun propellant (NOSOL 363) was placed atop the strand. For each test, the quartz tube was packed with the mixture and installed in the pressure vessel. The instantaneous pressure was monitored using a Setra 206 pressure transducer. Ignition was obtained by the small 1/8 in. thick propellant booster (mounted at the top of the quartz tube) initiated by a resistance-heated nichrome wire threaded through the

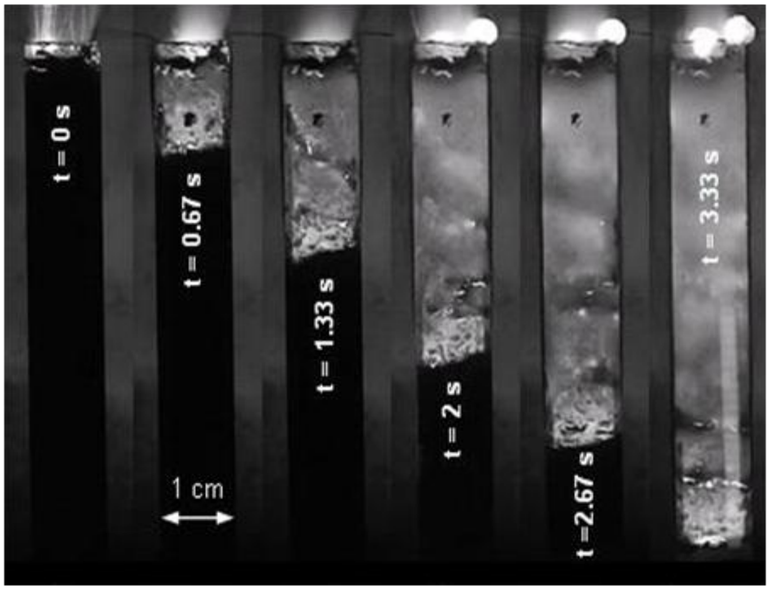

Figure 1.24: Photographs of stoichiometric 80 nm aluminum-water mixture burning at a pressure of 5.8 MPa (Risha et al. 2008).

booster. A data acquisition board was used to record the pressure transducer output at a sampling rate of 1000 Hz. The position and time of the regressing luminous front were tracked and recorded using the video record. From these data, the burning rate was determined using a curve fit to position vs. time. Figure 1.24 shows the photographs of stoichiometric 80 nm aluminum-water mixture burning at a pressure of 5.8 MPa. The flame propagates at a constant speed through the unburned mixture. Figure 1.25 shows the variations of the burning rate of the mixture with pressure and particle size. The mass burning rate per unit area is equal to the linear burning rate multiplied by the packing density of the mixture. The measured burning rates are greater than those of other energetic materials shown in the figure. The burning rate is inversely proportional to particle diameter and exhibits strong dependence on the gas pressure, with a burn rate

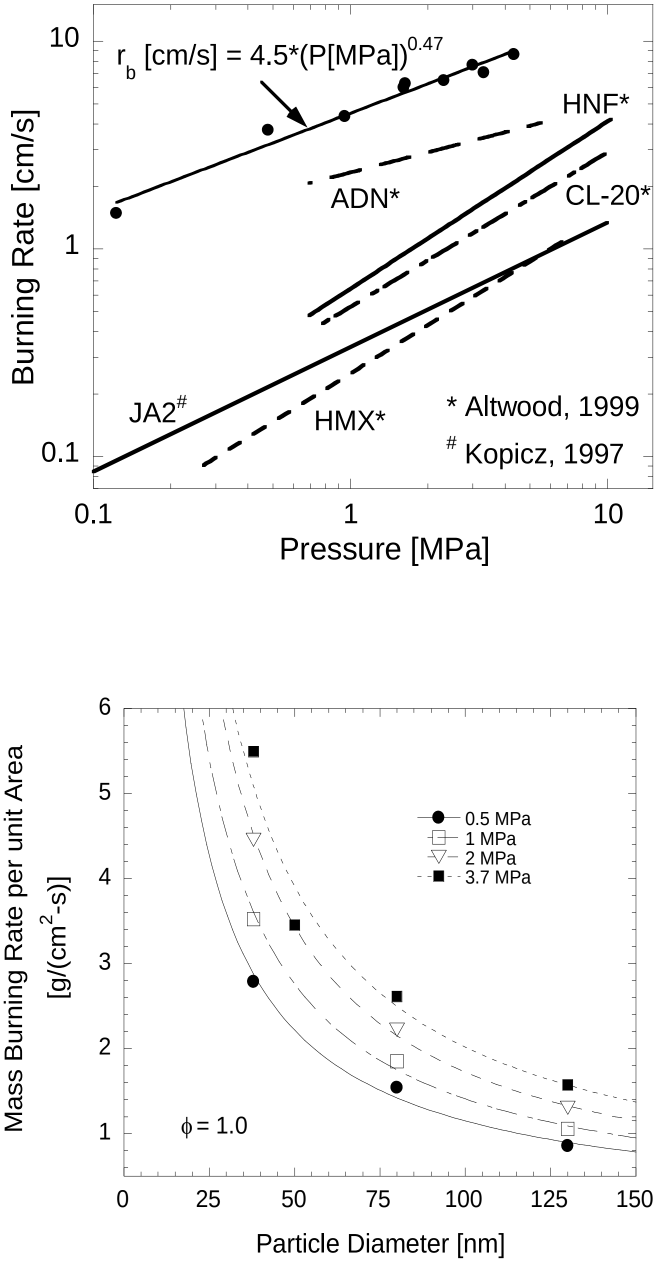

Figure 1.25: Variation of burning rate of stoichiometric nano-aluminum/water mixture with (a) pressure for a particle size of 38 nm and (b) particle size at four different pressures (Risha et al. 2007).

pressure exponent of ~0.5. Fundamental burning mechanisms are, however, not understood. The parameters that dictate the flame propagation velocity are also not known. One of the main drawbacks of nano-Al/water propellant, aging caused by low-temperature reactions and evaporation of water may be overcome by freezing the water in the mixture. This promoted the consideration of nano-aluminum particles and ice (ALICE) mixtures (Risha et al. 2013). Experimental data suggests that nano-aluminum/ice (ALICE) and nano-aluminum/water mixtures exhibit similar burning properties (Risha et al. 2013).

1.5 Research Objectives

The present work attempts to address several unresolved issues concerning the thermo-chemical behavior of various nano-energetic materials using appropriate modeling strategies:

- Molecular dynamics simulations are conducted to investigate the thermo-chemical behavior of nickel-aluminum core-shell structured particles over a broad temperature range of interest. Attention is given to all important physicochemical phenomena including core and shell melting behaviors, diffusion characteristics, and inter-metallic reactions. Systematic studies are performed to determine the effects of core size and shell thickness on physicochemical phenomena of interest.

- A theoretical framework is established to study the combustion of aluminum-water/ice mixtures over a broad pressure range of 1-10 MPa. The particle size range of concern is 38-130 nm. Numerical analysis is performed to explore the effects of pressure and particle size on the burning rate and flame structure. An attempt is made to elucidate the rate controlling burning mechanism and physicochemical parameters that dictate the burning rate. A closed-form (analytic) expression of the burning rate is also obtained. The effect of bimodal nano/micro particle size distribution on the temperature distribution and burning rate is investigated.

- Energy balance analysis is performed to investigate the ignition characteristics of aluminum particles. Specific focus is given to understand the effect of particle size on ignition delay and ignition temperature of aluminum particles and explain the phenomenon of weak dependence of ignition delay on particle size at nano-scales. A comprehensive analysis on the pyrophoricity of nascent and passivated nanoaluminum particles is performed with accurate evaluation of material properties (including size dependent physicochemical properties of the particle). Validity of the model is tested by comparison of the predictions with the experimental data.

1.6 Dissertation Outline

The dissertation is organized into nine chapters. Chapter 2 deals with the description of the molecular dynamics simulation framework. Chapters 3 and 4 discuss the thermo-chemical behavior of nickel-coated nano-aluminum and aluminum-coated nano-nickel particles, respectively. Chapter 5 outlines the theoretical framework adopted to study the flame propagation of nano-aluminum/water mixtures and discusses the obtained results. Chapter 6 presents the analysis of combustion of aluminum-ice (ALICE) mixtures with both mono-modal and bimodal particle size distributions. Chapter 7 concerns the study of pyrophoricity of nascent and passivated aluminum particles.

Chapter 8 deals with the ignition analysis of passivated aluminum particles. The conclusions of the thesis are summarized and suggestions for future work are presented in Chapter 9.

CHAPTER 2

MOLECULAR DYNAMICS SIMULATION FRAMEWORK

Molecular dynamics (MD) is a computer simulation technique that helps in predicting the time evolution of a system of interacting particles (atoms, molecules etc.). It is computationally tractable way to study the properties of clusters and nano-sized particles. In a typical MD simulation, positions and velocities are initially assigned to a chosen number of atoms. The atomic interactions are captured using an appropriate potential function. The classical Newton’s equations of motion are solved for each atom. The macroscopic properties are calculated using the principles of statistical mechanics. Note that the quantum effects can be neglected only if the De Broglie wavelength is much smaller than the inter particle distance (Rauscher & Dietrich 2011). The inter-atomic spacing is roughly $n^{-1/3}$, where n is the number density. For aluminum and nickel, the calculated inter atomic spacing is 2.5 and 3.3 Å, respectively. The de Broglie wavelength can be calculated as

$$\Lambda_{th} = \frac{h}{\sqrt{2\pi m k_B T}} \tag{2.1}$$

where Λ_{th} is the De Broglie wavelength, h the Planck's constant, m the mass of the atom, k_B the Boltzmann's constant, and T the temperature. The de Broglie wavelengths for some of the elements at room temperature are calculated to be 1 Å (hydrogen), 0.2 Å (aluminum), and 0.13 Å (nickel). As a result, *classical* MD simulations offer reasonably accurate predictions of the physicochemical properties for most elements except light ones such as hydrogen. In terms of simulation time scale, the maximum time step is limited by the fastest motion in the system. The integration time step must be smaller than the inverse of highest vibration frequencies, which are on the order of 10 fs (Choe & Kim 2000). A time step of 1 fs is thus commonly used in most MD simulations (Choe & Kim 2000). Due to the restrictive time step, only few nanoseconds or picoseconds of simulation are possible. It is also not possible to simulate very large systems (dimensions greater than ~100 nm). In the present study, particles in the size range of 3-20 nm are studied. Parallel computing is used to ensure reasonable turnaround time for the simulations. The computer program was developed by Puri (Puri 2008). In this thesis, a sufficiently detail overview of the molecular dynamics simulation framework is presented.

2.1 Potential Function

The classical conservation of mechanical energy of a system for the case of conservative forces can be written as

$$\frac{1}{2}mv^2 + U = E = constant, \tag{2.2}$$

which can be rewritten as

$$\frac{p^2}{2m} + U = E, \tag{2.3}$$

where m is the mass, p the momentum, U the potential energy, v the velocity, and E the total mechanical energy. In making transition to a quantum-mechanical wave equation the physical variables take the form of “operators” (Tuckerman 2010)

$$p \to \frac{\hbar}{i}\frac{\partial}{\partial x} \qquad H \to \frac{-\hbar^2}{2m}\frac{\partial^2}{\partial x^2} + U, \tag{2.4}$$

$$H\Psi = E\Psi, \tag{2.5}$$

where ψ is the wave function and H the Hamiltonian. Equation (2.5) is the time-independent version of the Schrödinger equation. The Born-Oppenheimer approximation can be used to solve the Schrödinger equation (or calculate the wave function) in two relatively less complicated steps (Schlick 2010). According to this approximation, electronic and nuclear motion can be separated and the total wave function can be expressed as:

$$\psi(\vec{r}_i, \vec{R}_i) = \psi_{electrons}(\vec{r}_i, \vec{R}_i)\psi_{nuclei}(\vec{R}_i), \tag{2.6}$$

where r and R are position vectors for electron and nuclei, respectively. The nuclear motion is much slower than electronic motion that the nuclei can be considered fixed relative to the speedy electrons. As a result, the problem can be reformulated in terms of two separate Schrödinger equations. In first step, the equation of electronic motion gives the electronic energy as a function of the coordinates of nuclei. In the second step, the obtained electronic energy (consisting of kinetic energies, inter-electronic repulsions, and electron-nuclear attraction) serves as the potential energy function for the nuclei motion. In classical molecular dynamics, the Schrödinger equation is replaced with the Newton's equation of motion (Rauscher & Dietrich 2011). The potential function can have an assumed analytical form and the parameters can be chosen to reproduce a set of experimental and/or *ab initio* data such as structural (cohesive energies, elastic constants, elastic moduli), and thermodynamic (melting point, latent heat) properties. Such empirical potential functions needs to be accurate, transferable, and computationally inexpensive. Potential function in the most generalized form can be written as (Allen & Tildesley 1989)

$$U\left(\vec{r}_1, \vec{r}_2, \ldots, \vec{r}_n\right) = \sum_i U_1\left(\vec{r}_i\right) + \sum_i \sum_{j>i} U_2\left(\vec{r}_i, \vec{r}_j\right) + \sum_i \sum_{j>i} \sum_{k>j} U_2\left(\vec{r}_i, \vec{r}_j, \vec{r}_k\right) + \ldots, \tag{2.7}$$

where U_1 is the one-body term due to an external field, U_2 the two-body term, and U_3 the three-body term. For metals, majority of the potential functions are based on the embedded atom method (Daw & Baskes 1984). In this method, the energy needed to embed an atom in the background electron gas is considered in addition to the electrostatic interactions. The Cleri-Rosato potential function (Cleri & Rosato 1993), which is based on this concept, is employed in the present study. It takes the following form:

$$U = \sum_{i=1}^{N} \left(\sum_{j \neq i} V_{ij} - \sqrt{\sum_{j} \rho_{ij}} \right). \tag{2.8}$$

The first term describes the electrostatic interactions, while the second term accounts for the energy needed to embed an atom in the electron gas. The pair-potential and electron density functions are expressed as

$$\begin{aligned} V_{ij} &= A_{\alpha\beta} \exp\left(-p_{\alpha\beta} \left(\frac{r_{ij}}{r^0_{\alpha\beta}} - 1 \right) \right), \\ \rho_{ij} &= \xi^2_{\alpha\beta} \exp\left(-2q_{\alpha\beta} \left(\frac{r_{ij}}{r^0_{\alpha\beta}} - 1 \right) \right). \end{aligned} \tag{2.9}$$

Table 2.1: Parameters for potential function (Cleri & Rosato 1993, Delogu 2007).

	Ni-Ni	Al-Al	Ni-Al
A(eV)	0.0376	0.1221	0.0597
ξ (eV)	1.0700	1.3160	1.2898
p	16.999	8.6120	15.714
q	1.1890	2.5160	1.1550
r_0 (Å)	2.4910	2.8637	2.5001

Table 2.1 shows the parameters of the potential function (Cleri & Rosato 1993, Delogu 2007). The potential function accurately reproduces the structural and thermodynamic properties of aluminum, nickel, and nickel-aluminum inter-metallic compounds.

2.2 Equations of Motion

The motion of each atom in the system is calculated using Newton’s equation of motion. The accelerations are direct function of the forces acting on the atoms. Since the forces are conservative, they are computed as the negative gradient of the potential energy (Allen & Tildesley 1989)

$$m_i \frac{d^2\vec{r}_i}{dt^2} = \vec{F}_i = -\nabla_i U. \tag{2.10}$$

Figure 2.1 shows the flow chart illustrating the steps involved in a typical MD simulation. The problem is set up by defining the initial positions and velocities of all the atoms of the system. The force acting on each atom is calculated using the potential energy, which is a function of inter-atomic distances. Newton’s equations of motion are then used to determine the trajectory of the atoms. The desired macroscopic properties are computed based on the principles of statistical mechanics. The whole procedure is repeated for a specified number of time steps. Numerical integration is achieved using the fifth-order predictor corrector method (Allen & Tildesley 1989). If the position, velocity, acceleration, etc. are known at time t, these quantities can be predicted for the time t+ δt

$$r_i^p(t+\delta t) = r_i(t) + v_i(t)\delta t + \frac{1}{2!}a_i(t)\delta t^2 + \frac{1}{3!}b_i(t)\delta t^3 + \frac{1}{4!}c_i(t)\delta t^4 + \frac{1}{5!}d_i(t)\delta t^5,$$

$$v_i^p(t+\delta t) = v_i(t) + a_i(t)\delta t + \frac{1}{2!}b_i(t)\delta t^2 + \frac{1}{3!}c_i(t)\delta t^3 + \frac{1}{4!}d_i(t)\delta t^4,$$

$$a_i^p(t+\delta t) = a_i(t) + b_i(t)\delta t + \frac{1}{2!}c_i(t)\delta t^2 + \frac{1}{3!}d_i(t)\delta t^3,$$

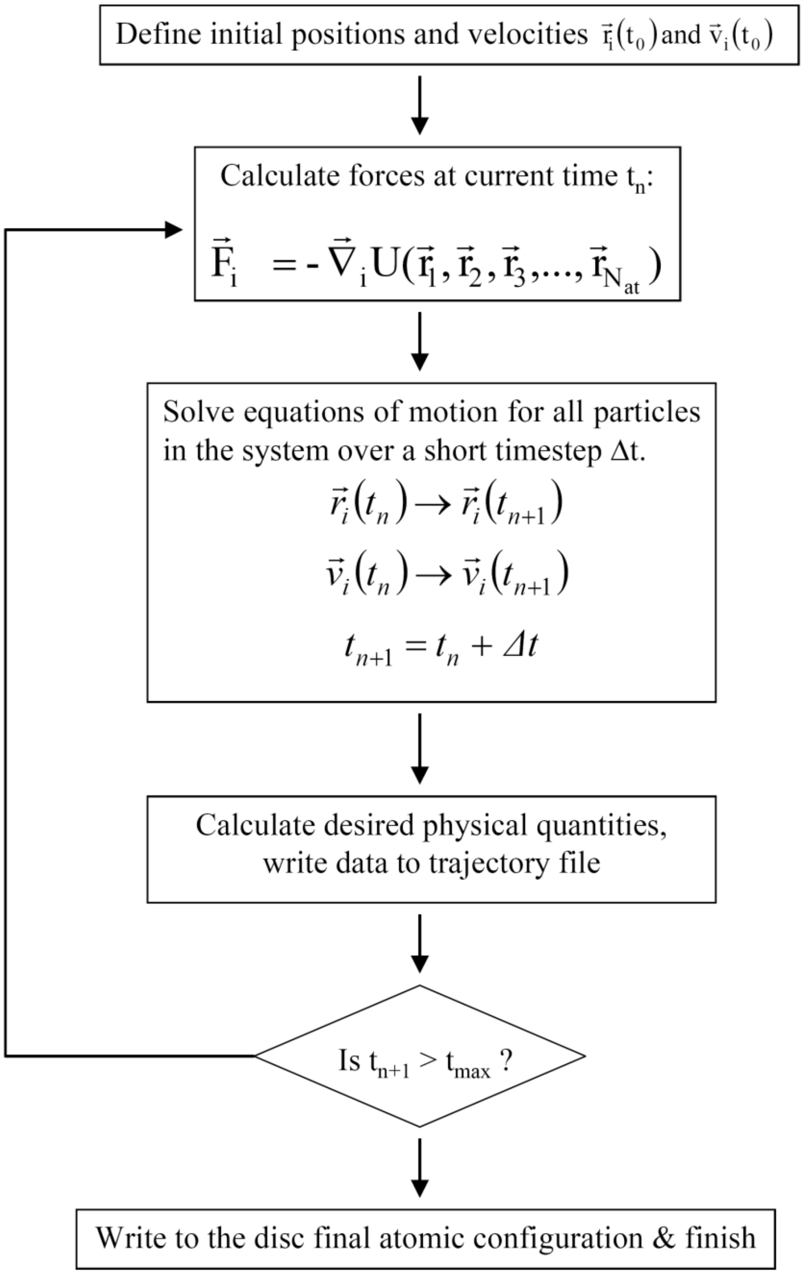

Figure 2.1: Flowchart illustrating the steps involved in an MD simulation.

$$
\begin{aligned}
b_i^p(t+\delta t) &= b_i(t) + c_i(t)\delta t + \frac{1}{2!} d_i(t)\delta t^2, \\
c_i^p(t+\delta t) &= c_i(t) + d_i(t)\delta t, \\
d_i^p(t+\delta t) &= d_i(t).
\end{aligned}
\tag{2.11}
$$

Once the accelerations have been evaluated using the forces, the difference between the predicted and calculated accelerations is called the error

$$
\delta a_i(t+\delta t) = a_i^c(t+\delta t) - a_i^p(t+\delta t). \tag{2.12}
$$

The corrected values of different quantities are then obtained using the calculated error, predicted values, and appropriate constants chosen to maximize the efficiency of the algorithm.

$$
\begin{aligned}
r_i^c(t+\delta t) &= r_i^p(t+\delta t) + c_0 \delta a_i(t+\delta t), \\
v_i^c(t+\delta t) &= v_i^p(t+\delta t) + c_1 \delta a_i(t+\delta t), \\
a_i^c(t+\delta t) &= a_i^p(t+\delta t) + c_2 \delta a_i(t+\delta t), \\
b_i^c(t+\delta t) &= b_i^p(t+\delta t) + c_3 \delta a_i(t+\delta t), \\
c_i^c(t+\delta t) &= c_i^p(t+\delta t) + c_4 \delta a_i(t+\delta t), \\
d_i^c(t+\delta t) &= d_i^p(t+\delta t) + c_5 \delta a_i(t+\delta t),
\end{aligned}
\tag{2.13}
$$

where the constants have values

$$
\begin{aligned}
c_0 &= 3/20 \qquad & c_1 &= 251/360 \\
c_2 &= 1 \qquad & c_3 &= 11/18 \\
c_4 &= 1/6 \qquad & c_5 &= 1/60
\end{aligned}
\tag{2.14}
$$

2.3 Crystal Structure and Boundary Conditions

The initial arrangement of the atoms is based on the crystal structure of the material. Figure 2.2a shows the face-centered cubic crystal structure which is observed for both aluminum and nickel. The lattice constants are 4.032 and 3.52 Å for aluminum and nickel, respectively (Kittel 2004). The entire crystal (super cell) is generated by replicating the fractional coordinates with the lattice spacing in all three directions.

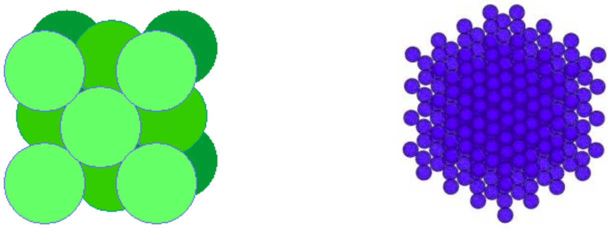

Figure 2.2: (a) Schematic of the face-centered cubic (FCC) crystal structure; (b) super cell of aluminum (Puri 2008).

Figure 2.2b show the super cell of aluminum. In order to create a spherical particle, all the atoms that lie outside a specified radius are removed. In MD simulations, a free-surface boundary is typically applied for nano particles. For bulk materials, a periodic boundary condition is employed. Figure 2.3 shows the schematic illustrating the periodic boundary condition. An atom that leaves the simulation box on one side enters back on

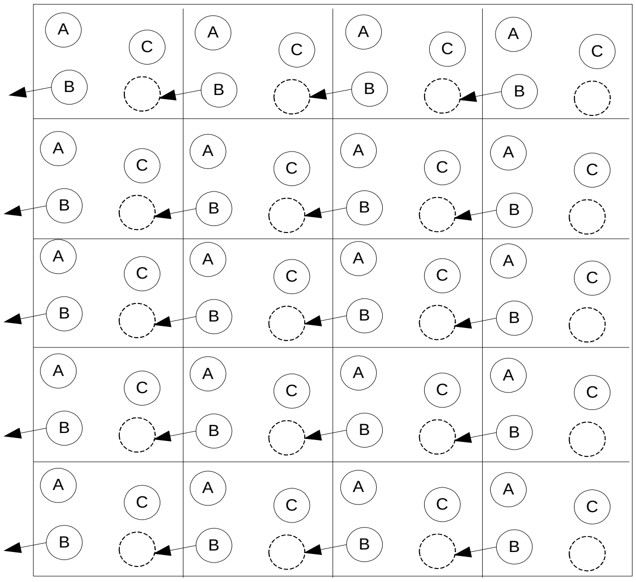

Figure 2.3: Schematic illustrating the periodic boundary condition.

the other side of the box. In addition, the minimum image criterion is imposed (Allen & Tildesley 1989). An atom *i* interacts only with the nearest image of the atom *j*. For the sake of consistency, the cut-off distance for the finite-range interactions is set to be less than or equal to half the box length.

2.4 Statistical Ensembles

An ensemble is a theoretical concept that can be used to analyze the dynamics of the system under desired conditions. There are four major ensembles in molecular dynamics (Allen & Tildesley 1989): (1) microcanonical (NVE); (2) isochoric-isothermal (NVT); (3) isobaric-isothermal (NPT); (4) isobaric-isoenthalpic (NPH). To simulate the system in a particular ensemble, the equations of motion are derived using Lagrangian mechanics. The Lagrangian equations of motion are derived using the Euler-Lagrange equation (Tuckerman 2010)

$$\frac{d}{dt}\frac{\partial L}{\partial q_i'} = \frac{\partial L}{\partial q_i}, \tag{2.15}$$

where L is the Lagrangian, q the generalized coordinate, and t the time. The Lagrangian is the difference between the kinetic and potential energies of the system. In the present study, both microcanonical (NVE) and isobaric-isothermal (NPT) ensembles are employed. For the NVE ensemble, the Newtonian equations of motion can be written as

$$mx'' = F = -\nabla U, \tag{2.16}$$

where x is the position vector, F the force, m the mass, and U the potential energy. The Lagrangian is given by

$$L = \frac{1}{2}mx'^2 - U(x). \tag{2.17}$$

Substituting Eq. (2.17) into Eq. (2.15), the following equations of motion for the NVE ensemble are obtained:

$$\frac{d}{dt}(mx') = -\nabla U(x). \tag{2.18}$$

In the NPT ensemble, a system of *N* atoms is coupled to an external source by introducing additional variables into the Lagrangian. Andersen (Andersen 1980) and Nose (Nose 1984) have established methodologies to control the pressure and temperature, respectively, which yield a canonical phase-space distribution. The position and velocity are scaled as follows

$$\begin{aligned} x_i &= V^{1/3} d_i, \\ \dot{x}_i &= s V^{1/3} \dot{d}_i. \end{aligned} \tag{2.19}$$

The potential energy, kinetic energy, and Lagrangian are expressed as

$$\begin{aligned} P.E. &= U(V^{1/3} d_1, \ldots, V^{1/3} d_{3N}) + pV + g k_B T \ln s, \\ K.E. &= \sum_i \frac{m s^2 V^{2/3} \dot{d}_i^2}{2} + \frac{M \dot{V}^2}{2} + \frac{Q \dot{s}^2}{2}, \\ L &= \sum_i \frac{m s^2 V^{2/3} \dot{d}_i^2}{2} + \frac{M \dot{V}^2}{2} + \frac{Q \dot{s}^2}{2} - U(V^{1/3} d_1, \ldots, V^{1/3} d_{3N}) - pV - g k_B T \ln s, \end{aligned} \tag{2.20}$$

where *M* is a constant fictitious mass associated with the volume of the system, *m* the mass of the atom, *U* the potential energy, k_B the Boltzmann constant, *s* the degree of freedom of the thermostat, *Q* the inertia factor, *V* the volume, treated as a dynamic variable, *p* the pressure, and d_i the scaled position of atom *i*. The equations of motion in the NPT ensemble are obtained as follows:

$$\begin{aligned} M\ddot{V} &= -p + \frac{s^2}{3V}\left[V^{2/3} \sum_i m_i \dot{d}_i^2 - V^{1/3} \sum_i F_i d_i \right], \\ m_i \ddot{d}_i &= \frac{V^{-1/3} F_i}{s^2} - \frac{2 m_i \dot{V} \dot{d}_i}{3V} - \frac{2 m_i \dot{s} \dot{d}_i}{s}, \\ Q\ddot{s} &= s V^{2/3} \sum_i m_i \dot{d}_i^2 - \frac{g k_B T}{s}. \end{aligned} \tag{2.21}$$

2.5 Macroscopic Properties

Statistical mechanics can be used to predict macroscopic properties of the system in terms of microscopic variables (position and velocities of system of atoms). For example, the temperature is defined as (Allen & Tildesley 1989)

$$T = \frac{2\langle K \rangle}{3Nk_B}, \tag{2.22}$$

where K is the kinetic energy of the system. For any physical property A, $\langle A \rangle$ denotes an average over time given by

$$\langle A \rangle = \frac{1}{N_{step}} \sum_{i=1}^{N_{step}} A(\Gamma_i), \tag{2.23}$$

where Γ_i represents a 6N-dimensional phase space consisting of positions and momenta of all atoms. Molecular dynamics simulations invoke the ergodic hypothesis, which states that the ensemble and time averages are equal (Tuckerman 2010). The pressure is calculated through the virial equation of state, as a function of the temperature of the system and forces experienced by all the atoms (Allen & Tildesley 1989)

$$pV = Nk_B T + \left\langle \frac{1}{3} \sum_{i=1}^{N} r_i . F_i \right\rangle. \tag{2.24}$$

The melting points are identified based on the variations in the potential energy, Lindemann index, and translational-order parameter. The Lindemann index is a measure of the vibrational motion of atoms (Zhuo et al. 2002)

$$\delta = \frac{2}{N(N-1)} \sum_{i<j} \frac{\sqrt{\langle r_{ij}^2 \rangle_t - \langle r_{ij} \rangle_t^2}}{\langle r_{ij} \rangle_t}. \tag{2.25}$$

The increase in vibrational motion is a characteristic of the phase change in materials and the Lindemann index is expected to increase abruptly during melting. The translational-order parameter is expressed as (Allen & Tildesley 1989)

$$\lambda = \frac{1}{N}\sqrt{\left(\sum_{i=1}^{N}\cos(k.r_i)\right)^2 + \left(\sum_{i=1}^{N}\sin(k.r_i)\right)^2}, \quad k = \left(\frac{(2N)^{1/3}\pi}{L}\right)(-1,1,1). \tag{2.26}$$

In solids, atoms translate about their lattice positions, and there is a perfect order. Such order, however, disappears in a liquid state, and the corresponding translational-order parameter is reduced by an order of magnitude.

2.6 Parallel Computation

Parallel computers are essentially many processors linked together and set to operate concurrently. If a given computational task is shared evenly among the processors, the task can be accomplished efficiently. Programming on parallel architectures requires considerations in terms of division of the computational workload and minimal communications between the processors. The molecular dynamics code has been parallelized using the atomic decomposition method (Plimpton 1995), in which the number of atoms are divided among the available processors. All simulations are conducted in Yang's supercomputing facility at Georgia Tech. Further details on parallelization can be found in Puri's thesis (Puri 2008).

CHAPTER 3

THERMO-CHEMICAL BEHAVIOR OF NICKEL-COATED NANO-ALUMINUM PARTICLES

The molecular dynamics simulation framework is employed to study the thermo-chemical behavior of nickel-coated nano-aluminum particles. The analysis deals with binary nickel-aluminum system and neglects the presence of metal oxides (Al_2O_3 and NiO) that may be formed as a result of heterogeneous oxidation reactions. The presence of oxidizing gas is not considered and all the simulations are conducted in vacuum. The predicted physicochemical behavior is thus expected to resemble those observed in inert environments. In practical applications, oxidizer molecules will diffuse through the shell and react with both aluminum and nickel atoms. As a result, both oxidation and inter-metallic reactions must be treated in parallel. Furthermore, the presence of defects in the particle is not considered. Defects may promote melting and impose an additional stress concentration effect, thereby facilitating the cracking the shell and altering the physicochemical behavior. The particle temperature is assumed to be uniform at every instant of time. For particles considered in this study, the calculated Biot numbers are orders of magnitude lower than unity. As a result, the lumped capacitance treatment is valid. Emphasis is placed on the behavior of single (or isolated) nickel-aluminum particles. In most practical applications, nano-particles are attracted towards each other by weak Van der Waals forces, thereby resulting in sintering and aggregation of particles. Investigation of particle-particle interactions are thus useful but beyond the scope of the present work.

NPT simulations are conducted to study physicochemical phenomena in the presence of external heating, while NVE simulations are employed to investigate self-heating of the particle due to inter-metallic reactions under adiabatic condition. For NPT simulations, the heating rate is an important adjustable parameter of concern. A parametric study is conducted to determine the appropriate value of the heating rate in the range 10^{-3}-10^{-1} K/fs (10^{12}-10^{14} K/s). Figure 3.1 shows the variation of potential energy with temperature for a 7 nm aluminum particle at different heating rates. At a heating rate of 10^{14} K/s, melting occurs over a much wider range of temperatures. At lower heating rates, particle melting is relatively isothermal and melting is completed at a lower temperature. Shibuta and Suzuki (Shibuta & Suzuki 2011) analyzed the effect of the cooling rate on the solidification of metal nano-particles using MD simulations. The solidification temperature decreased with increasing cooling rate. A similar phenomenon

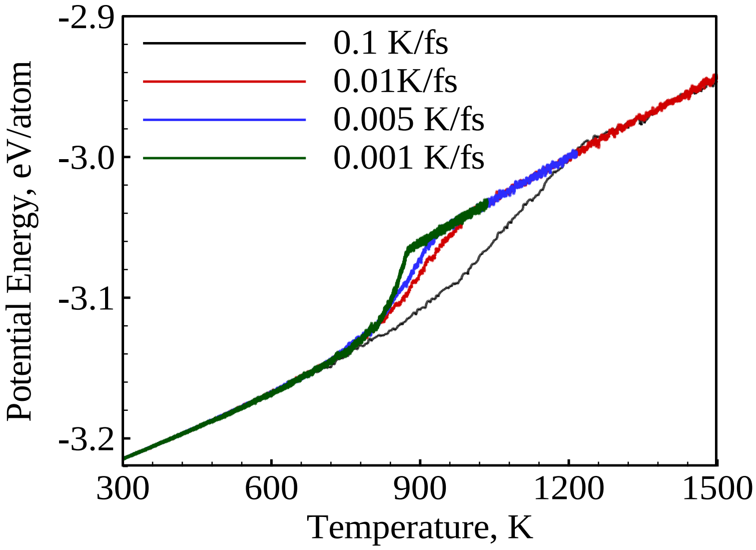

Figure 3.1: Variation of potential energy of 7 nm (10976 atoms) aluminum particle with temperature at different heating rates.

is observed in the present study. Both the onset temperature and temperature range of melting decreases with decreasing heating rate. Luo and Ahrens (Luo & Ahrens 2003) studied the systematics of homogeneous melting under different heating rates and concluded that the melting temperature increases with increasing heating rate. The sensitivity of the melting temperature to heating rate is found to be a function of atomic number. For aluminum, the melting temperature increases by 5 %, when the heating rate increases from 1 to 10^{12} K/s. In MD simulations, the time step places restriction on the minimum value of the heating rate. The analysis reveals that a heating rate lower than 10^{-2} K/fs increases the total computational time dramatically with only little (and predictable) change in the model results, while a higher value leads to significantly different results. As a result, a heating rate of 10^{-2} K/fs (10^{13} K/s) is adopted in the present study. This is greater than the heating rates concerning the burning of real energetic materials. For example, the measured intrinsic heating rates for nano-scale Al/CuO thermites are on the order of 10^{7} K/s (Chowdhury et al. 2010). The present study thus captures the physicochemical behavior of the particle under much faster heating conditions. The atomic interactions are captured using the Cleri-Rosato potential function with the parameters shown in Table 2.1.

3.1 Pure Aluminum and Nickel

The structural and thermodynamic properties of aluminum and nickel are first calculated. Unlike bulk materials, the thermophysical properties (e.g., melting points) of nano-sized particles have not been extensively studied. Puri and Yang (Puri & Yang 2007) conducted MD simulations and studied the effect of particle size on the melting temperature of nano-aluminum particles. Comparison with the experimental data was not reported. Qi et al.'s study (Qi et al. 2001) is the only reported work on the size-dependence of melting temperature of nickel particles. The calculated values were, however, significantly lower than the experimental data. As a result, it is useful to have have more accurate data of the melting temperature of nickel particles. Analysis of thermophysical properties of pure aluminum and nickel is also an important step to ascertain the validity of the model. An FCC lattice is adopted to calculate the initial position vectors for a known number of atoms. For bulk materials, a periodic boundary condition is enforced in all the three spatial directions. A free-surface boundary condition is, however, prescribed for nano-particles. The crystal is allowed to equilibrate at 300 K prior to the heating simulation.

3.1.1 Bulk Materials

The properties of surface-free bulk systems of aluminum and nickel are first treated. The lattice constant and cohesive energy are calculated by equilibrating the crystal in an NVE ensemble. To determine the melting point and latent heat of melting, the crystal is heated externally in an NPT ensemble. Table 3.1 shows calculated values of the cohesive energy, lattice constant, and latent heat of melting and compares them with experimental data (Kittel 2004, Brandes & Brook 1992, Kubaschewski, Alcock &

Table 3.1: Cohesive energy, lattice constant, and latent heat of melting of bulk materials.

	Aluminum		Nickel	
	Model	Experiment	Model	Experiment
E_c (eV/atom)	-3.337	-3.340	-4.437	-4.435
a (Å)	4.048	4.050	3.491	3.520
ΔH_m (kJ/mol)	10.610	10.470	17.360	17.160

Spencer 1993). The discrepancy is less than 2 %, thereby demonstrating the accuracy of the potential function. Figure 3.2 shows the variation of the translational order parameter and Lindemann index for surface-free bulk aluminum and nickel. Melting of aluminum is observed at 1060 K, at which point sharp variations occur in the translational-order parameter and Lindemann index. Such a trend is characteristic of the structural melting (or homogeneous melting), which is caused by the absence of a nucleation site for melting in the simulated system. The structural melting point (determined from MD simulations at a heating rate of 10^{13} K/s) is typically greater than the thermodynamic counterpart by about 20 % (Mei & Lu 2007). This number is expected to serve only as a rough estimate (or a rule of thumb) of the degree of superheating in idealized system. An approximate estimate of the bulk value of the heterogeneous melting temperature of aluminum particles is 883 K, which is comparable to the experimental value of 933 K. Note that the experimental melting temperature is also a function of the heating rate. A similar pattern is observed for bulk nickel, as shown in Fig. 3.2. It melts at 1950 K, which is greater than the melting temperature of nickel (1728 K) by 222 K.

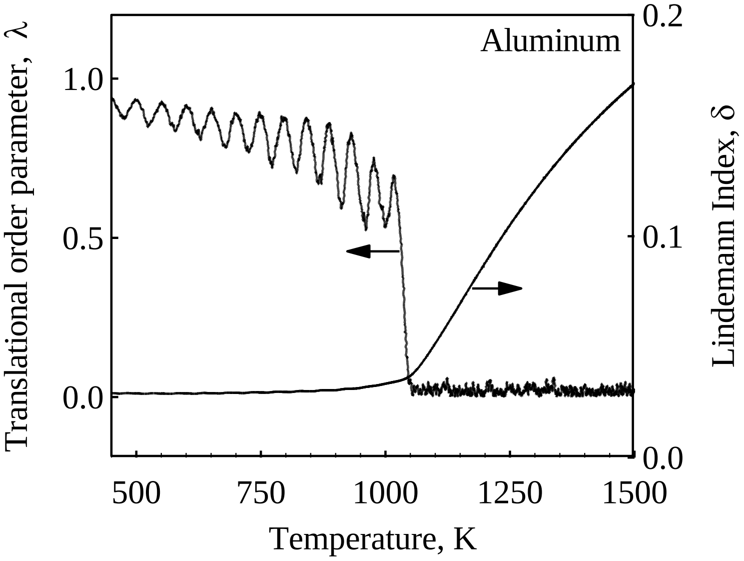

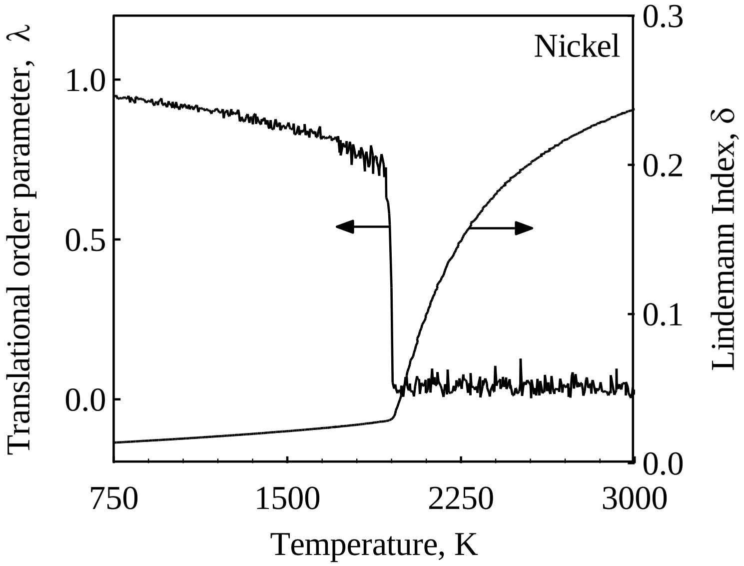

Figure 3.2: Translational order parameter (λ) and Lindemann index (δ) as a function of temperature showing the melting of bulk aluminum and nickel in vacuum.

3.1.2 Nano Particles

The melting of nanoscale particles is examined over a size range of 1.5-12 nm. Figure 3.3 shows the variation of the potential energy and Lindemann index with temperature for a 7 nm aluminum particle consisting of 10976 atoms. The melting point was defined as the temperature at which the slope of potential energy (calculated using the data at every N time steps in order to eliminate the noise/fluctuations and retain the temporal resolution) begins to increase sharply towards the peak value. The slope of potential energy curve then remains constant over a range of temperatures, thereby representing melting of the bulk of the core volume. Note that there is a small uncertainty of 20-30 K in the predicted melting point. It is also likely to change if a different parameter (e.g., Lindemann index) is employed to characterize melting. For aluminum, melting occurs at 810 K. The surface acts as a nucleation site for phase transition and the melting front propagates to the interior regions of the core. Hence, the phase change is manifested by a gradual increase in the properties, as opposed to the abrupt changes found in a bulk material. A similar trend is observed for the nickel particle, except that melting takes place at a higher temperature of 1540 K. Figure 3.4 shows the effect of

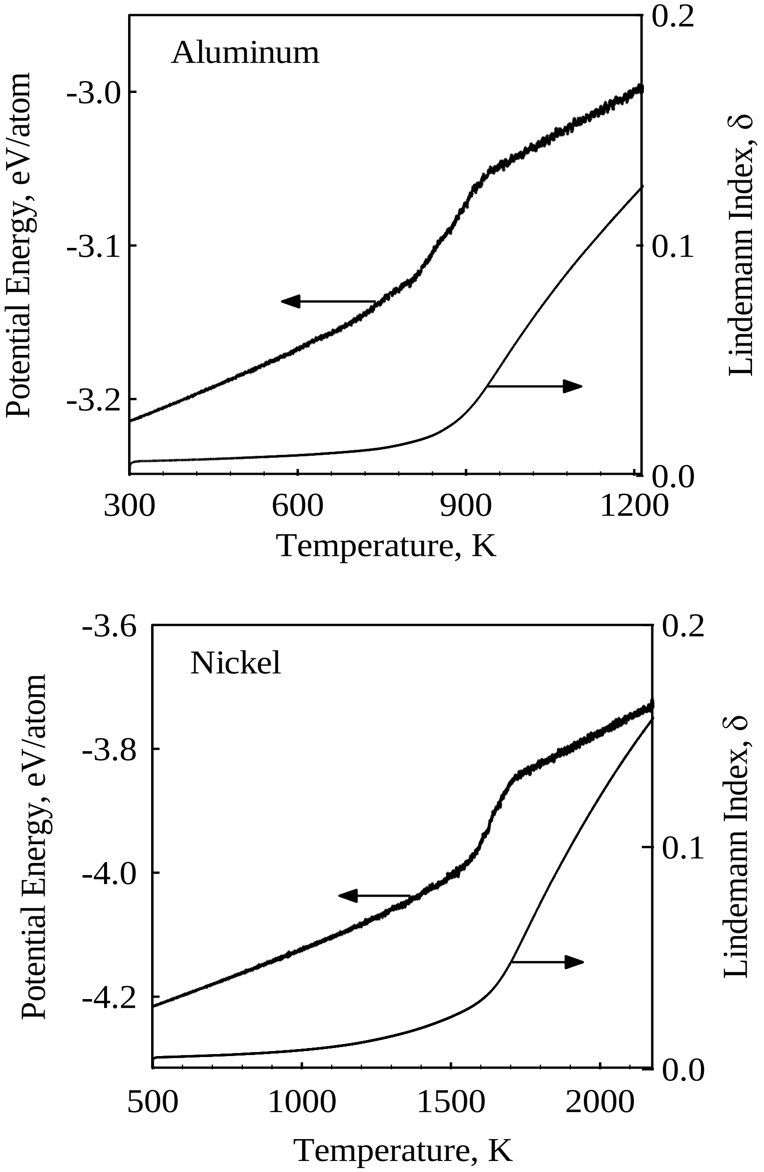

Figure 3.3: Potential energy and Lindemann index (δ) as a function of temperature showing the melting of 10976-atom aluminum (7 nm) and nickel (6 nm) particles.

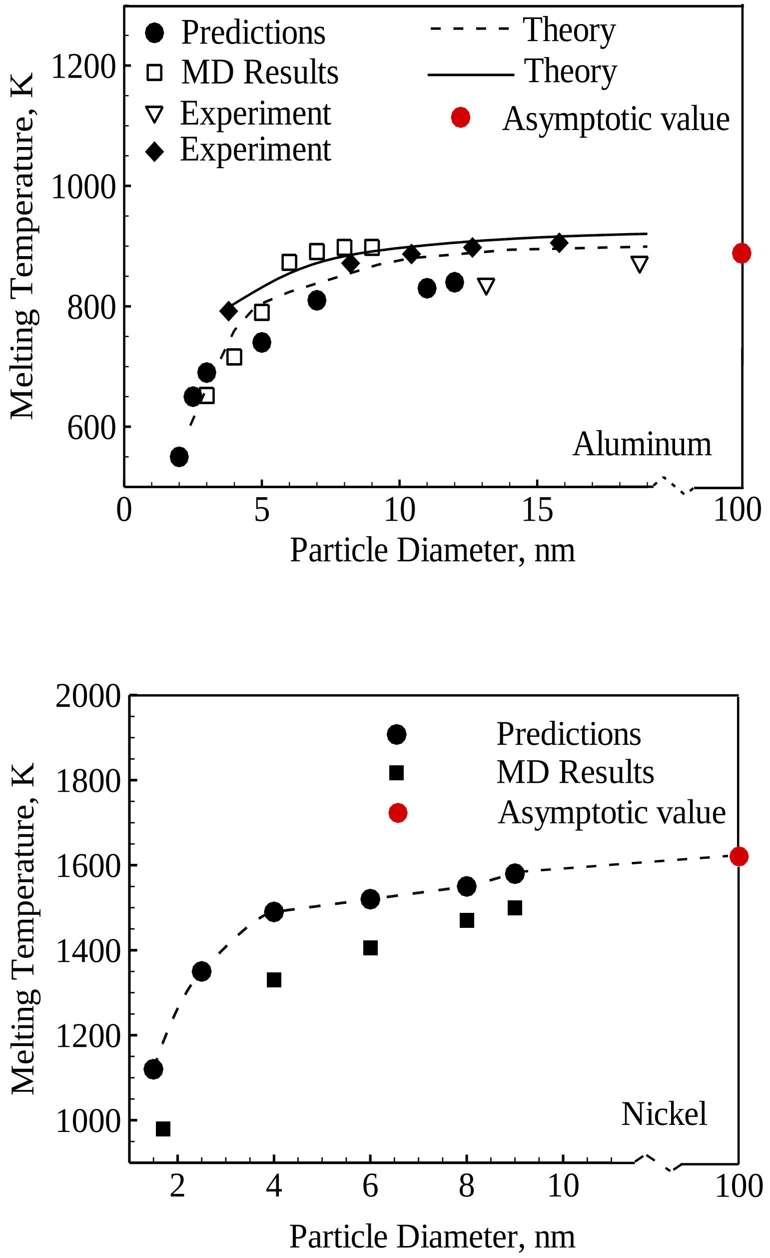

Figure 3.4: Effect of particle size on melting temperature of aluminum and nickel particles (Qi et al. 2001 (■), Puri & Yang 2007 (□), Lai, Carlsoon & Allen 1998(♦), Eckert et al. 1993 (∇)).

particle size on the melting temperature of aluminum and nickel at nano-scales. It also shows comparison with the results of previous MD simulations, experiments, and theoretical studies (Levitas & Samani 2011). The theoretical curves were obtained by using the phase-field theory (Ginzburg-Landau (GL) equation) coupled with advanced material mechanics. Further details on theoretical work are referred to the original work (Levitas & Samani 2011). The surface atoms pre-melt due to their lower cohesive energy. This phenomenon is referred to as surface premelting. Since the percentage of surface atoms increases with decreasing particle size, a smaller particle melts at a lower temperature. Note that the dependence of the melting point on particle size becomes much weaker for diameters greater than 10 nm. The experimental and theoretical data indicate a qualitatively similar reduction in the melting point with decreasing size. It is rather surprising that the predicted values exhibit good agreement with experimental data of Eckert et al. (Eckert et al. 1993), since the model under-predicts the melting point. This can be attributed to the fact that the heating rates in the simulations are orders of magnitude higher than those employed in the Eckert's experiments (Eckert et al. 1993). Eckert's experiments employed differential scanning calorimetry (DSC) with heating rates on the order of 1 K/s, while Lai et al.'s experiments (Lai, Carlsoon & Allen 1998) employed thin-film DSC nanocalorimetry (TDSC) with heating rates on the order of 10^5 K/s. It is, thus, not surprising that the predicted values are comparable with the experimental data of Eckert et al. Qi et al. (Qi et al. 2001) calculated the melting points of nickel particles as a function of particle size using the quantum-corrected Sutton-Chen potential. The resulting values are lower than those obtained using the Cleri-Rosato potential function. Note that the heating rate employed in Qi et al.'s study is 4×10^{12} K/s, which is slightly lower than the value of 10^{13} K/s used in the present study.

3.2 Nickel-Coated Nano-Aluminum Particles

The computational model is employed to analyze the thermo-chemical behavior of nickel-coated nano-aluminum particles. Figure 3.5 shows the initial structure of a nickel-coated aluminum particle with a core diameter of 12 nm and shell thickness of 1 nm. A spherical nickel particle of known dimension is first generated. A spherical void is then created in the interior of the nickel particle to accommodate the aluminum core. The resulting particle is equilibrated at 300 K prior to the heating simulation. Table 3.2 shows the values of the core diameter (d_c), shell thickness (δ_s), total number of atoms (N), and number of aluminum atoms (N_{Al}). The core diameter varies in the range of 3-12 nm, and three different shell thickness of 0.5, 1, 2, and 3 nm are considered. The aluminum atomic fraction increases with increasing core size and decreasing shell thickness.

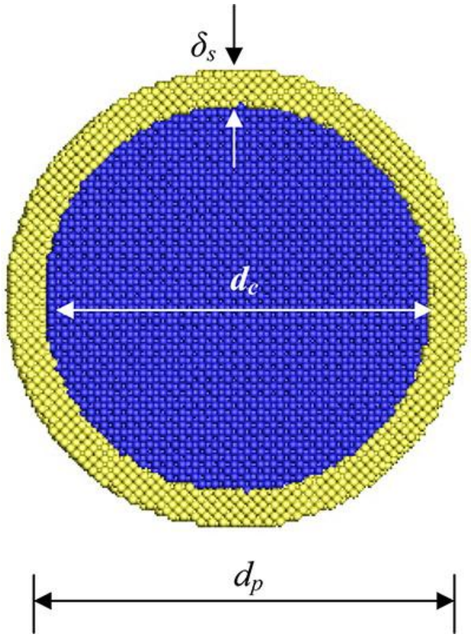

Figure 3.5: Initial crystal structure of nickel-coated aluminum particle ($d_p = d_c+2\delta_s$).

Table 3.2: Configuration of nickel-coated nano-aluminum particles.

d_c, nm	δ_s, nm	N	N_{Al}	X_{Al}
3	0.5	2909	874	0.30
3	1.0	7187	874	0.12
3	2.0	17440	874	0.05
3	3.0	37065	874	0.02
5	1.0	15496	4081	0.26
6	1.0	20914	6380	0.30
6	0.5	12760	6380	0.50
8	1.0	39435	15504	0.39
12	1.0	103737	53752	0.52
12	2.0	169899	53752	0.31
12	3.0	254614	53752	0.21

3.2.1 Baseline Simulation

To facilitate detailed discussion of the thermochemical behavior of nickel-coated aluminum particles, a particle with a core diameter of 12 nm and shell thickness of 1 nm is first considered. Figure 3.6 shows the variation of the Lindemann index and potential energy of the core with temperature. Melting of the core is characterized by deviation from the linear trend, beginning at approximately 1000 K. The predicted melting point is greater than that of a similar-sized nascent aluminum particle, which is ~883 K. It is, however, lower than the calculated structural melting point of bulk aluminum, 1060 K. The latter represents the upper limit for the core melting point, since it is the temperature at which the crystal undergoes catastrophic mechanical failure. The melting point elevation for a coated nano particle has been observed in previous experimental and

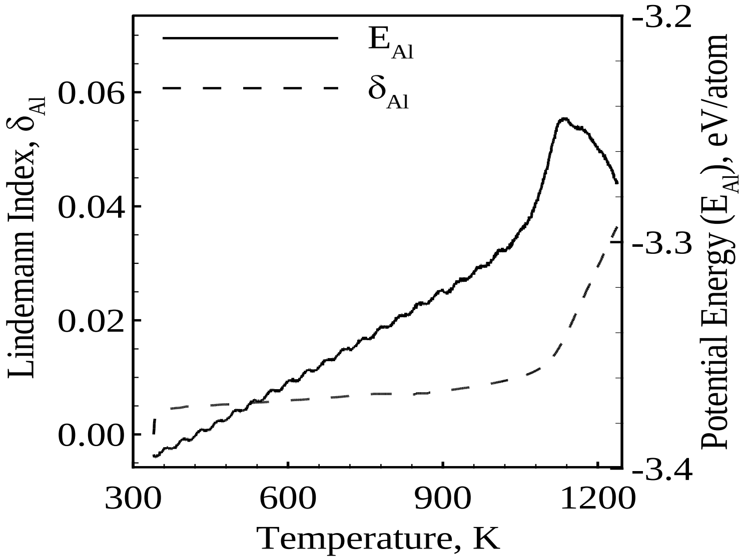

Figure 3.6: Lindemann index, δ_{Al}, and potential energy of the aluminum core as a function of temperature for a 14 nm particle with a 1 nm thick nickel shell.

theoretical studies (Mei & Lu 2007, Lu & Jin 2001). The enhanced thermal stability of an encapsulated core is attributed to the epitaxial core-shell interface and/or to the pressure build up (Mei & Lu 2007). In an uncoated nano-particle, the surface atoms have lower coordination numbers and undergo pre-melting. For a coated particle, the shell constrains the motion of the core atoms through low-energy epitaxy interface. Figure 3.7 shows the snapshots of the particle at 300 and 1100 K. Melting causes a significant change in the crystal structure. At 300 K, a well-defined order is present, but no such order is observed at 1100 K, indicating phase change of the core. Figure 3.8 shows the variation of the core radius with temperature and/or time. The core radius is defined as

$$r_c = \sqrt{\frac{5}{3N_{Al}} \sum_{i=1}^{N_{Al}} (r_i - r_{cm})^2}, \tag{3.1}$$

where r_{cm} is the position vector of the center of mass. At temperatures lower than the core

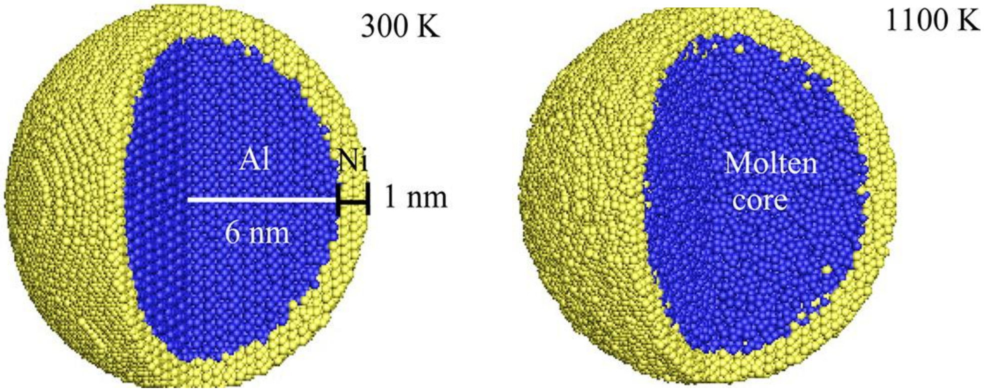

Figure 3.7: Snapshot of the particle before (300 K) and after (1100 K) core melting.

melting point, solid-state diffusion at significantly lower rates is observed. Diffusion occurs at much higher rates upon melting of the core. The sudden increase in the core radius at ~1000 K may be attributed to the melting of the core. The diffusion process, then, momentarily slows down before speeding up at higher temperatures. Figure 3.9

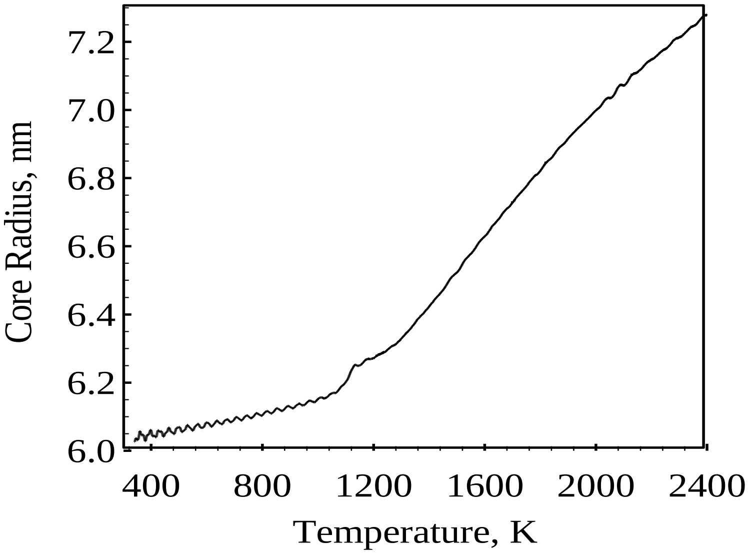

Figure 3.8: Core radius as a function of temperature (and/or time) for 14 nm particle with a 1 nm thick Ni shell.

shows the diffusion processes occurring in the particle over the temperature range of interest (300-2400 K). Aluminum atoms diffuse into the shell and nickel atoms diffuse into the core, converting the core-shell structured particle into a homogeneous alloyed particle. The diffusion processes prevail upon melting due to the higher mobility of the melted atoms. Note that complete homogenization is not observed at 2400 K, suggesting that longer time is required for complete mixing of the core and shell atoms. Figure 3.10

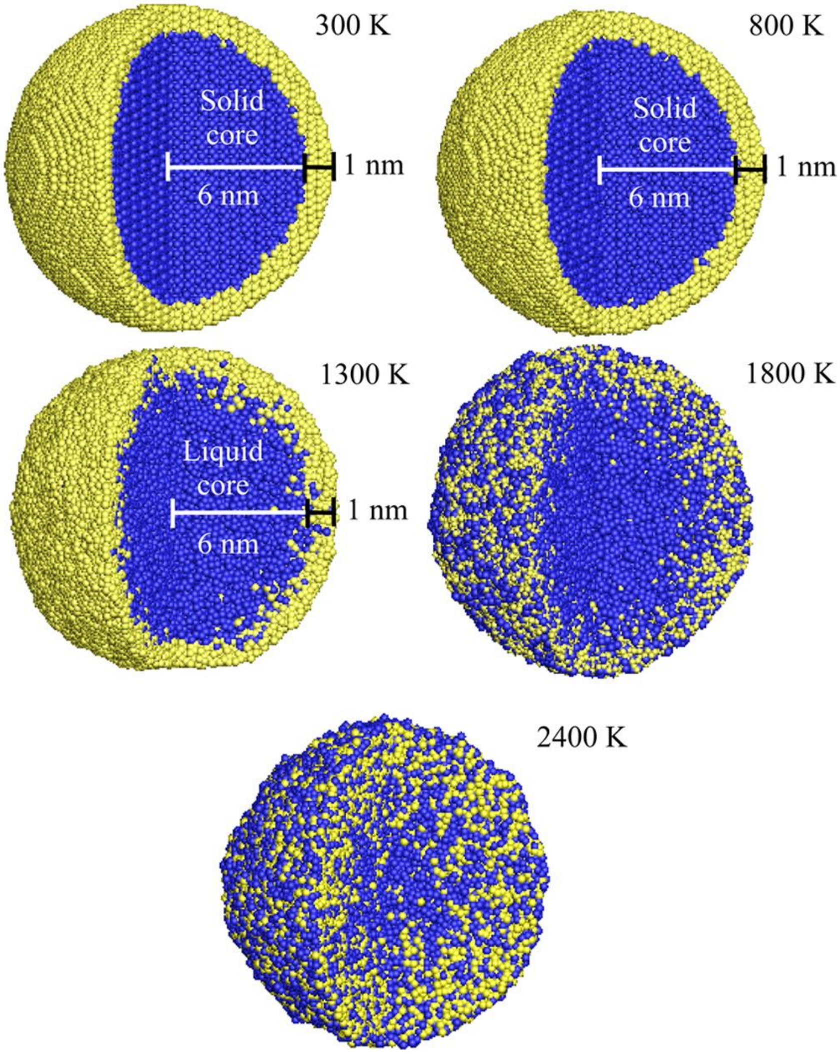

Figure 3.9: Snapshots of 14 nm particle showing melting and diffusion processes.

shows the variation of the average potential energy of the particle with temperature and/or time. The potential energy rises, attains a plateau, and then decreases. This trend is a characteristic of the core-shell particle structure, and is not observed for nascent particles. The result suggests the formation of low-energy species from the exothermic inter-metallic reactions. The inter-metallic species formed depends on the particle temperature and Ni-Al atomic ratio. For the present case, the Ni-Al phase diagram suggests that the reaction can be written as

$$\mathrm{Ni} + \mathrm{Al} \rightarrow \mathrm{NiAl}. \qquad (3.2)$$

The heat of formation of NiAl at room temperature is -62 kJ/mol (Hu & Nash 2005). The initial rise in the potential energy is caused by the transfer of energy from the heat reservoir to the particle (external heating). The plateau represents the stage at which this energy supply is counterbalanced by the formation of the low-energy inter-metallic species, NiAl. As a result, it is clear that the reactions begin upon melting of the

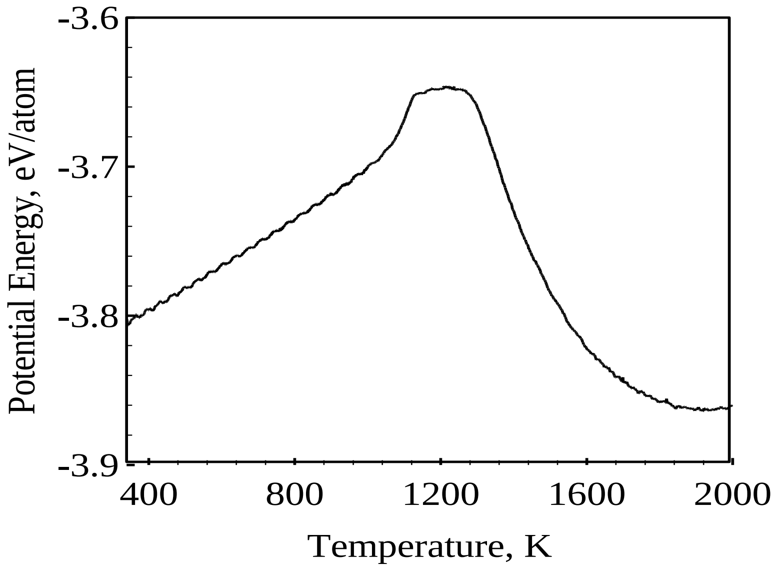

Figure 3.10: Average potential energy of the particle as a function of temperature (and/or time) for core diameter of 12 nm and shell thickness of 1 nm.

aluminum core. The subsequent decrease (which is not observed for single component systems) indicates the preponderance of the inter-metallic reactions. Note that the interfacial aluminum atoms mix with nickel atoms even at room temperature. If the particle is heated externally to a temperature at which the reactions gain significance, it can ignite, provided that the rate of chemical heat generation is greater than that of heat loss to the ambient environment. An energy balance is performed to estimate the equilibrium temperature of the particle (upon completion of the inter-metallic reactions) at adiabatic conditions. The result is compared with the value obtained from the MD simulation. The thermodynamic energy balance takes the form

$$H_{reac}\left(T_i\right)=H_{prod}\left(T_{ad}\right), \tag{3.3}$$

where H_{reac} is the enthalpy of the reactants calculated at an initial temperature, T_i, and H_{prod} the enthalpy of the products evaluated at the adiabatic reaction temperature, T_{ad}. The initial temperature is taken as 1250 K, which corresponds to the point at which the potential energy begins to decrease. The enthalpy of the reactants, H_{reac}, is given by

$$H_{reac}=H_{Al}^{1250K}+H_{Ni}^{1250K}+H_{m,Al}. \tag{3.4}$$

The enthalpies of aluminum and nickel consist only of the thermal contribution, since the chemical energy is taken as zero. For simplicity, the specific heat capacities of Al and Ni are taken as 24 J/mol and 26 J/mol, respectively. The resulting enthalpies of Al and Ni are 22.85 and 24.82 kJ/mol, respectively. The enthalpy of melting of aluminum is taken as 10.71 kJ/mol. The enthalpy of the products is expressed as

$$H_{prod}=\left(1-\frac{t_i A}{V}\right)H_{f,NiAl}^{298K}+C_{p,NiAl}\left(T_{ad}-298\right)+H_{m,NiAl} \tag{3.5}$$

where A is the interfacial area, V the core volume and t_i the thickness of the interfacial zone. The factor in the first term of the left hand side of Eq. (3.5) accounts for the fact that the interfacial core atoms participate in alloying reactions prior to melting of the core, thereby decreasing the energy content of the particle. The fraction of the core volume that has already reacted depends on the interfacial area-to-core volume ratio and the thickness of the interfacial reaction zone. The latter is approximated to be 0.7Å based on the study of aluminum-coated nickel particles (Henz, Hawa & Zachariah 2009). The specific heat and enthalpy of melting of NiAl are taken as 110 J/mol-K and 63 kJ/mol, respectively (Alexander et al. 2009). The equilibrium temperature calculated using Eqs. (3.4) and (3.5) is 2388 K. In other words, the particle is self-heated from 1250 to 2388 K due to the heat release from inter-metallic reactions. Employing temperature-averaged specific heat results in a reaction temperature of 2396 K. If the latent heat of melting of Ni is considered in the reactant energy, the predicted reaction temperature is 2700 K.

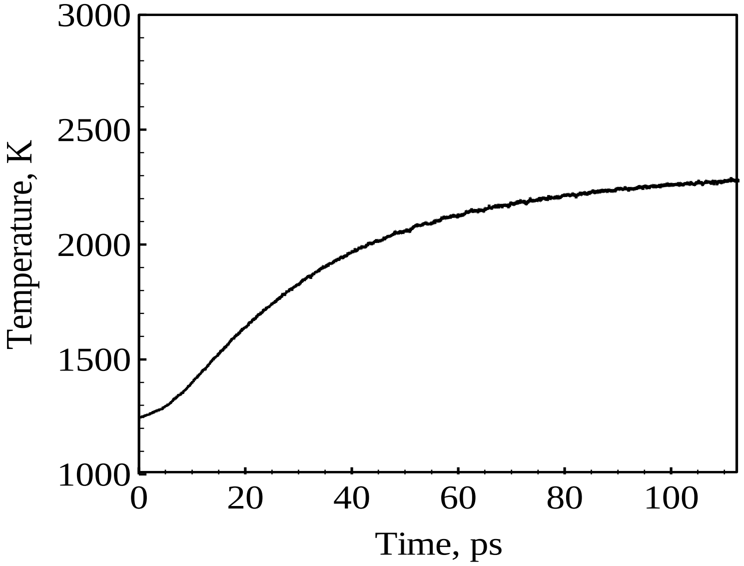

Figure 3.11: Temporal evolution of the particle temperature for core diameter of 12 nm and 1 nm thick shell.

Note that the choice of initial temperature has a nearly linear effect on the final reaction temperature. For example, decreasing the initial temperature from 1250 to 1150 K causes the reaction temperature to decrease by about 90 K. Figure 3.11 shows the variation of the temperature of the particle with time under adiabatic conditions calculated using MD simulations. The initial position and velocities of atoms are those obtained from the heating simulation in an NPT ensemble at 1250 K. The particle is heated from 1250 to ~2300 K due to exothermic intermetallic reactions of aluminum and nickel atoms over a period of 100 ps. One of the reasons for the discrepancy is that equilibrium is not attained within a time period of ~100 ps. After a time period of 50 ps, the temperature increases very slowly. It is also important to note that the atomic species are no longer expected to interact with the ground state electronic configuration but with an excited one at higher temperatures. Therefore, classical many-body potentials reproduce interaction forces only with modest accuracy, and ab initio methods should be applied. The particle temperature increases by ~1000 K over a time period of ~100 ps. The resulting *intrinsic* heating rate is ~ 10^{13} K/s.

3.2.2 Effect of Core Size

The effect of core size is studied in the diameter range of 3-12 nm and for a fixed shell thickness of 1 nm. Figure 3.12 shows the variation of the melting point of the core with the core diameter for a shell thickness of 1 nm. It increases from 775 to 1000 K when the core diameter increases from 3 to 12 nm. Melting point elevation is, thus, observed for all core sizes. The fact that the core melting point increases with increasing core size indicates that core melting is a heterogeneous process beginning at the interface.

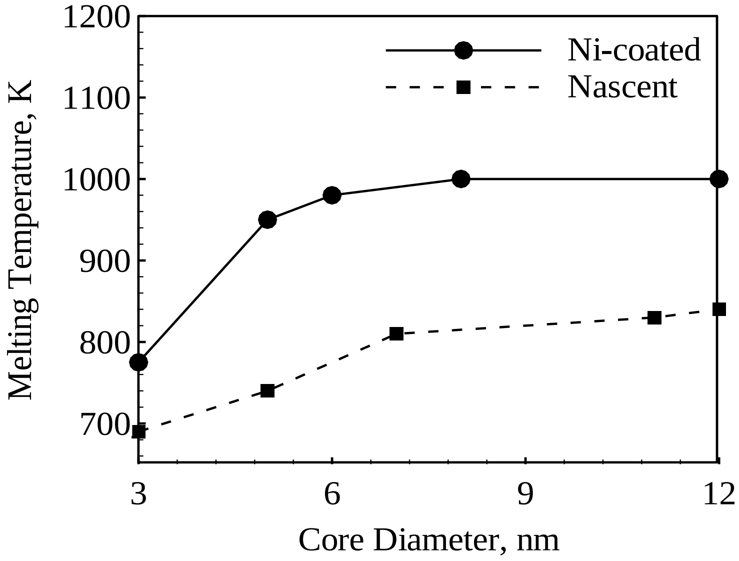

Figure 3.12: Effect of core diameter on the melting point of the core for a 1 nm shell.

Figure 3.13 shows the snapshots of 8 nm particle colored by thermal displacement at different temperatures. The atomic thermal displacement is given by

$$\delta_{t,i} = \sqrt{\left(r_i - r_{0,i}\right)^2}, \tag{3.6}$$

where *r* denotes the position vector. The subscripts *i* and 0 refer to atom *i* and the initial state, respectively. The thermal displacement is a measure of lattice disorder induced by thermal motion. It is expected to increase abruptly during melting. As can be seen, the nucleation of the liquid phase begins at the core-shell interface and the melting front propagates to the interior region of the core. The fact that heterogeneous nucleation at the interface dominates melting of superheated nano-particles is consistent with the results of MD simulations of nickel-coated silver particles (Lu & Jin 2001). Figure 3.14 shows the variation of the core radius with temperature (and/or time) for different core sizes. For a 3 nm core, the diffusion rate of aluminum atoms increases significantly at approximately

1300 K, a phenomenon that is not related to the melting of the core, since the core melts at a much lower temperature. The nickel shell, however, melts at 1325 K (see Section 3.2.3), which is significantly lower than the bulk melting point of nickel, 1728 K. The

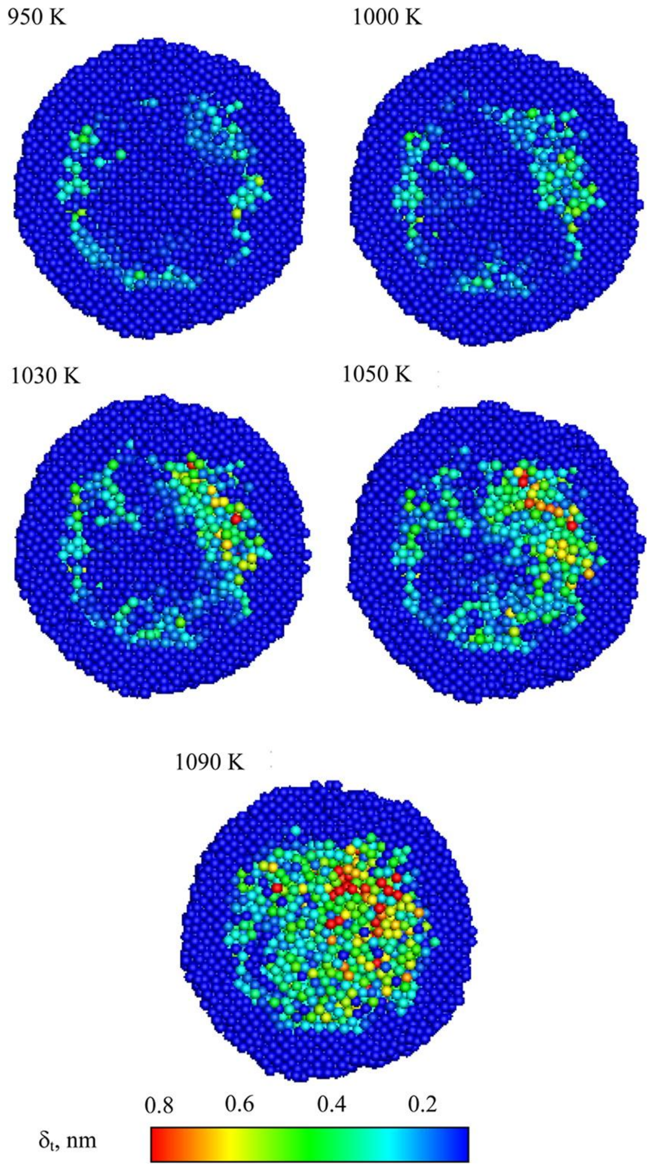

Figure 3.13: Particle snapshots showing thermal displacement of core atoms at different temperatures for 8 nm particle with 1 nm shell.

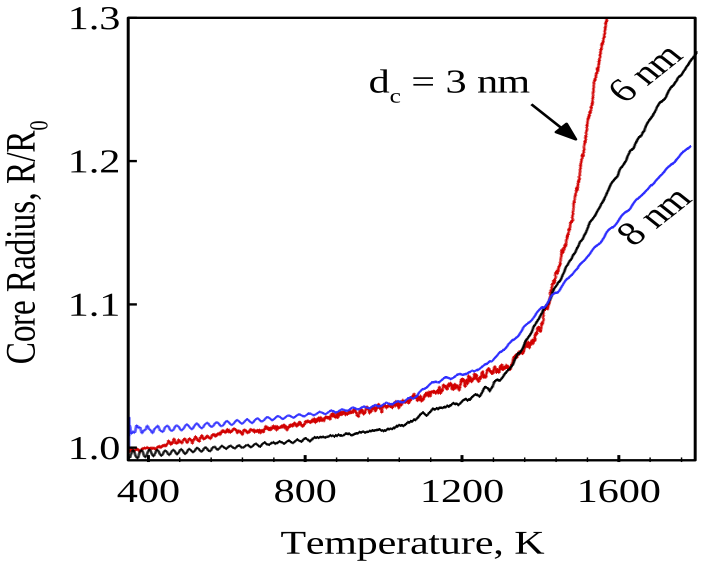

Figure 3.14: Core radius (normalized with respect to initial value) as a function of temperature (and/or time) for particles with a 1 nm shell.

diffusion of core atoms thus accelerates upon melting of the shell. For a spherical shell, liquid phase nucleation may begin at the outer surface and/or core-shell interface. Furthermore, nano-scale shells encapsulating molten clusters are thermally less stable than spherical particles of the same size (Mei & Lu 2007). As a result, melting points of spherical particles and shells may not be the same. Figure 3.15 shows the variation of the average potential energy of the particle with temperature and/or time. The magnitude by which the potential energy decreases is proportional to the core size. For smaller cores, fewer number of aluminum atoms react with nickel atoms (For a core diameter of 3 nm, only 12 % of atoms is aluminum). As result, there is significant of amount of nickel atoms in the particle that remain unreacted. Furthermore, the average potential energy reflects the property of the shell than the core for smaller core sizes, since the aluminum atomic fraction decreases with decreasing core size. The cohesive energy of nickel is

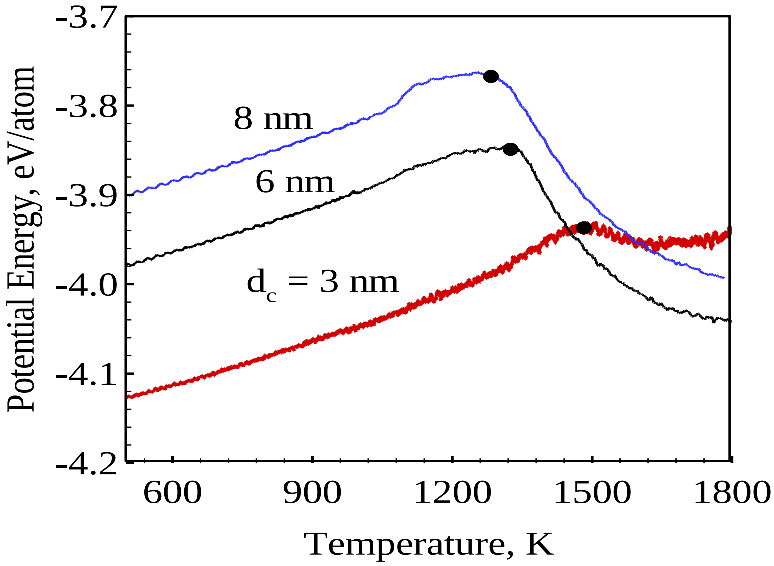

Figure 3.15: Average potential energy of the particle as a function of temperature (and/or time) for different core diameters and 1 nm shell.

approximately equal to that of Ni-Al inter-metallic species.The temperature at which the potential energy begins to drop decreases with increasing core size. One possible reason is that the diffusion is facilitated for larger cores at slightly lower temperatures. Note that the "averaging" of the potential energy may also affect the trend.

Simulations in an isochoric-isoenergetic ensemble are performed to calculate the adiabatic reaction temperature of the particle for different core sizes. Figure 3.16 shows the effect of core diameter on the adiabatic reaction temperature of the particle for a shell thickness of 1 nm. The reaction temperature (or temperature rise) decreases with decreasing core size. To understand the relevant physicochemical phenomena, a companion thermodynamic analysis is also performed. Figure 3.17 shows the equilibrium phase diagram for the Ni-Al system (Massalski 1992). The particle composition determines the final inter-metallic product. For 3 nm core, the aluminum atomic fraction

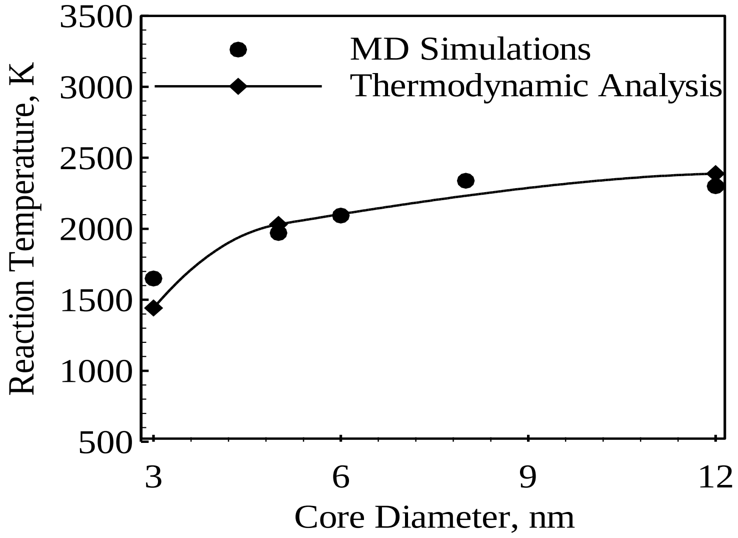

Figure 3.16: Effect of core diameter on adiabatic reaction temperature of particles for a shell thickness of 1 nm.

is 0.12 (particle is nickel-rich). According to Ni-Al phase diagram, the product is a mixture of Ni_3Al and Ni for an aluminum atomic fraction of 0.12. The chemical reaction can thus be expressed as

$$7.2\mathrm{Ni} + \mathrm{Al} \rightarrow \mathrm{Ni_3Al} + 4.2\mathrm{Ni}. \tag{3.7}$$

In the present analysis, the specific heat, enthalpy of fusion and heat of formation of Ni_3Al are taken to be 130 J/mol-K, 50 kJ/mol, and -164 kJ/mol, respectively (Liu & Dupont 2003). The results (shown in Fig. 3.16) support the fact that the adiabatic reaction temperature decreases with decreasing core size. This can be attributed to the following reasons. Firstly, residual Ni atoms that do not participate in inter-metallic reactions are present in the product particle. Secondly, the fraction of interfacial core atoms increases with decreasing particle size. As a result, a greater percentage of core atoms have undergone interfacial premixing process, thereby decreasing the energy content of the particle. The core size, thus, significantly affects the energetics of nickel-coated nano-aluminum particles.

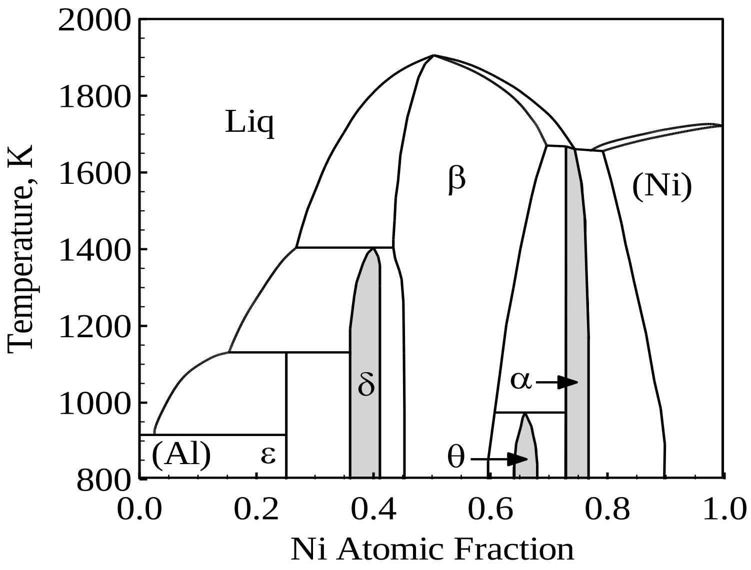

Figure 3.17: Ni-Al phase diagram (ε: *Ni*Al_3, δ*:* Ni_2Al_3, β: NiAl, θ: Ni_5Al_3, α: Ni_3Al).

3.2.3 Effect of Shell Thickness

The effect of shell thickness is examined in the range of 0.5-3.0 nm. Figure 3.18 shows the melting point of the aluminum core as a function of shell thickness. The core melting point is not significantly affected by variations in the shell thickness in the size range of concern. In the present study, spallation of the nickel shell due to the tensile stress exerted by the aluminum core was not observed. For homogeneously heated aluminum particles, the core pressure is about 1 GPa (Henz 2009). Levitas (Levitas 2009) proposed melt dispersion mechanism, which is valid at very high heating rates (> 10^6 K/s). According to this theory, the shell is ruptured by the tensile stress exerted by the core and the molten aluminum clusters are dispersed in the surrounding environment. For crystalline materials, the theoretical strength is $\sigma_{th} = E/10$, where E is the Young's

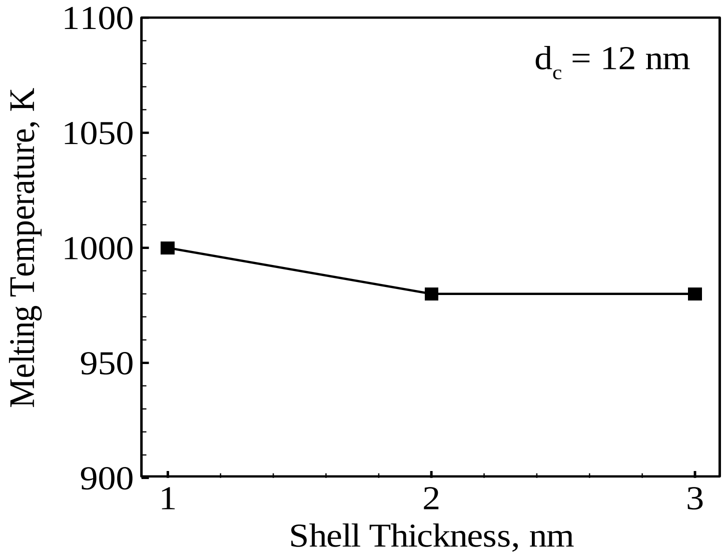

Figure 3.18: Effect of shell thickness on the melting temperature of the 12 nm core.

modulus (Levitas et al. 2007). For nickel, the resulting strength value is 17 GPa, which is significantly greater than the core pressure. It is, thus, not surprising that spallation of nickel shell is not observed. In real materials, defects in the form of cracks and voids may lower the tensile strength. The strength is, however, expected to increase with increasing heating rate (Levitas et al. 2007). In addition, stress concentration phenomenon may have weak effect at nano-scales and high heating rates (Levitas et al. 2007). As a result, homogeneous spallation of the shell at the theoretical strength may occur for real materials. Figure 3.19 shows the core radius as a function of temperature and/or time for a core diameter of 3 nm and shell thickness of 0.5, 1, 2, and 3 nm. Diffusion is facilitated for thinner shells. For a 0.5 nm shell, the core radius increases significantly upon melting of the core at ~800 K. The core atoms, however, diffuse out at 1400, 1500, and 1600 K for shell thickness of 1, 2 and 3 nm, respectively. The ignition temperature of a 3 nm aluminum particle increases from 800 to 1600 K, when the nickel shell thickness

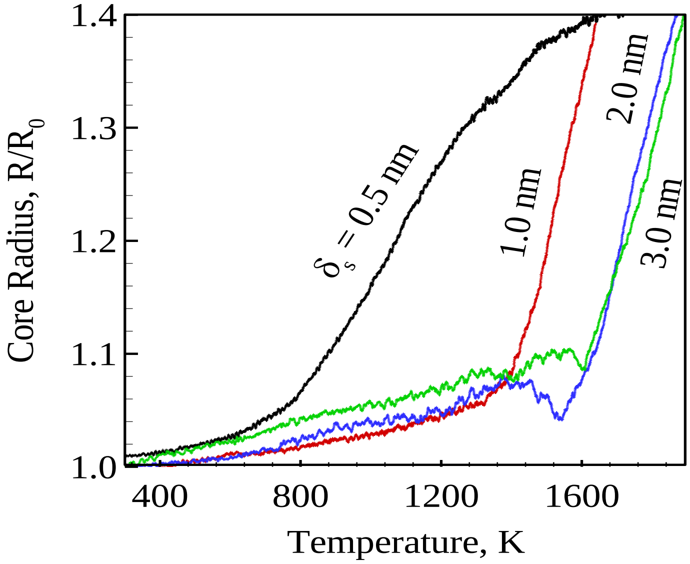

Figure 3.19: Variation of the core radius with temperature (and/or time) for a core diameter of 3 nm and shell thickness in the range of 0.5-3 nm.

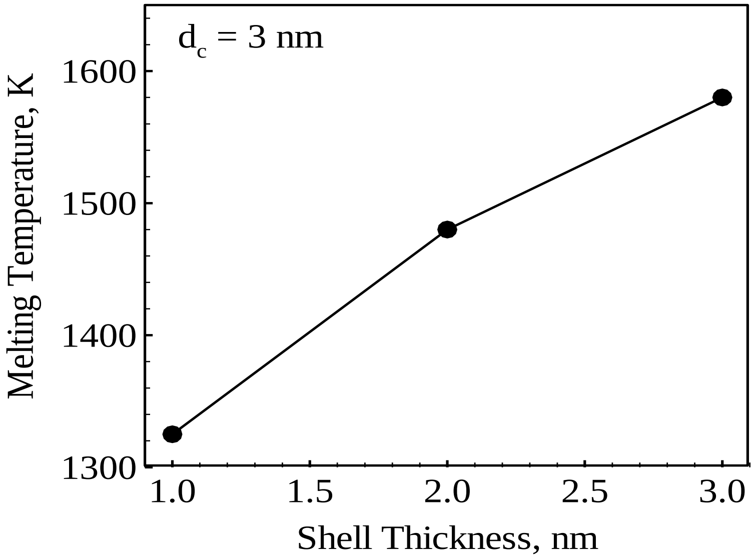

Figure 3.20: Effect of shell thickness on the melting temperature of the nickel shell for core diameter of 3 nm.

increases from 0.5 to 3.0 nm. Figure 3.20 shows the effect of shell thickness on the melting point of the shell for a core diameter of 3 nm. The shell melting point increases from 1325 to 1580 K, when the thickness increases from 1 to 3 nm. The melting point of the shell is approximately equal to the bulk value for shell thickness greater than 3 nm. A qualitatively similar trend is observed for other core sizes. It is obvious that shell melting plays an important role in dictating the diffusion and reaction processes in nickel-coated nano-aluminum particles.

The diffusion coefficient of aluminum atoms in a nickel shell is an important parameter, especially from the standpoint of ignition and combustion analyses of nickel-coated aluminum particles. In the present study, the diffusion coefficient is calculated for a 7 nm particle with a 0.5 nm shell. Figure 3.21 shows the effect of temperature and/or time on the diffusion coefficient of aluminum atoms in the nickel shell. The diffusion

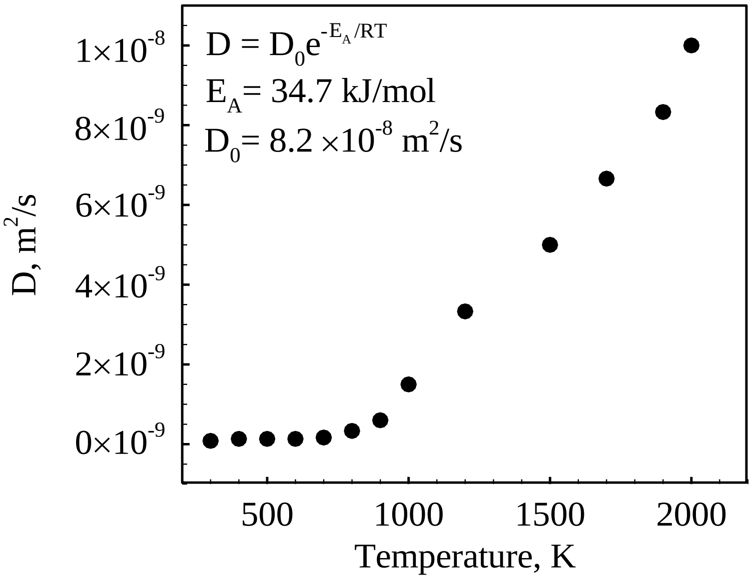

Figure 3.21: Effect of temperature (and/or time) on the diffusion coefficient of aluminum atoms in nickel shell for a 7 nm particle with a 0.5 nm shell.

coefficient increases slowly at temperatures lower than the core melting point. A sudden increase is observed upon melting of the core. It exhibits a temperature dependence of the form

$$D = D_0 \exp\left(-\frac{E_A}{RT}\right), \tag{3.8}$$

where E_A is the activation energy and D_0 is the pre-exponential factor. The curve-fit indicates a value of 34.7 kJ/mol for the activation energy and 8.2×10^{-8} m^2/s for the pre-exponential factor. Note that the activation energy and pre-exponential factor may also depend on the core diameter and shell thickness. The present work indicates that the dimensions of the core and shell significantly influence the properties of nickel-coated nano-aluminum particles. It is of scientific interest to compare the physicochemical behavior of nano-sized nickel-coated aluminum particles and aluminum-coated nickel particles.

3.3 Summary

The major results of the analysis presented in this chapter are summarized as follows:

- The size dependence of melting temperature of aluminum and nickel particles is analyzed. The results of various experimental and theoretical studies are gathered and compared with those of the present MD simulations. Reasonably good agreement is obtained. The predicted melting temperatures are lower than the experimental data at high heating rates and agree reasonably well with the low heating rate values. Since the melting point increases with increasing heating rate, it may be concluded that the Cleri-Rosato potential function slightly under predicts the melting temperature of aluminum and nickel particles. For nickel, the calculated melting points are more accurate than the values currently available in the literature.

- MD simulations of nickel-coated nano-aluminum particles indicate that the aluminum core is superheated above the melting point of nascent aluminum particles. This is consistent with the findings of previous experimental and theoretical studies. The superheating phenomenon is attributed to the epitaxial interface and/or pressure build up. Melting temperature of core increases with increasing core diameter, from 775 K at 3 nm to 1000 K at 12 nm. It is nearly independent of shell thickness in the range of 1-3 nm. Analysis reveals that the core undergoes heterogeneous melting and the nucleation of the liquid phase begins at the core-shell interface.

- Melting temperature of the nickel shell increases with increasing shell thickness, from 1325 K at 1 nm to 1580 K at 3 nm. This pattern is analogous to that observed for spherical particles.

- Melting of the shell results in dramatic increase in the rate of diffusion of core atoms. Diffusion is accompanied by nickel-aluminum inter-metallic reactions, which self-heat the particle under adiabatic condition. Majority of the heat release is expected to occur upon melting of the shell. This is of importance to particle oxidation in a chemically reacting gas.

- Diffusion coefficient is calculated as a function of temperature for a 6 nm aluminum particle covered by a nickel shell of thickness 0.5 nm. The curve-fit indicates a value of 34.7 kJ/mol for the activation energy and 8.19×10^{-8} m^2/s for the pre-exponential factor. These numbers are likely to vary depending on the core diameter and shell thickness.

- The predicted adiabatic reaction temperature increases with increasing core size, reaching a value of ~2300 K at a core size of 12 nm (for a fixed shell thickness of 1 nm). The lower reaction temperature (or temperature rise) for smaller cores is explained by the thermo-chemistry of Ni-Al reactions and loss of energy content due to interfacial premixing process.

CHAPTER 4

THERMO-CHEMICAL BEHAVIOR OF NANO-SIZED ALUMINUM-COATED NICKEL PARTICLES

The molecular dynamics simulation framework is used to study the thermo-chemical behavior of aluminum-coated nano-nickel particles. The results are useful for both material synthesis and propulsion applications. Comparison of the properties of nickel-coated aluminum particles and aluminum-coated nickel particles is also of pure scientific interest. The present study employs the embedded atom method to capture the interactions between the atoms. Analysis indicates that the parameter set employed in the study of nickel-coated aluminum particles (Table 2.1) does not give accurate predictions of the reaction temperature of aluminum-coated nickel particles. Note that this parameter set is widely used to study the properties of Ni-Al alloys. For aluminum-coated nickel particles considered in the present study, the reaction products are stoichiometric and Al-rich inter-metallic species. The parameters were obtained by fitting the potential function to the properties of B2-NiAl and nickel-rich Ni_3Al, which are of relevance only to nickel-coated nano-aluminum particles. As a result, we have chosen the parameter set developed by Papanicolaou et al. (Papanicolaou et al. 2003), which has been fitted to structural and thermodynamic properties of various Ni-Al species including the Al-rich species. It is important to note that the parameter sets developed by Papanicolaou et al. and Cleri and Rosato give qualitatively similar predictions of the melting and diffusion processes for nickel-coated aluminum and aluminum-coated nickel particles. Table 4.1 gives the parameter adopted in the present study.

Table 4.1: Parameters of the Cleri-Rosato potential function (Papanicolaou et al. 2003).

	Ni-Ni	Al-Al	Ni-Al
A(eV)	0.0741	0.0550	0.0949
ξ (eV)	1.4175	0.9564	1.4677
p	13.8297	10.9011	10.9486
q	2.2448	1.5126	3.8507
r_0 (Å)	2.4307	2.8310	2.7424

4.1 Pure Aluminum and Nickel

The predictive capability of the potential function is first tested for pure aluminum and nickel particles. Figure 4.1 shows the potential energy as a function of temperature for aluminum and nickel particles consisting of 10976 atoms. A gradual deviation from the linear trend at ~900 K marks the onset of surface melting for aluminum. For nickel,

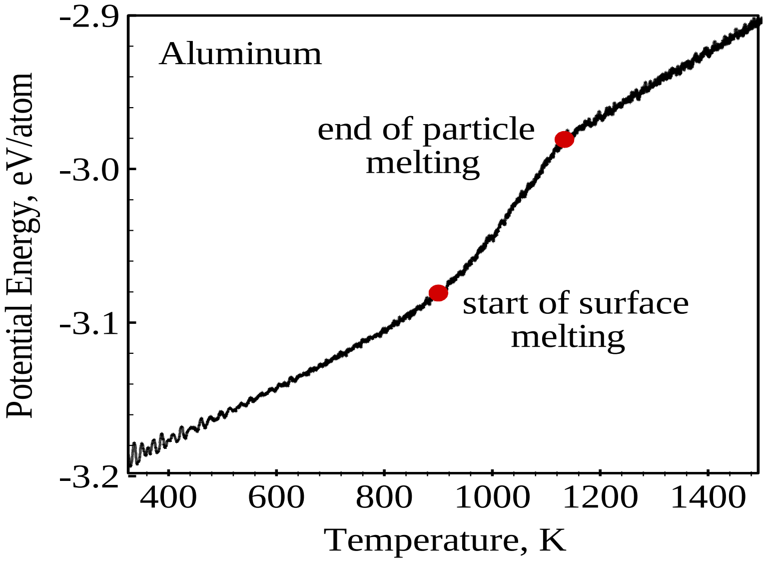

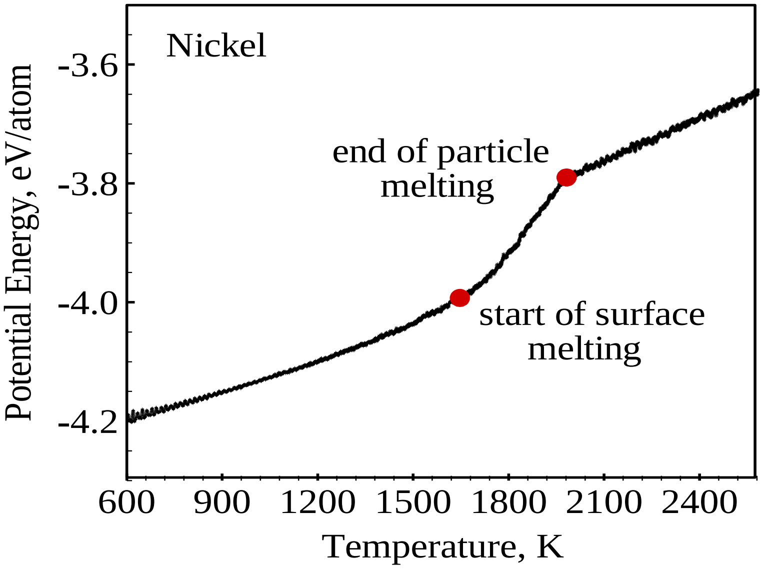

Figure 4.1: Variation of potential energy with temperature for 7 nm aluminum and 6 nm nickel particles (10976 atoms).

surface pre-melting begins at 1650 K. Note that the predicted melting temperatures predicted are greater than those obtained using the parameters developed by Cleri and Rosato. Figure 4.2 show the effect of particle size on the melting temperature of aluminum and nickel, respectively. The comparison with the results of previous MD simulations, experiments, and theoretical studies (Levitas & Samani 2011) are also shown in the figure. The calculated melting temperatures are greater than those obtained using the Cleri-Rosato parameter set, but agree reasonably with the counterparts of the glue potential (Puri & Yang 2007) for aluminum. Note that the heating rates in the present MD simulations (10^{13} K/s) are orders of magnitude greater than those in experiments (1-10^{6} K/s). It is, thus, not surprising that some of the predicted melting temperatures are greater than the experimental data. For nickel, the predictions are significantly greater than the values obtained by Qi et al. (Qi et al. 2001). It can be

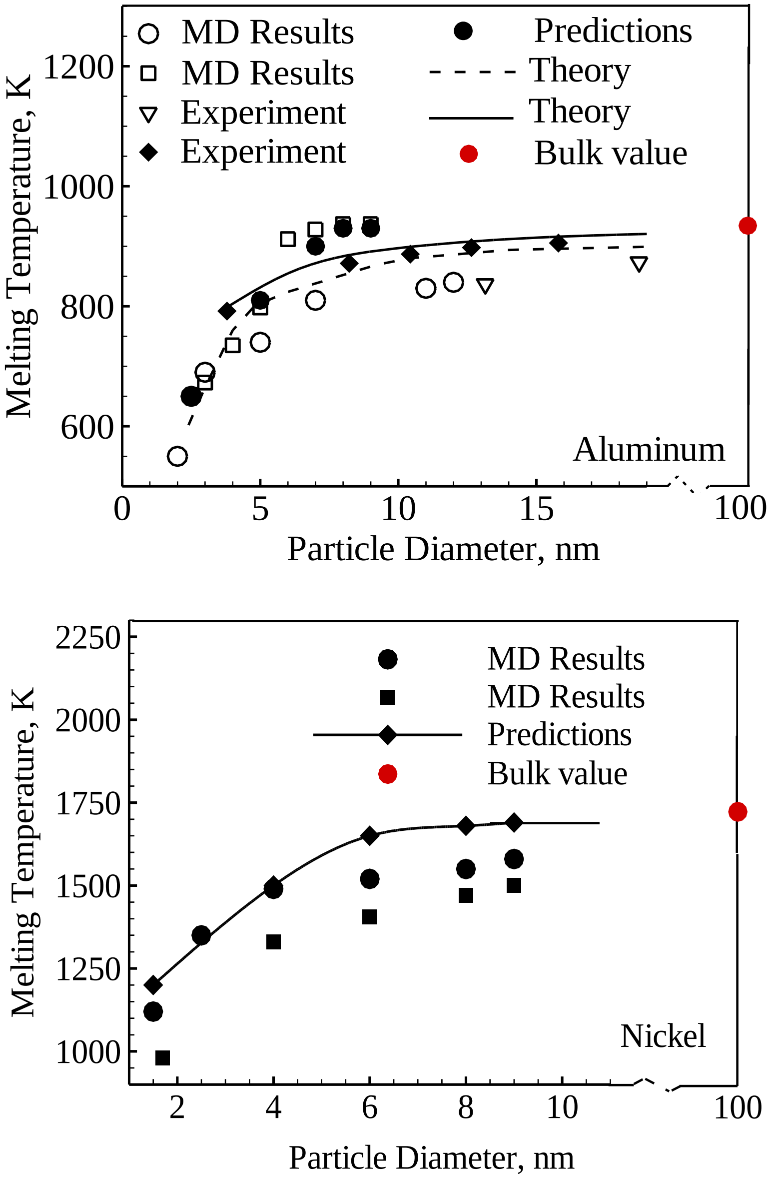

Figure 4.2: Effect of particle size on melting temperature of aluminum and nickel at nano-scales (Qi et al. 2001 (■), Puri & Yang 2007 (□), Sundaram, Puri & Yang 2013 (•, o), Lai, Carlsoon & Allen 1998(♦), Eckert et al. 1993 (∇)).

concluded that the parameter set developed by Papanicolaou et al. (Papanicolaou et al. 2003) offers the most accurate predictions of the melting temperature of aluminum and nickel particles.

4.2 Aluminum-Coated Nano-Nickel Particles

The thermo-chemical behavior of aluminum-coated nickel particles is investigated for different core diameters and shell thicknesses. Emphasis is placed on the particle melting behavior, diffusion characteristics, and inter-metallic reactions. Figure 4.3 shows the snapshot of the dissected particle. A spherical aluminum particle of known dimension is first generated. A spherical void is then created in the interior of the particle to accommodate the nickel core. The resulting particle is equilibrated at 300 K prior to the heating simulation. Table 4.2 shows the core diameter (d_c), shell thickness (δ_s), total number of atoms (N), and number of nickel atoms (N_{Ni}) of the particles chosen in the present study. The core diameter is in the range of 3-10 nm and different shell thickness of 0.5, 1.0, 2.0, and 3.0 are considered.

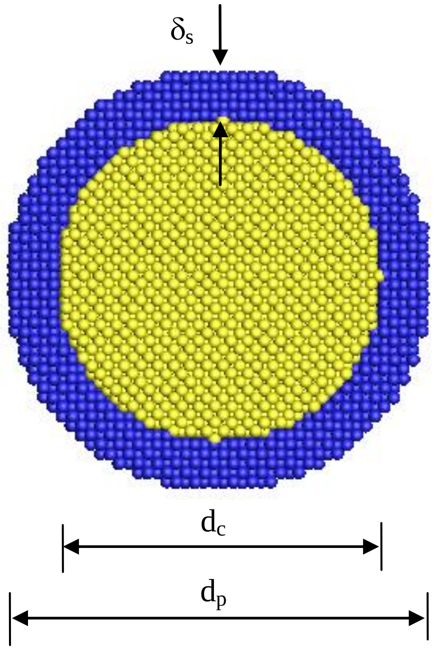

Figure 4.3: Snapshot of a dissected aluminum-coated nickel particle ($d_p = d_c + 2\delta_s$).

Table 4.2: Configuration of aluminum-coated nickel particles used in the present study.

Core diameter (d_c), nm	Shell thickness (δ_s), nm	Total number of atoms (N)	Number of nickel atoms (N_{Ni})
3	0.5	1919	874
3	1.0	3715	874
3	2.0	10252	874
3	3.0	21954	874
5	0.5	9642	6379
5	1.0	13973	6379
5	2.0	27099	6379
7	1.0	27832	15499
7	2.0	47082	15499
7	3.0	74675	15499
10	1.0	79233	53754

4.2.1 Baseline Simulation

To facilitate detailed discussion of the relevant physicochemical processes, a particle with core diameter of 3 nm and shell thickness of 2 nm is considered. Figure 4.4 shows the variation of the potential energy of the shell with temperature. The predicted melting temperature of 930 K is approximately equal to the bulk melting point of aluminum. The nickel-aluminum reactions are responsible for the drop in the potential energy upon melting of the shell. Figure 4.5 shows the snapshots of the particle colored by thermal displacement of the atoms. The snapshots indicate that the shell melting is a

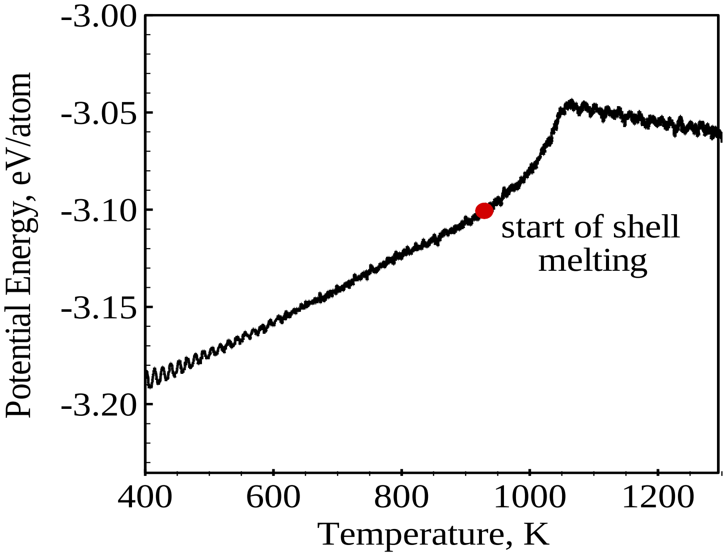

Figure 4.4: Potential energy of shell as a function of temperature for a particle with core diameter of 3 nm and shell thickness of 2 nm.

heterogeneous process in which the nucleation of the liquid phase begins at the particle surface. The melting front propagates towards the core-shell interface with increasing temperatures. Heterogeneous melting of the shell was also observed for nickel-coated aluminum particles. Figure 4.6 shows the variation of the core radius with temperature and/or time. The core radius is defined based on radius of gyration of the system of atoms

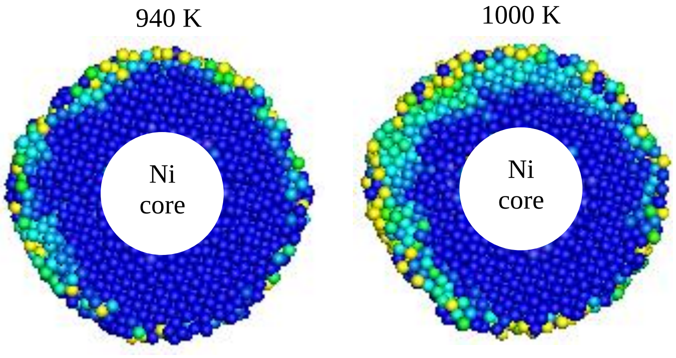

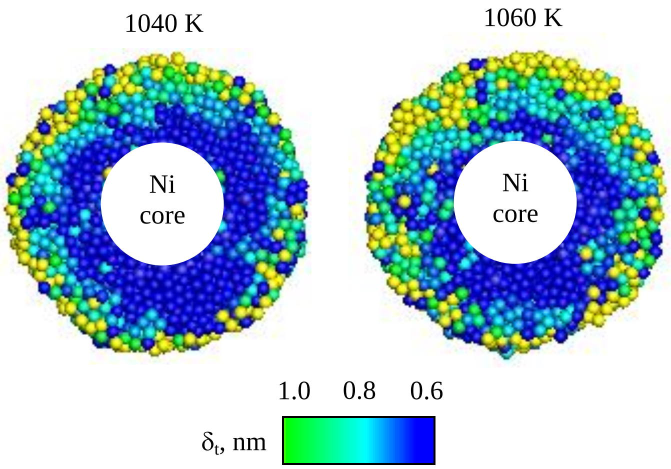

Figure 4.5: Snapshots of the particle colored by thermal displacement of shell atoms (dashed red curve: melting front; solid white circle: nickel core).

$$r_c = \sqrt{\frac{5}{3N_{Ni}} \sum_{i=1}^{N_{Ni}} \left(r_i - r_{cm}\right)^2}, \qquad (4.1)$$

where r_{cm} is the position vector of the center of mass. It increases negligibly in the temperature range of 300-900 K. It, however, rises sharply upon melting of the shell. Diffusion of nickel atoms is, thus, facilitated by the melting of the shell. Figure 4.7 shows the variation of the average potential energy of the particle with temperature and/or time. The potential energy increases, attains a plateau and then increases. The initial rise in the potential energy is caused by the energy transfer from the heat reservoir to particle. The plateau represents the stage at which the energy supply is counterbalanced by formation of low-energy species due to inter- metallic reactions. The ensuing increase in potential energy indicates heating of a homogeneous (alloyed) particle. Note that the potential energy does not decrease significantly, which may

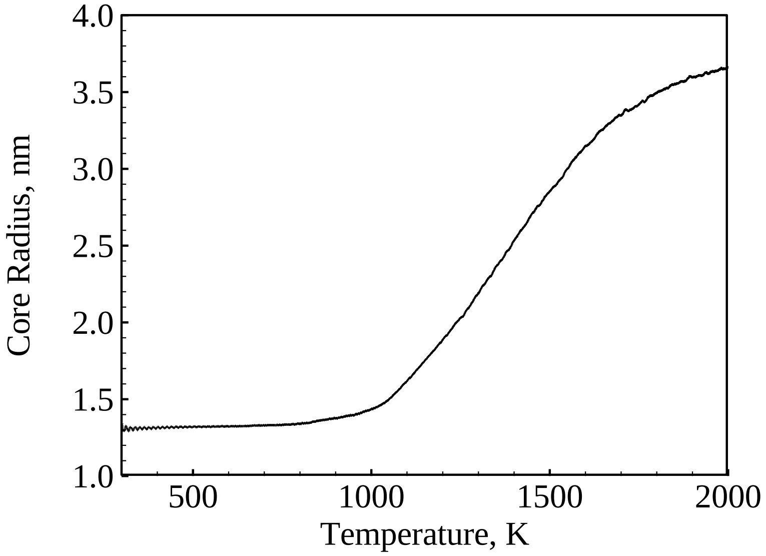

Figure 4.6: Variation of core radius with temperature (and/or time) for particle with core diameter of 3 nm and shell thickness of 2 nm.

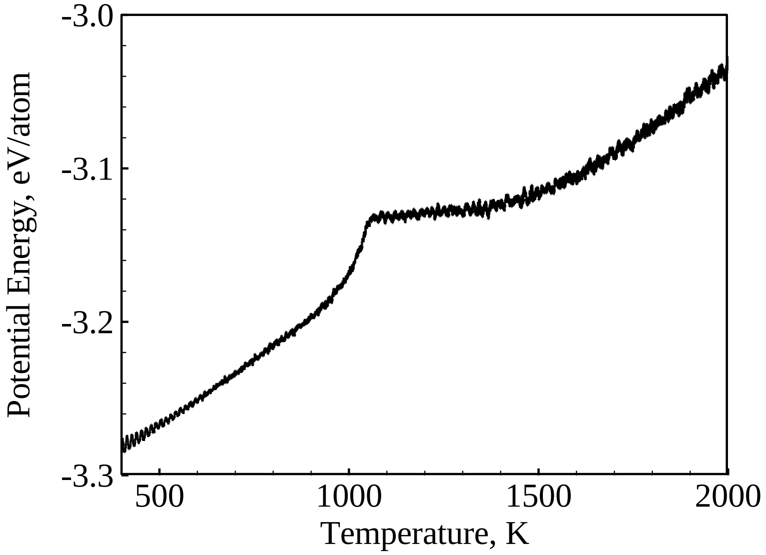

Figure 4.7: Variation of potential energy with temperature (and/or time) for particle with core diameter of 3 nm and shell thickness of 2 nm.

suggest that the chemical energy release is relatively low. Figure 4.8 shows the snapshots of the particle at different temperatures. At 900 K, a well-defined structural order characteristic of the solid state is observed. No such order is present in the shell at 1100 K, thereby suggesting that the shell is in liquid state. Note that the predicted melting temperature of the shell is ~930 K. The diffusion of nickel atoms, which occurs at

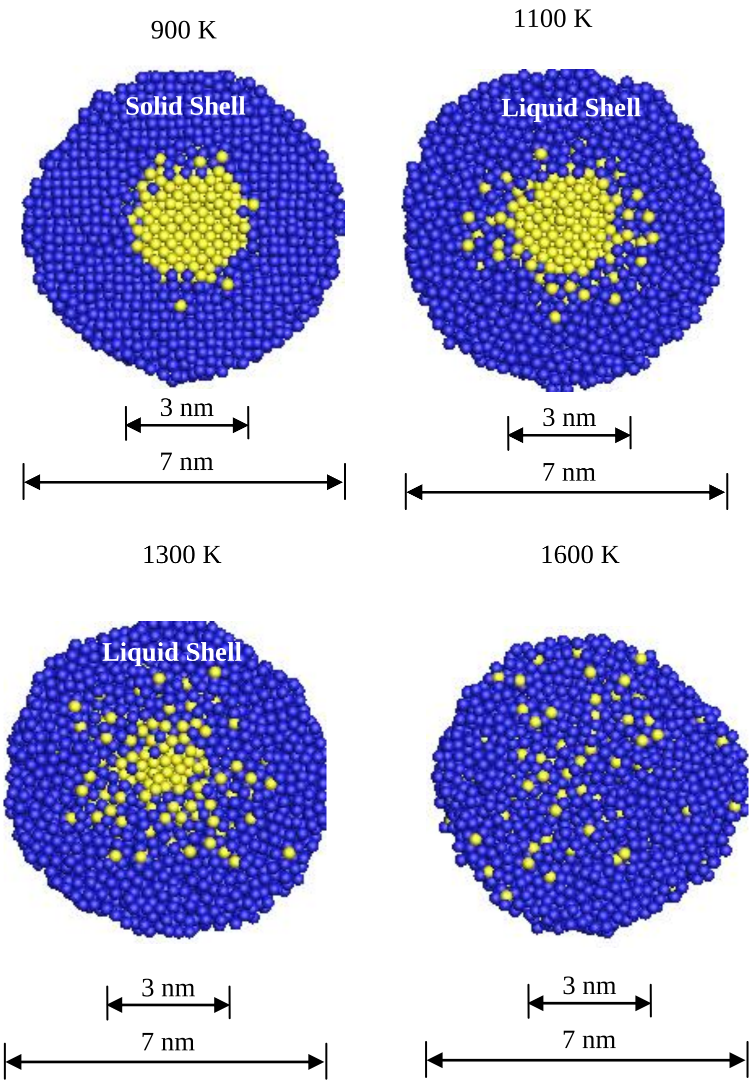

Figure 4.8: Particle snapshots at different temperatures showing melting and diffusion processes.

temperatures greater than the melting point of the shell, causes the dissolution of core-shell particle structure and formation of a homogeneous (alloyed) particle. The observed physicochemical phenomena bear close resemblance to those of nickel-coated aluminum particles with the exception that the shell melts before the core. In both cases, diffusion of core atoms is promoted upon melting of the shell (the core melting process will be discussed in Section 4.2.2).

Isochoric-isoenergetic MD simulations are performed to analyze the inter-metallic reactions that result in self-heating of the particle in adiabatic condition. The resulting adiabatic reaction temperature is compared with the value obtained using the thermodynamic energy balance analysis. The products of aluminum-nickel reaction depend on the particle composition (Ni:Al atomic ratio) and temperature. In the present case, the atomic fraction of nickel is 0.085. As a result, the inter-metallic reaction can be expressed as:

$$10.72\mathrm{Al} + \mathrm{Ni} \rightarrow \mathrm{NiAl_3} + 7.72\mathrm{Al}. \tag{4.2}$$

The thermodynamic energy balance is given by

$$H_{reac}\left(T_i\right) = H_{prod}\left(T_{ad}\right), \tag{4.3}$$

where H_{reac} is the enthalpy of the reactants calculated at an initial temperature, T_i, and H_{prod} the enthalpy of the products evaluated at the adiabatic reaction temperature, T_{ad}. The initial temperature is taken as 1050 K. The enthalpy of the reactants, H_{reac}, is given by

$$H_{reac} = 10.72 H_{Al}^{1050K} + H_{Ni}^{1050K} + 10.72 H_{m,Al}. \tag{4.4}$$

The enthalpy of melting of aluminum is taken as 10.71 kJ/mol. The resulting reactant enthalpy is 327.8 kJ/mol. The total enthalpy of the products is expressed as

$$H_{prod} = \left(1 - \frac{t_i A}{V}\right) H_{f,NiAl_3}^{298K} + \left(C_{p,NiAl_3} + 7.72C_{p,Al}\right)\left(T_{ad} - 298\right) + H_{m,NiAl_3} + 7.72H_{m,Al} \qquad (4.5)$$

where A the interfacial area, V the core volume and t_i the thickness of the interfacial zone. The specific heat, enthalpy of melting, and heat of formation of $NiAl_3$ are taken as 115 J/mol-K, 38 kJ/mol, and -150.6 kJ/mol respectively (Morsi 2001). The equilibrium temperature calculated by equating Eqs. (4.4) and (4.5) is 1420 K. In other words, the particle is self-heated from 1050 to 1420 K due to the heat release from inter-metallic reactions. Figure 4.9 shows the variation of the temperature of the particle with time under adiabatic condition calculated using isochoric-isoenergetic MD simulations. The initial position and velocities of atoms are those obtained from the constant pressure heating simulation at 1050 K. The MD simulation result indicates that the particle is heated from 1050 to 1540 K during a time period of 100 ps. The relatively low temperature rise can be partly attributed to the presence of unreacted aluminum atoms in the particle.

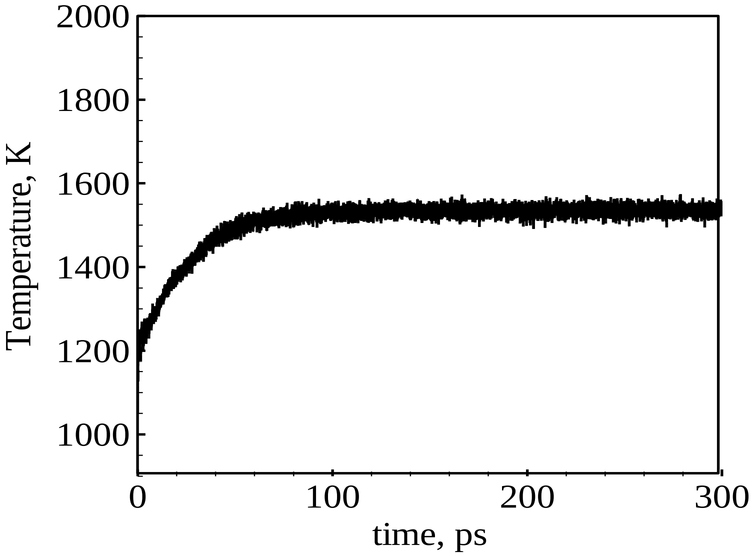

Figure 4.9: Temporal variation of particle temperature in adiabatic condition.

4.2.2 Effects of Core Size and Shell Thickness

A systematic analysis is performed to determine the effects of core size and shell thickness on the relevant physicochemical phenomena. Figure 4.10 shows the variation of the melting temperature of the shell with shell thickness for a core diameter of 7 nm. It increases with increasing shell thickness, from 750 K at 1 nm to 960 K at 3 nm. A similar trend was observed for other values of core diameters considered in the present study. For nickel-coated aluminum particles, the melting temperature of the nickel shell increases from 1325 to 1580 K, when the shell thickness increases from 1 to 3 nm. A thicker shell melts at a higher temperature, since the percentage of surface atoms decreases with increasing shell thickness. Note that the melting temperature is approximately equal to bulk value for shell thicknesses greater than 2 nm. Figure 4.11 shows the melting point of the shell as a function of core diameter for a shell thickness of 2 nm. It increases with increasing core diameter, from 930 K at 3 nm to 960 K at 7 nm. The core size exerts

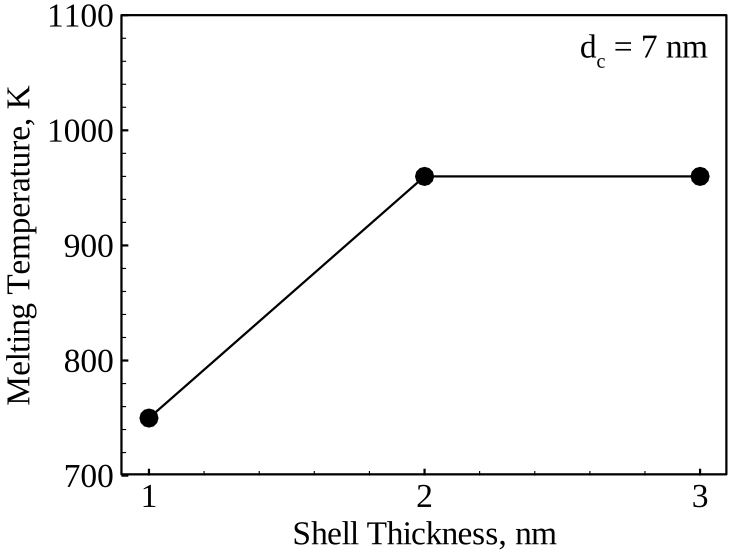

Figure 4.10: Effect of shell thickness on the melting temperature of shell for a core diameter of 7 nm.

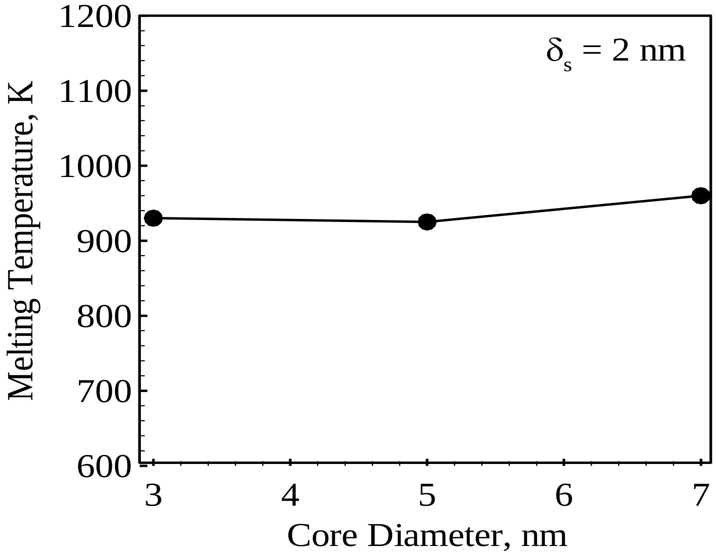

Figure 4.11: Variation of shell melting point with core diameter for a 2 nm shell.

relatively weak effect on the shell melting point. It is imperative to explore the dependence of the surface-area-to-volume ratio of the shell on the core size, since melting of the shell is a heterogeneous process beginning at the outer surface of the particle. The result is shown in Fig. 4.12. The shell thickness is assumed to be 2 nm. The surface-area-to-volume ratio of the core increases by an order of magnitude, when the core diameter decreases from 10 to 1 nm. For a spherical shell, it increases only by a factor of two. It is, thus, reasonable that the melting point of the shell bears a relative weak dependence on the core size. Figure 4.13 shows the potential energy of the core as a function of temperature for core diameter of 10 nm and shell thickness of 1 nm. The core begins to melt at a temperature of 1730 K, which is nearly the bulk melting point of nickel. The melting point of the core increases with increasing core diameter, from 1500 K at 7 nm to 1730 K at 10 nm. For smaller cores, it was difficult to clearly ascertain the melting point partly because inter-metallic reactions take place during the melting process. The melting

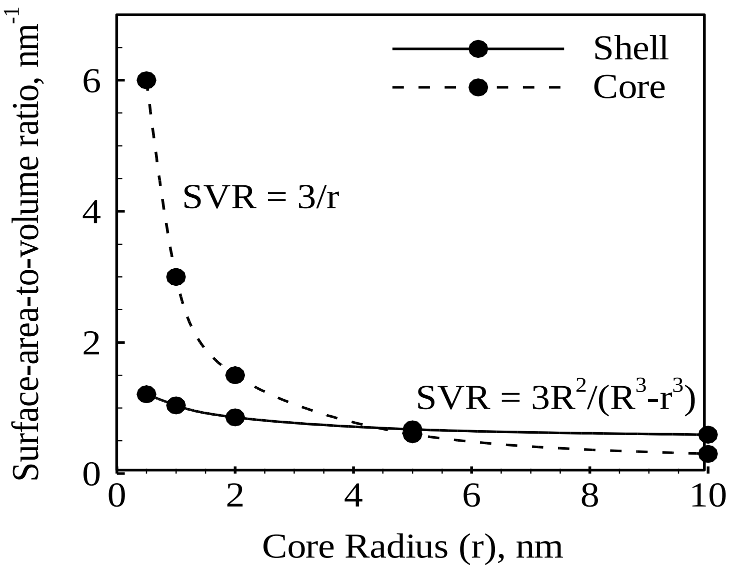

Figure 4.12: Effect of core radius on surface-area-to-volume ratio (SVR) of the core and shell for particles with a 2 nm shell.

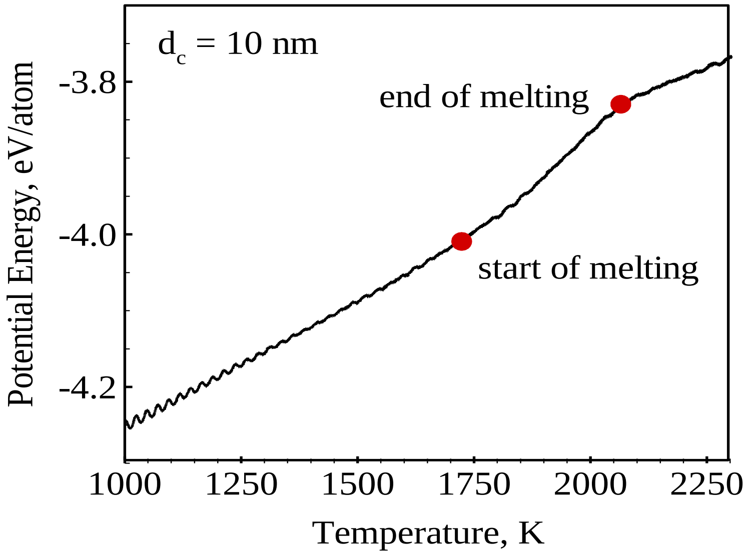

Figure 4.13: Potential energy of the core as a function of temperature for core diameter of 10 nm and shell thickness of 1 nm.

scenario differs from that observed for nickel-coated aluminum particles. The solid nickel shell exerted a cage-like effect on the aluminum core. As a result, the core was superheated above the melting point of a nascent aluminum particle. For aluminum-coated nickel particles, no such phenomenon is observed because the shell melts before the core.

It is useful to understand the effects of core size and shell thickness on diffusion processes and inter-metallic reactions. Figure 4.14a shows the variation of the core radius with temperature and/or time for particles with core diameter of 3 nm and shell thickness of 1 and 2 nm. The diffusion of nickel atoms is facilitated for thinner shells, since the melting temperature of the shell decreases with decreasing shell thickness. As a result, inter-metallic reactions begin to occur at lower temperatures for thinner shells. Figure 4.14b shows the trends for particles with core diameters in the range of 3-7 nm. The shell thickness is chosen as 2 nm. For the sake of convenience, the core radius is normalized based on its initial value. The results seem to suggest that the diffusion

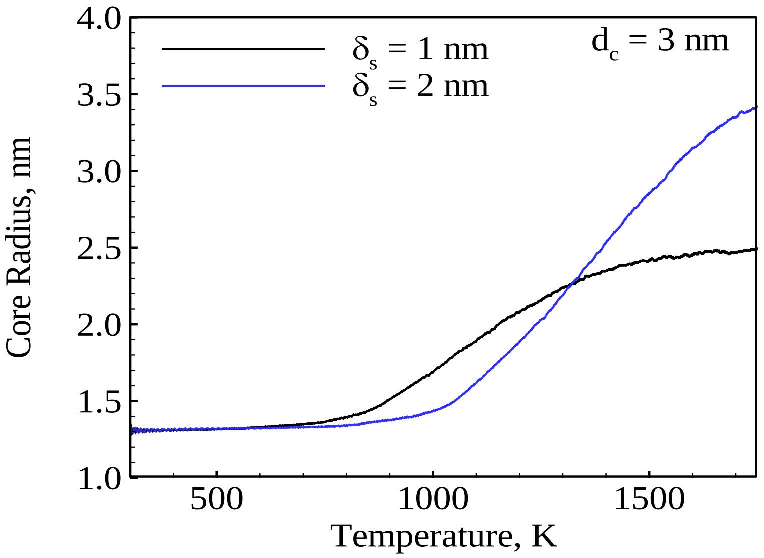

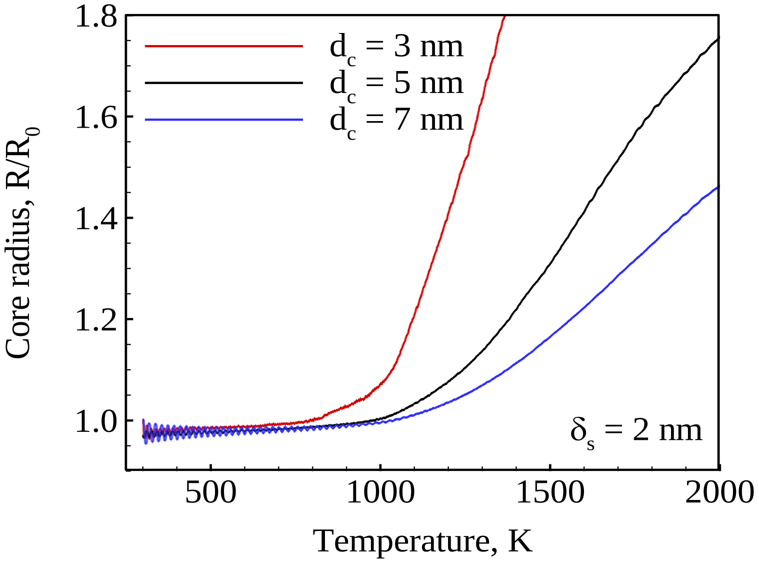

Figure 4.14: Core radius as a function of temperature (and/or time) for (a) core diameter of 3 nm and shell thickness of 1 and 2 nm; (b) shell thickness of 2 nm and core diameters of 3, 5, and 7 nm.

process is promoted for smaller core sizes. This is partly an artifact resulting from the normalization process. The core size exerts only a modest effect on the diffusion, since the melting temperature of the shell is not a strong function of the core diameter. Figure 4.15a shows the effect of shell thickness on the adiabatic reaction temperature for particles with a core diameter of 3 nm. The reaction temperature decreases from 1850 to 1350 K, when the shell thickness increases from 0.5 to 3.0 nm. This can be attributed to the presence of excess amount of unreacted aluminum atoms in the product. For a particle with core diameter of 3 nm and shell thickness of 0.5 nm, the inter-metallic reaction is given by

$$0.55\mathrm{Al} + 0.45\mathrm{Ni} \rightarrow \mathrm{Ni}_{0.45}\mathrm{Al}_{0.55}. \qquad (4.6)$$

As a result, all the atoms participate in the alloying reactions to form non-stoichiometric

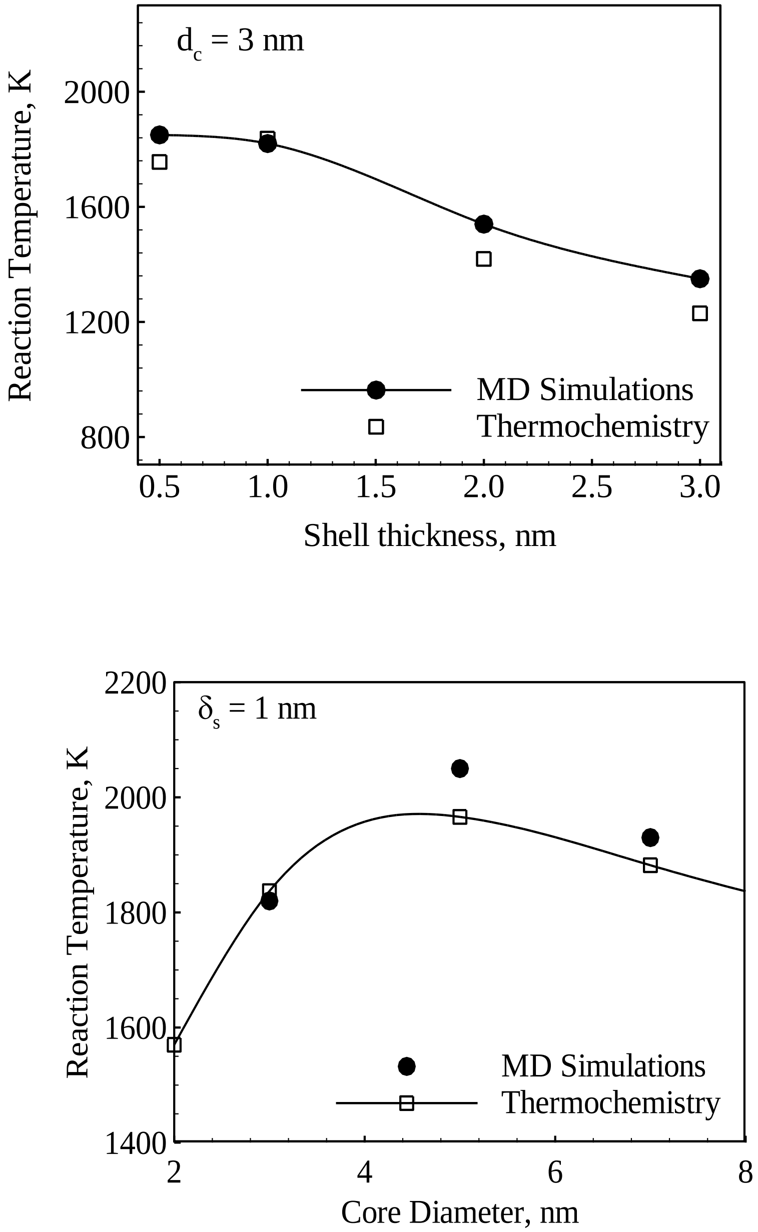

Figure 4.15: Adiabatic reaction temperature as a function of (a) shell thickness for a core diameter of 3 nm; (b) core diameter for a shell thickness of 1 nm.

NiAl species. For thicker shells, the reaction can be expressed as

$$xAl + Ni \rightarrow NiAl_3 + (x-3)Al. \qquad (4.7)$$

The product thus contains unreacted aluminum atoms and aluminum-rich $NiAl_3$. Satisfactory agreement with the results of thermodynamic analysis is obtained. Figure 4.15b shows the variation of the adiabatic reaction temperature with core diameter for a shell thickness of 1 nm. It increases with increasing core diameter, attains a maximum value of ~2050 K at 5 nm, and decreases with further increase in the core diameter. The reaction temperature of the particle is maximum, when the core diameter and shell thickness are chosen so as to favor the formation of B2-NiAl, which has the highest heat of formation on a per mol-atom basis (as shown in Table 4.3). In addition, the size of the core must be large enough to minimize the loss of energy content due to the low-temperature interfacial mixing process. These observations are consistent with the results obtained for nickel-coated aluminum particles. The diffusion coefficient is estimated for a particle with ~6380 core atoms (diameter 5 nm) and shell thickness of 0.5 nm. Figure 4.16 shows the effect of temperature and/or time on diffusion coefficient of nickel atoms in aluminum shell for an aluminum-coated nickel particle and that of aluminum atoms in nickel shell for a nickel-coated aluminum particle consisting of 6380 core atoms and 0.5

Table 4.3: Heats of formation of Ni-Al compounds at 298 K (Morsi 2001).

Compound	Heat of formation, (kJ/mol atoms)
Ni_3Al	-38.2
NiAl	-59.2
Ni_2Al_3	-56.5
$NiAl_3$	-37.6

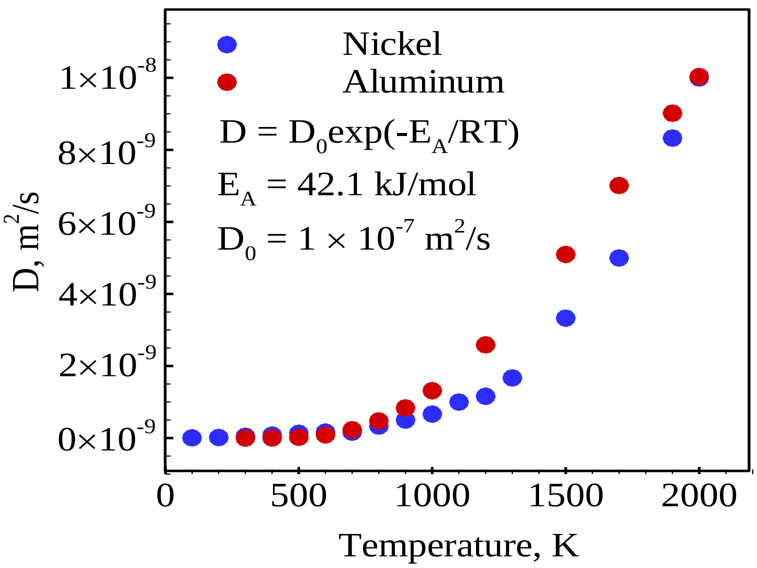

Figure 4.16: Effect of temperature (and/or time) on the diffusion coefficients of nickel atoms in aluminum shell and aluminum atoms in nickel shell for particles with 6380-atom core and 0.5 nm thick shell.

nm thick nickel shell. In both cases, the diffusion coefficient increases sharply upon melting of the aluminum component. The diffusion coefficient exhibits a temperature dependence of the form

$$D = D_0 \exp\left(-\frac{E_A}{RT}\right), \tag{4.8}$$

where E_A is the activation energy and D_0 is the pre-exponential factor. The curve-fit indicates a value of 42.1 kJ/mol for the activation energy and 1×10^{-7} m^2/s for the pre-exponential factor, which are similar to those obtained for nickel-coated aluminum particles. It is important to reemphasize that the obtained values depend significantly on the core diameter and shell thickness. The results once again demonstrate that the dimensions of the core and shell can be tailored to obtain the desired melting, diffusion, and reaction behavior in nickel-aluminum core shell structured particles.

4.3 Summary

The major results of the analysis presented in this chapter are summarized as follows:

- The Cleri-Rosato potential function combined with parameters developed by Papanicolaou et al. offers accurate prediction of the size dependence of the melting temperature of nascent aluminum and nickel particles. Favorable agreement with the experimental data is achieved. The results represent one of the most accurate melting point data in the literature for aluminum and nickel under ultra fast heating conditions.

- Molecular dynamics simulations are performed to analyze the thermo-chemical behavior of aluminum-coated nickel particles. The melting point of the nickel core is comparable to that of a nascent nickel particle. The melting scenario differs from that observed for nickel-coated aluminum particles. The solid nickel shell exerted a cage-like effect on the aluminum core. As a result, the core was superheated above the melting point of a nascent aluminum particle. For aluminum-coated nickel particles, no such phenomenon is observed because the shell melts before the core.

- Melting of the aluminum shell is a heterogeneous process beginning at the outer surface of the particle. The melting temperature of the aluminum shell increases with increasing shell thickness, from 750 K at 1 nm to 960 K at 3 nm. These are comparable to the values obtained for pure aluminum particles. It exhibits weak dependence on the core size, which is explained by the relative weak effect of the core diameter on the surface-to-volume ratio of the shell.

- Diffusion of nickel (core) atoms, which is observed upon melting of the aluminum shell, is followed by aluminum-nickel reactions that self-heat the particle. Diffusion process is facilitated for thinner shells due to lower melting temperature.

- The diffusion coefficient of nickel atoms in aluminum shell was calculated for a 6 nm particle with a 0.5 nm shell. The curve-fit indicates a value of 42.1 kJ/mol for the activation energy and 1×10^{-7} m^2/s for the pre-exponential factor, which are similar to those obtained for nickel-coated aluminum particles. These numbers are likely to vary depending on the core diameter and shell thickness.

- The adiabatic reaction temperature is strongly dependent on the core diameter and shell thickness. For a core diameter of 3 nm, the reaction temperature decreases from 1850 to 1350 K, when the shell thickness increases from 0.5 to 3.0 nm. This can be attributed to the presence of excess amounts of unreacted metal atoms in the product particle. The reaction temperature increases with increasing core diameter, attains a maximum value of ~2050 K at 5 nm, and decreases with further increase in the core diameter. It is maximum, when the core diameter and shell thickness are chosen so as to favor the formation of B2-NiAl, which has the highest heat of formation on a per mol-atom basis, and particle size is large enough to minimize the energy loss due to interfacial premixing process.

CHAPTER 5

COMBUSTION OF NANO-ALUMINUM PARTICLES AND LIQUID WATER

5.1 Theoretical Framework

The analysis considers steady, one-dimensional, and isobaric flame propagation in a chemically reacting system consisting of passivated nano-aluminum particles and liquid water. In Risha et al.'s experiments (Risha et al. 2007), highly linear position-time (*x*-*t*) curves for the flame front were obtained, which implies that the flame propagates at a constant speed through the unburned mixture. Furthermore, the volume of the vessel was chosen be large enough (~23 L) so as to minimize pressure variation caused by the generation of the gaseous combustion products. Measurements, however, indicate that there is a slight increase in the pressure in the experiments. For example, an average pressure of 7.24 ± 0.08 MPa is observed when the initial pressure is set as 7 MPa. In the present analysis, the particles are assumed to be uniformly sized at the mean value. Note that the nano-aluminum powder consists of particles with disparate sizes. For example, the actual diameters of the particles in the 38-nm powder are in the range of 30-44 nm (Risha et al. 2007). For simplicity, particle agglomeration is neglected. Flame propagation, which is modeled as a propagation of a thermal conduction wave, is accompanied by a variety of physicochemical processes, including water vaporization, chemical reactions, and mass, momentum and energy exchanges between the fluid and particle phases. The system is approximated to be pseudo-homogenous, so that the particles and surrounding fluid are in thermal equilibrium locally. Water vaporization

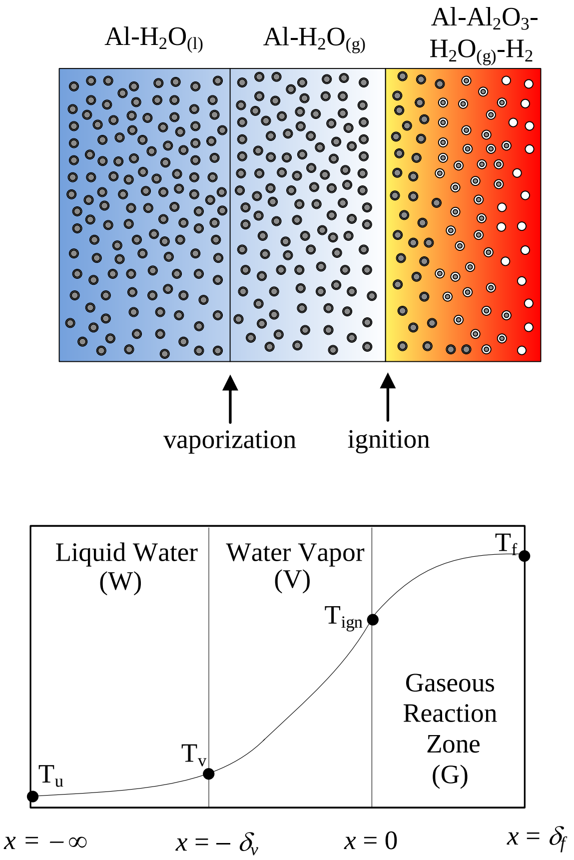

Figure 5.1: Physical model and multi-zone theoretical framework.

occurs on an infinitesimally thin plane. Figure 5.1 shows the physical model and multi-zone flame structure proposed in the present study. The entire spatial domain is divided into three zones to demarcate the regions in which phase transition and chemical reactions occur. The initial temperature of the mixture is 298 K. Water undergoes a thermodynamic phase transition at the vaporization front, $x = -\delta_v$, where the local temperature reaches the vaporization point, T_v. The particles start to burn once the ignition temperature, T_{ign}, is attained. Chemical reactions are neglected in the preheat zones. The overall thermal conductivity of the passivated aluminum particle, λ_p, is calculated as follows (Badrinarayan & Barlow 1990):

$$\lambda_p = \frac{\lambda_{Al}^2 R}{(r-R)\left[2\lambda_{Al}\ln a - 2\lambda_{ox}\ln a - \left(\lambda_{Al}^2/\lambda_{ox}\right)\right] + r\lambda_{Al}}, \tag{5.1}$$

where

$$a \equiv \frac{b-\lambda_{Al}R}{b-\lambda_{Al}(R-r)};\ b \equiv 2(R-r)\lambda_{ox} + 2r\lambda_{Al}. \tag{5.2}$$

Here r is the radius of the aluminum core and R the outer radius of the particle. The subscripts Al and ox refer to aluminum and oxide, respectively. The thermal conductivity of the mixture, λ_m, is calculated using the following correlation (Ticha, Pabst & Smith 2005):

$$\lambda_m = \lambda_p \exp\left(\frac{-B\Phi_f}{1-\Phi_f}\right), \tag{5.3}$$

where $B = 1.5$, λ the thermal conductivity and Φ the volume fraction. The subscripts m, p, and f refer to mixture, particle, and fluid, respectively. Equation (5.3) is valid when the thermal conductivity of fluid is two orders of magnitude lower than that of the particle (Ticha, Pabst & Smith 2005). This criterion is met in the present study. Maxwell model, which was first considered, under predicted the mixture thermal conductivity for higher particle loading densities. Volume averaging also gave a reasonably good prediction of the mixture thermal conductivity. The thermophysical properties of water and hydrogen are taken from NIST database (Lemmon, Huber & McLinden 2007) and Sengers & Watson 1986, while those of aluminum and its oxide are taken from Gale & Totemeier 2004, Buyco & Davis 1970, and Munro 1997. Table 5.1 summarizes the property data at a baseline pressure of 3.65 MPa. All properties are evaluated at an average temperature in each zone. The enthalpy of vaporization and boiling point of water are calculated as a function of pressure. Mass and energy balances are enforced for a differential element

Table 5.1: Thermophysical properties of different species in three zones at baseline pressure of 3.65 MPa.

Species	Thermal conductivity, W/m-K			Specific heat, kJ/kg-K			Density, kg/m^3		
	W	V	G	W	V	G	W	V	G
Al	239	95	143	0.954	1.260	1.176	2700		
Al_2O_3	22.20	9.50	6.40	0.930	1.200	1.303	4000		
$H_2O(l)$	0.70	–	–	4.400	–	–	995	–	–
$H_2O(g)$	–	0.07	0.12	–	2.330	2.580	–	8.58	5.17
H_2	–	–	0.80	–	–	16.150	–	–	0.56

T_v = 519 K, T_{ign} = 1360 K, T_f = 1800 K at p = 3.65 MPa

W: liquid water zone; V: water vapor zone; G: gaseous reaction zone

in each zone. The conservation equations are derived following well-established methodologies in the literature (Brennen 2005). They are solved to obtain the burning rate and temperature distribution. The formulation is developed based on a coordinate system attached to the propagating flame.

5.1.1 Energy Balance for the Liquid Water Zone

The liquid water zone encompasses the region between the far field, $x = -\infty$, and the vaporization front, $x = -\delta_v$. The energy equation takes the form

$$\left(\rho_{Al}C_{p,Al}\Phi_{Al}+\rho_{ox}C_{p,ox}\Phi_{ox}+\rho_{lw}C_{p,lw}\Phi_{lw}\right)r_b\frac{dT}{dx}=\lambda_{m,W}\frac{d^2T}{dx^2}, \tag{5.4}$$

subject to the boundary conditions:

$$T_{x\to-\infty} = T_u ; T_{x=-\delta_v} = T_v ; \tag{5.5}$$

where ρ is the density, C_p the specific heat, r_b the burning rate, T the temperature, x the space coordinate, and δ_v the thickness of the vapor zone. The subscripts W, u, v, ox, and lw refer to the liquid water zone, unburned state, vaporization, oxide, and liquid water, respectively. An analytical solution to Eq. (5.4) can be obtained for the temperature profile.

$$T = T_u + \left(T_v - T_u\right)\exp\left\{k_W\left(x+\delta_v\right)\right\}, \tag{5.6}$$

where k_W is the ratio of the burning rate to the thermal diffusivity, which can be defined as

$$k_W = r_b / \left(\lambda_{m,W} / \left(\rho C_p\right)_W\right), \tag{5.7}$$

where (ρC_p) denotes the volume-averaged product of the density and specific heat of the mixture. The temperature profile depends on the burning rate and thickness of the water vapor zone, both of which are not known *a priori*.

5.1.2 Energy and Mass Balance for the Water Vapor Zone

Velocity of water vapor generated at the vaporization front, $x = -\delta_v$, can be determined using the conservation of mass of water

$$\rho_{lw} r_b = \rho_{wv} v_{wv} . \tag{5.8}$$

Here, v is the gas velocity. The subscript wv denotes water vapor. Equation (5.8) can be used to express the energy equation in the following form:

$$\left(\rho_{Al} C_{p,Al} \Phi_{Al} + \rho_{ox} C_{p,ox} \Phi_{ox} + \rho_{lw} C_{p,wv} \Phi_{lw}\right) r_b \frac{dT}{dx} = \lambda_{m,V} \frac{d^2 T}{dx^2}, \tag{5.9}$$

subject to the interfacial conditions:

$$\begin{cases} x = -\delta_v : \lambda_m \left.\dfrac{dT}{dx}\right|_V = \lambda_m \left.\dfrac{dT}{dx}\right|_W + h_{fg}\Phi_{lw}\rho_{lw}r_b, \\ x = 0 : T = T_{ign}, \end{cases} \tag{5.10}$$

where h_{fg} is the enthalpy of water vaporization and T_{ign} the ignition temperature of nano-aluminum particles. The subscript V refers to the vapor zone. The vapor zone thickness can be obtained iteratively or directly using the heat-flux balance at $x = -\delta_V$:

$$\delta_v = \frac{1}{k_V}\log\left\{\left(1 + \frac{\lambda_{m,V}k_V\left(T_{ign} - T_v\right)}{\lambda_{m,W}k_W\left(T_v - T_u\right) + h_{fg}\rho_{lw}\Phi_{lw}r_b}\right)\right\}. \tag{5.11}$$

The temperatures at the interfacial boundaries are matched to provide a closed-form solution to the energy equation:

$$T = \frac{1}{1 - e^{-k_V\delta_v}}\left[T_v\left(1 - e^{k_V x}\right) - T_{ign}\left(e^{-k_V\delta_v} - e^{k_V x}\right)\right]. \tag{5.12}$$

5.1.3 Energy Balance for the Reaction Zone

The stoichiometric reaction of aluminum particles with water vapor is given by

$$2\mathrm{Al} + 3\mathrm{H_2O} \rightarrow \mathrm{Al_2O_3} + 3\mathrm{H_2}. \tag{5.13}$$

The properties are calculated by averaging their respective values of the reactant and product species. The energy equation can be expressed as

$$\left(\sum_i \rho_i C_{p,i}\Phi_i\right) r_b \frac{dT}{dx} = \lambda_{m,G}\frac{d^2T}{dx^2} + \frac{\rho_m Q_r}{\tau_b}, \tag{5.14}$$

where Q_r is the chemical energy release per unit mass of the mixture, and τ_b the burning time scale. The subscripts G, m and i refer to the reaction zone, mixture, and species i, respectively. To facilitate the analysis, the temperature and spatial coordinate are normalized as follows:

$$\theta = \frac{T}{T_u}, \quad y = \frac{x}{r_b \tau_0}, \tag{5.15}$$

where τ_0 is the reference time scale defined as the burning time at a reference temperature. The location $y = 0$ is the ignition point of particles. Substituting the normalized variables defined in Eq. (5.15) into Eq. (5.14), the non-dimensional form of the energy equation is obtained

$$\frac{d^2\theta}{dy^2} - \kappa^2 \frac{d\theta}{dy} = -\mu\kappa^2 \left(\theta_{ign} - 1\right) \frac{\tau_0}{\tau_b}. \tag{5.16}$$

Here $\kappa = r_b \cdot \sqrt{\tau_0 / \alpha_{m,G}}$ is the normalized burning rate, with α being the thermal diffusivity. The normalized heat-release, μ, is written as

$$\mu = \frac{-\alpha_{m,G} \rho_m Q_r}{\lambda_{m,G} \left(T_{ign} - T_u\right)}. \tag{5.17}$$

The energy equation gives only a partial description of the underlying physicochemical phenomena in the reaction zone. In particular, an equation for the consumption rate of the particle mass is also needed.

5.1.4 Particle Mass Consumption in the Reaction Zone

The composition of the particle changes during the course of its reaction with water vapor. The aluminum content decreases progressively and a spherical oxide particle forms after complete oxidation. To characterize the combustion of individual particles, an equation for the particle mass consumption is considered

$$r_b \frac{dM_p}{dx} = -\frac{M_{p0}}{\tau_b}, \tag{5.18}$$

where M_p is the particle mass. The subscript 0 refers to the initial state. Equation (5.18) can be re-written in terms of the particle size

$$\frac{d\left(d_p^3\right)}{dx} = -\frac{d_{p0}^3}{r_b.\tau_b}, \tag{5.19}$$

where d_p is the particle diameter. For consistency, the particle diameter is normalized as follows:

$$\eta = \frac{d_p}{d_{p0}}. \tag{5.20}$$

Substituting the normalized variable defined in Eq. (5.20) into Eq. (5.19), the non-dimensional form of the particle mass consumption equation is obtained

$$\frac{d\eta^3}{dy} = -\frac{\tau_0}{\tau_b}, \tag{5.21}$$

The following boundary conditions are specified to close the formulation:

$$\begin{cases} y = 0: \lambda_m \left.\frac{d\theta}{dy}\right|_G = \lambda_m \left.\frac{d\theta}{dy}\right|_V, \ \theta = \theta_{ign}, \ \eta = 1 \\ y = 1: \frac{d\theta}{dy} = 0, \ \eta = 0. \end{cases} \tag{5.22}$$

The mass and energy balance equations in the reaction zone are solved numerically, with the burning rate treated as the eigenvalue. A shooting technique is employed to find the solution; the Newton-Raphson iteration method is used (Press et al. 1992). Numerical integration is achieved by means of the Rosenbrock method (Press et al. 1992).

5.1.5 Heat Release

The actual heat release from particle burning is lower than its theoretical counterpart due to incomplete combustion. The combustion efficiency of nano-aluminum/water mixtures is in the range of 80-100%, depending on the pressure and particle size (Risha et al. 2008). Heat loss to the environment also occurs through thermal conduction and radiation. To incorporate these effects into the model, the normalized heat release is calculated based on the measured flame temperature. A simplified expression for the normalized heat release is obtained by integrating the energy equation, Eq. (5.16), and imposing the boundary conditions specified in Eq. (5.22)

$$\mu = \frac{\kappa^2\left(\theta_f - \theta_{ign}\right) + \left.\frac{d\theta}{dy}\right|_G}{\left(\theta_{ign} - 1\right)}, \tag{5.23}$$

where the subscript *f* denotes the flame. Diakov et al. (Diakov et al. 2007) studied the flame propagation of aluminum-water mixtures in a stainless steel chamber equipped with thermocouples at a pressure of 1 atm. The particle size is 100 nm and the oxide layer thickness is 1.84 nm. The measured flame temperature is 1800 K, which is significantly lower than the theoretical value of 2790 K for a particle size of 100 nm. The combustion

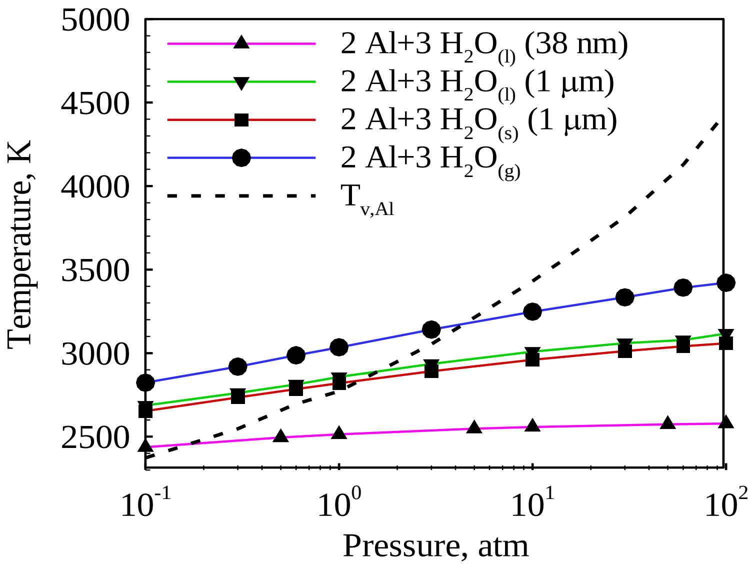

Figure 5.2: Effect of pressure on aluminum vaporization temperature and adiabatic flame temperatures for various oxidizers.

efficiency is measured to be 87%. The combustion efficiency increases with decreasing particle size (Risha et al. 2008), although the adiabatic flame temperature is lower for smaller particles (See Figure 5.2). For simplicity, a flame temperature of 1800 K is used to calculate the heat release for all particle sizes. Note that the variation of the adiabatic flame temperature with pressure is weak for nano-sized particles and is neglected. Results of the sensitivity analysis indicate that the burning rate increases modestly with increasing flame temperature. At a pressure of 3.65 MPa and particle size of 38 nm, the burning rate increases from 5.59 to 6.85 cm/s when the flame temperature increases from 1800 to 2300 K.

5.1.6 Ignition Temperature and Burning Time

The present model requires, as input parameters, the ignition temperature and burning time. Figure 5.3 shows the effect of particle size on the ignition temperature of

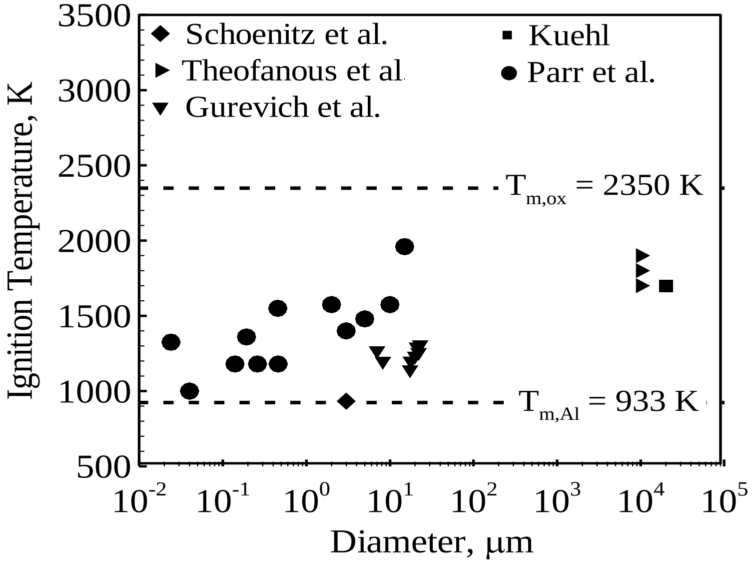

Figure 5.3: Effect of particle size on ignition temperature of aluminum particles in water vapor.

aluminum particles in water vapor environment. The ignition temperatures of micron-sized aluminum particles in water vapor are significantly lower than those in oxygenated environments. This has been attributed to the stabilization of γ-polymorph (Schoenitz, Chen & Dreizin 2009) and/or formation of weaker hydroxide layer (Kuehl 1965). In fact, Schoenitz et al. (Schoenitz, Chen & Dreizin 2009) observed that the ignition temperatures of 5-10 μm particles in water are same as those of nano-sized particles. Parr et al. (Parr et al. 2003) found that the ignition temperatures of Technanogy aluminum particles (used in the Al-water combustion experiments) in water vapor vary between 1325 and 1360 K for the particle size range of 24-192 nm. As a result, the ignition temperature is taken as 1360 K.

The combustion of aluminum particles involves mass diffusion processes and chemical reactions between the aluminum atoms and oxidizer molecules. The combustion mechanism of nano-aluminum is still an unsettled problem. It is still debated if transport (in gas or oxide layer) or chemistry is the rate-controlling process, thereby making it difficult to choose an appropriate model for the reaction rate. Furthermore, chemical kinetics and diffusion coefficients in the oxide layer are poorly known. The reference burning time scale is approximated as the burning time of Technanogy 24 nm aluminum particles at 1 atm pressure in the present study (Huang et al. 2007, Parr et al. 2003)

$$\tau_{b,24nm} = c\left[a_1 \exp\left(b_1 T\right) + a_2 \exp\left(b_2 T\right)\right]. \tag{5.24}$$

This assumption is reasonable, since the energy release rate, to a good approximation, is determined by the reactivity of individual particles. The constants are given in Table 5.2. Note that the strong temperature dependence of the burning time suggests kinetically controlled combustion mode. Bazyn et al.'s shock tube experiments (Bazyn, Krier &

Table 5.2: Constants in burning time expression.

Constant	Value
c	1.736×10^{-3}
a_1	204.650
b_1	-9.848×10^{-3}
a_2	1.842×10^{-4}
b_2	3.461×10^{-5}
a_3	7.075
b_3	-1.905×10^{-3}
a_4	4.023×10^{-1}
b_4	-3.120×10^{-4}

Glumac 2006) indicate that the burning time of nano-aluminum particles decreases with increasing gas pressure. They attribute this to the fact that the rate controlling mechanism is chemical kinetics or species diffusion through the oxide layer. In the present study, the pressure exponent in the burning time law is based on the curve-fitted burn time obtained (by Bazyn et al.) using the experimental data

$$m = a_3 \exp\left(b_3 T\right) + a_4 \exp\left(b_4 T\right). \tag{5.25}$$

The curve-fit indicates that the pressure exponent decreases from 0.8 at 1360 K to 0.37 at 2000 K. The Damkohler number analysis indicates that the chemical time scale is about two orders of magnitude greater than gas-phase diffusion time scale for a particle size of 100 nm at a pressure of 1 atm. As a result, kinetically controlled combustion is expected at nano-scales at 1 atm pressure (provided the oxide layer is breached). At higher pressures, the two time scales become comparable, so that diffusion limit is being approached again. In the intermediate pressure range, diffusion process gain importance gradually. In the diffusion regime, the burn time is nearly independent of temperature. Also, kinetics is relatively fast at higher temperatures. As a result, it is not surprising that that the pressure exponent decreases with increasing temperature. This is clearly seen in the burn time fit obtained by Bazyn et al. It is important to mention that there is significant uncertainity in the pressure exponent, since it is calculated using the burn time at only two different pressures. Strand-burning experimental data indicate that the burning rate of the aluminum-water mixture follows d_p^{-1} law over a particle size range of 50-130 nm. Our model indicates that this is possible only if the burning time follows d_p^2-law. To capture the particle size dependence of the burning time, a d_p^2-law is employed. Detailed discussions on possible rate-controlling mechanism are given in Section 5.3.

5.2 Analytical Model of the Burning Rate

An analytical expression for the burning rate can be obtained following the approach of Zeldovich, Frank-Kamenetskii, and Semenov (Glassman 1996), where the continuity of the heat flux is enforced at the ignition point. Furthemore, constancy of specific heat and thermal conductivity is assumed. The energy equation can be written as

$$\left[\rho_p(1-\Phi)+\rho_{lw}\Phi\right]C_p r_b \frac{dT}{dx} = \lambda \frac{d^2T}{dx^2}, \tag{5.26}$$

where Φ is the volume fraction of water. Equations (5.11) and (5.12) are combined to provide an expression for the heat flux at $x = 0$ in the preheat zone

$$\lambda \left.\frac{dT}{dx}\right|_V = r_b\left[2\frac{\rho_{lw}\rho_p}{\rho_{lw}+\rho_p}C_p\left(T_{ign}-T_u\right)+\frac{\rho_{lw}\rho_p}{\rho_{lw}+\rho_p}h_{fg}\right]. \tag{5.27}$$

The heat flux at x=0 in the reaction zone is calculated by taking the spatial derivative of the analytical solution to Eq. (5.14) with the high-activation energy assumption

$$\lambda \left.\frac{dT}{dx}\right|_G = \frac{\lambda Q_r}{\tau_b r_b C_p}, \tag{5.28}$$

By matching the two heat fluxes at x = 0, an analytical expression for the burning rate is obtained

$$r_b = \left(\frac{\lambda}{\rho_m C_p} \cdot \frac{2Q_r}{2C_p\left(T_{ign} - T_u\right) + h_{fg}} \cdot \frac{1}{\tau_b} \right)^{1/2}, \tag{5.29}$$

where ρ_m is the density of the unburned mixture. The obtained expression bears close resemblance to the Mallard-Le Chatelier formula for the flame speed of a homogenous gas-phase mixture obtained via one-dimensional flame propagation analysis. The parameters that significantly dictate the flame propagation are the thermal diffusivity of the mixture, heat of reaction, and burning time. The inverse dependence of the burning rate on particle size implies that species diffusion process controls the rate of combustion. The pressure exponent of 0.5 implies that species diffusion through the oxide layer or chemical kinetics is the rate controlling process. The obtained closed-form expression, Eq. (5.29), is used to estimate the burning rate of a stoichiometric nanoaluminum-water mixture. The particle size and pressure are taken to be 38 nm and 3.65 MPa, respectively. The mean specific heat of the mixture is taken as 2.36 kJ/kg-K. The thermal conductivity of the mixture is calculated to be 1.21 W/m-K. The density of the mixture is assumed to be equal to the theoretical value of 1800 kg/m^3. The enthalpies of reaction and vaporization of water are taken as 4400 and 1737 kJ/kg, respectively. The burning time is calculated as 0.07 ms. Substituting these values into Eq. (5.29), the burning rate is estimated to be 7.28 cm/s, which is in the range of 4.66-7.78 cm/s measured in the experiments (Risha et al. 2008). A more accurate result can be obtained by conducting numerical analysis. It is important to determine the sensitivity of the model predictions to changes in values of the key parameters. The obtained burning rate is sensitive to changes in the burning time used in the model. For example, the burning rate increases from 7.28 to 8.6 cm/s, when the burning time decreases from 0.07 to 0.05 cm/s. Similarly, the burning rate decreases by a factor of two, when the mixture thermal conductivity (or diffusivity) decreases by a factor of four.

5.3 Results and Discussion

The theoretical framework described in Section 5.1 is employed to calculate the temperature distribution and burning rate of stoichiometric mixtures at different pressures and particle sizes. Table 5.3 shows the characteristics of the particles considered in the present study. The thickness of the oxide layer varies in the range of 2.1-3.1 nm. The active aluminum content decreases with decreasing particle size. The particle composition significantly influences the thermophysical properties of the mixture. As a result, it is important to use an appropriate value of the oxide layer thickness in the calculations. Figure 5.4 shows the temperature distribution for a stoichiometric mixture

Table 5.3: Characteristics of aluminum particles (Risha et al. 2007).

Particle size, nm	Oxide layer thickness, nm	Al content, wt.%
38	3.10	54.3
50	2.10	68.0
80	2.70	75.0
130	2.20	84.0

containing 38 nm aluminum particles at pressures of 1 and 10 MPa. The temperature increases from an initial value of 298 K in the preheat zone and attains a maximum value of 1800 K in the reaction zone. The thickness of the vapor and reaction zones decrease with increasing pressure. The temperature distribution is further altered by the fact that

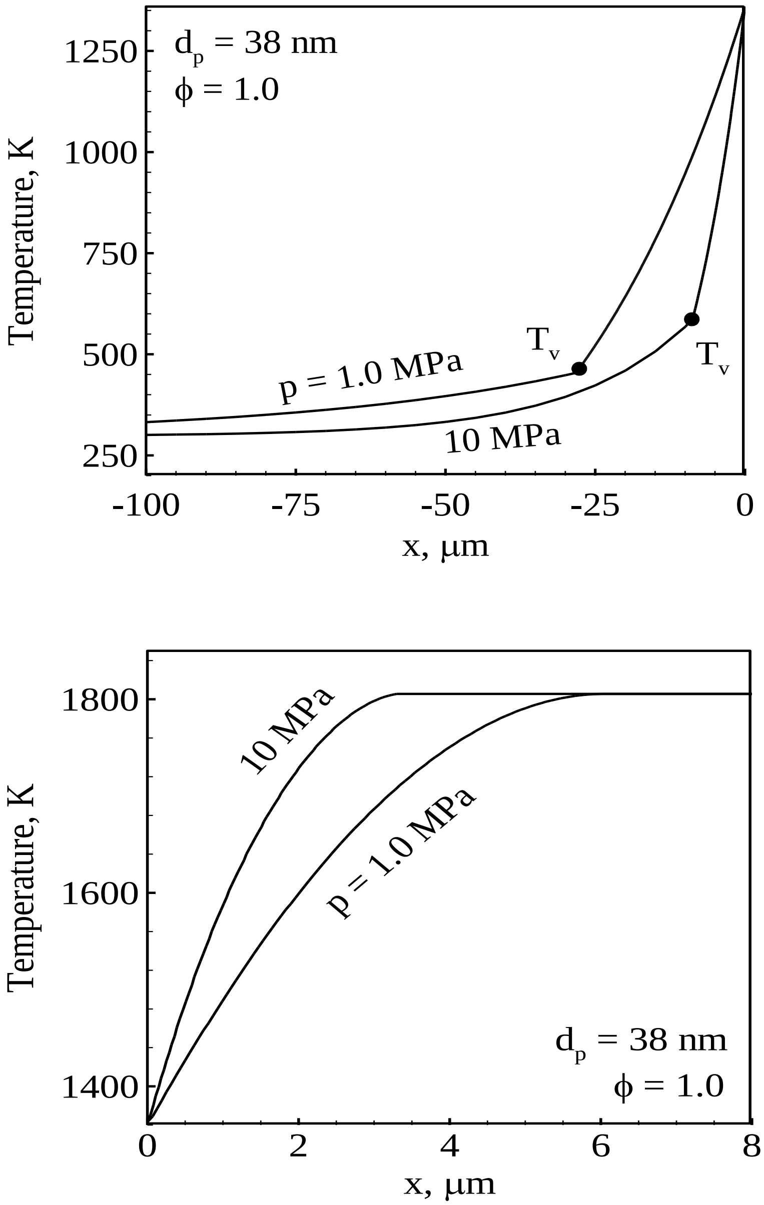

Figure 5.4: Effect of pressure on temperature distribution of stoichiometric Al-H_2O mixture containing 38 nm particles in (a) the preheat zone; (b) the reaction zone.

the vaporization temperature of water increases with pressure. An estimate of the reaction zone thickness can be obtained by multiplying the flame propagation velocity and particle burning time. Note that the heating rate in vapor and reaction zones is calculated to be on the order of 10^6 K/s at a pressure of 1 MPa. Figure 5.5 shows the effect of pressure on the burning rates for stoichiometric mixtures containing 130, 80, and 38 nm particles, respectively. For 130 nm particles, the burning rate increases from 0.76 to 1.59 cm/s when the pressure increases from 1 to 10 MPa. A similar trend is observed for the other two cases. For 38 nm particles, the presence of significant scatter in the burning rates can be attributed to the variations in the packing density of the mixture in the experiments. The actual densities are in the range of 0.75-1.00 g/cm^3, which are lower than the theoretical value of 1.80 g/cm^3. Such a disparity was not observed for 80 and 130 nm particles in the experiments, since fewer water molecules are absorbed on the particle surface (Risha et al. 2008). The burning rate decreases with increasing packing density (Risha et al. 2008). It is, thus, not surprising that some of the measured burning rates are greater than the predicted values. The pressure exponent in the burning rate law is ~0.3,

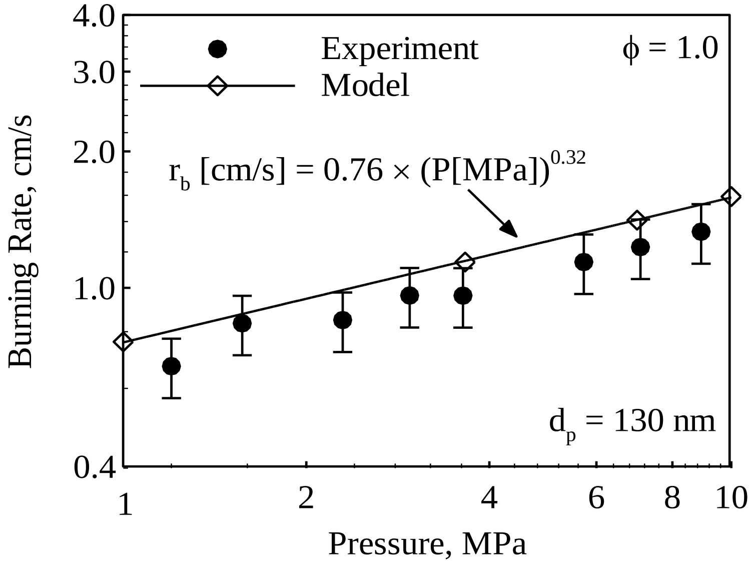

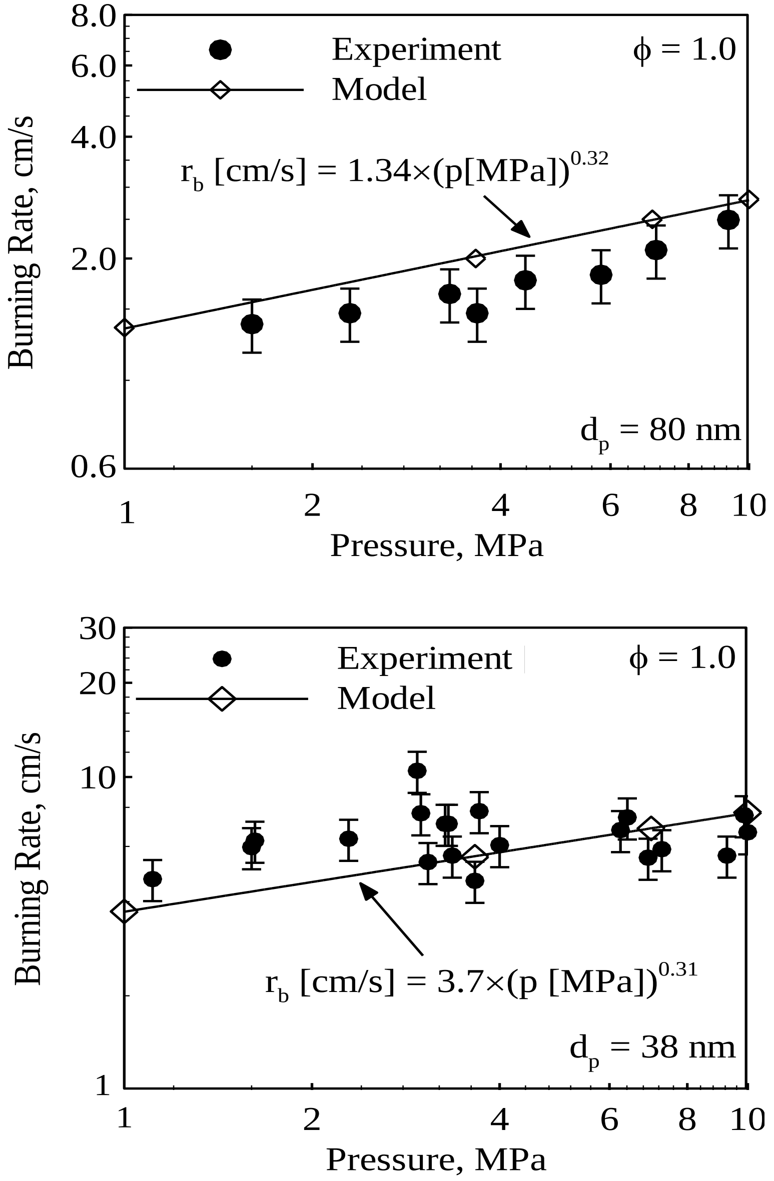

Figure 5.5: Effect of pressure on burning rates of stoichiometric Al- H_2O mixture containing 38-130 nm particles.

which agrees reasonably well with experimental data. In a typical composite solid rocket propellant, the burning rate increases with increasing pressure. A general explanation for this phenomenon is that the flame stand-off distance decreases with increasing pressure, thereby increasing the heat flow to the propellant surface (Beckstead et al. 2007). In the experiments, a visible flame appeared to be attached to the burning surface, since the particles undergo heterogeneous reactions at the particle surface. The observed pressure effect can be attributed to the fact that the particle burning time decreases with increasing pressure.

Figure 5.6 shows the effect of particle size on the burning rate for a stoichiometric mixture at a pressure of 3.65 MPa. The burning rate shows a particle size dependence of $r_b = a\ d_p^{\,n}$, with an exponent of -1.15, which agrees reasonably well with the inverse dependence observed in the experiments (Risha et al. 2008). The slightly greater diameter exponent of -1.26 is due to the variations in the thermophysical properties of the mixture with particle size. In the present analysis, the reaction time scale is assumed to follow $d_p^{\,2}$-law. The actual diameter exponent in the diffusion time scale relationship may be lower than two (Rai et al. 2006). This may explain the observed disparity between the predicted and measured values of the diameter exponent. Figure 5.7 shows a comparison of the

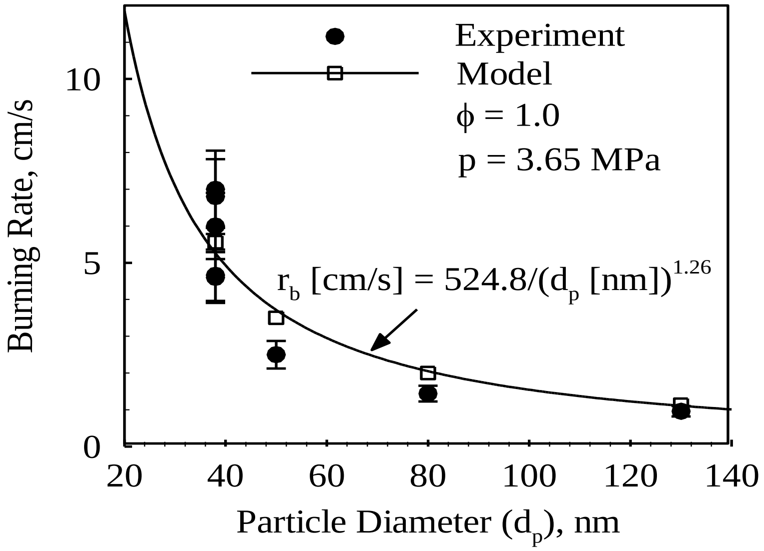

Figure 5.6: Effect of particle size on burning rate of stoichiometric Al-H_2O mixture at 3.65 MPa.

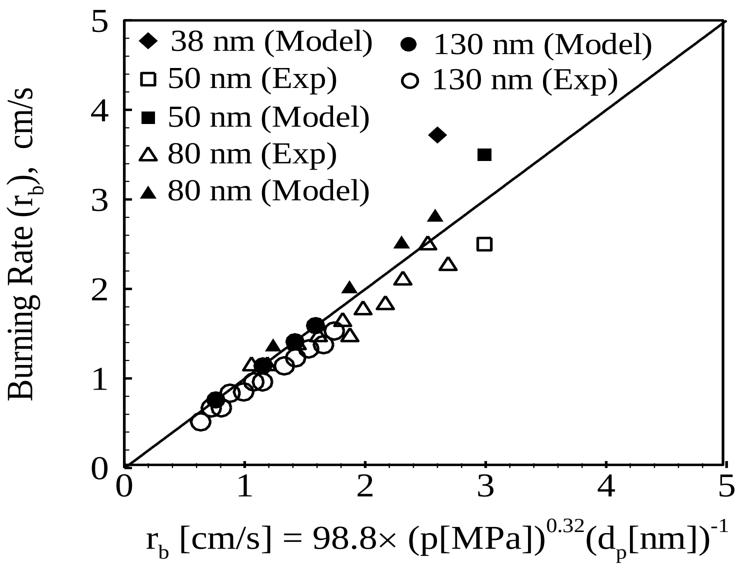

Figure 5.7: Measured and calculated burning rates vs. curve-fit values for different particle sizes and pressures, $r_b[\mathrm{cm/s}] = 98.8 \times (p[\mathrm{MPa}])^{0.32}(d_p[\mathrm{nm}])^{-1.0}$.

measured and calculated burning rates with those obtained using the following correlation:

$$r_b[\mathrm{cm/s}] = 98.8 \times (p[\mathrm{MPa}])^{0.32}(d_p[\mathrm{nm}])^{-1.0}. \tag{5.30}$$

Note that the correlation is valid only for the situations present in the current study. From time-scale arguments, the strong pressure and particle size dependencies of the burning rate suggests that species diffusion through the oxide layer may be the rate controlling process. This is consistent with the experimental data of Park et al. (Park et al. 2005) and theoretical predictions of Rai et al. (Rai et al. 2006) and Aita (Aita 2005). This, however, requires that the oxide layer be intact. This issue is highly debated and not well known at present.

It is important to note that the experiments indicate a relative weak particle size effect on the burning time of nano-aluminum particles at 1 atm pressure (diameter exponent lower than or equal to unity, Parr et al. 2003), which seem to contradict the diffusion theory. Bazyn et al. (Bazyn, Krier, & Glumac, 2007) attribute this to the transition of the combustion mode from diffusion (gas-phase) to kinetically controlled condition. This seems to be the most widely accepted theory. Buckmaster and Jackson (Buckmaster & Jackson, 2013) support this hypothesis and suggest that cracking of the oxide layer brings an additional fractal ingredient to the problem, thereby resulting in a diameter exponent slightly lower than unity. Badiola and Dreizin (Badiola & Dreizin 2012), on the other hand, speculate that the weak particle size effect is due to the transition of heat and mass transport modes from continuum to free-molecular regime and propose that combustion is limited by transport effects (gas-phase) at nano-scales. This is, however, yet to be proven. The effects of free-molecular heat and mass transfer on the burn time is ambiguous and uncertain and further analysis is needed. Note that both these theories does not consider the role of oxide layer, thereby implicitly assuming the loss of integrity of the oxide layer (by fracturing/cracking). The present study deals with pressures representative of those in practical propulsion devices (10-100 atm), for which the particle size is greater than the mean-free-path of oxidizer molecules. More importantly, chemical kinetics might be significantly faster at higher pressures. As a result, the diffusion (gas-phase) time scale may not be negligible compared to the chemical kinetics time scale. One may thus expect stronger dependence of the burning time (and burn rate) on particle size at higher pressures. Note that the pressure exponent in the burning rate law is as low as 0.27, which also indicates significant deviation from the pure kinetics limit. The exponents were calculated through a curve fit over a pressure range of 1-10 MPa, where chemical kinetics might also be important. Hence, strong pressure and particle size effects on the burning rate can be observed even if the oxide layer is breached.

Another possibility is that the particles chosen in the present study have inherently different burning time scales due to different characteristics (morphology, porosity, defects, composition, and other associated factors). For example, the experimental data of Parr et al. (Parr et al. 2003) indicate that the burning time increases by a factor of ~3, when the particle size increases from 24 to 40 nm. This corresponds approximately to d_p^2-law. But, if the burning times of 24 and 192 nm particles are compared, a d_p^1-law is obtained. Note that the burning rate fit was obtained using three data points (50, 80, and 130 nm). Further measurements of the burning rates for larger particle sizes are necessary to clearly ascertain the particle size dependence of the burning rate. Zaseck et al.'s study on aluminum-hydrogen peroxide propellant indicates that the burning rate decreases by a factor of two, when the particle size increases from 3 to 12 μm at a pressure of 7 MPa (Zaseck, Son, & Pourpoint, 2013). This is indicative of kinetically controlled combustion regime. A similar evidence is also observed for bimodal aluminum-ice mixtures, as discussed in Chapter 6. As a result, chemical kinetics might be the sole rate-controlling process, should the particle size exert a weak effect on the burning rate. This would be consistent with the pressure dependence of the burning rate.

Note that in the agglomeration of particles is not considered in the present analysis. Agglomeration prior or during combustion increases the overall size of the particle, thereby increasing the burning time scale. The severity of agglomeration depends on loading density of particles (or inter-particle distance). In the present study, the inter-particle distance decreases with increasing particle size due to changes in the consistency of the mixture with particle size. As a result, larger particles are more likely to be agglomerated. In the experiments, deionized water was employed. As a consequence, the charge buildup around the particle is expected to be minimum. The particles thus experience negligible electrostatic repulsive force and are primarily under the influence of attractive Van der Waals force. It is, thus, useful to understand the effect of particle agglomeration on the burning rate. Unfortunately, there is no basis to exactly quantify the extent of agglomeration in the present system. If the particles agglomerate such that the net diameter of the agglomerate (or aggregate) is four times the original size of the particle, the burning rate is expected to decrease by a factor of two, should the burning time be linearly dependent on particle size.

The entrainment of particles in the gas flow has also been neglected. The experiments indicate that a significant number of particles remain in the quartz tube instead of being convectively transported out of the tube, especially for larger particles (Risha et al. 2008). This may be attributed to the inertial and gravitational forces, particle-particle interactions, and quartz tube wall effects. The region in which particle motion is likely to be most important is the post-combustion zone, since the particles are under the continuous influence of the flow of the combustion gas (H_2). The entrainment phenomenon may also bring an additional pressure dependence of the burning rate, since the velocity of the particles (and flame thickness) decreases with increasing pressure. Note that the pressure exponent in burn rate law is 0.47, 0.27, and 0.31 for 38, 80 and 130 nm particles. One possible reason for the larger pressure exponent for smaller particles is that they are more likely to burn under kinetically controlled condition. The trend may also be attributed to the entrainment phenomenon, since smaller particles are likely to be more entrained in the gas. Zaseck et al.'s (Zaseck, Son, & Pourpoint, 2013) experimental data indicate that the pressure exponent in the burning rate law is as high as ~1 for smallest particles considered in their study (H-2, 3 μm). They speculate transition from diffusion to kinetically controlled conditions for aluminum-hydrogen peroxide propellant, when the particle size decreases below 20 μm. Such a high burn rate pressure exponent (greater than 0.5) can only be explained by kinetically-controlled combustion mechanism together with the entrainment effect. This phenomenon can be investigated in a future analysis through a more advanced model that accurately captures the particle motion by considering the inertial and gravitational forces, interactions and collisions between particles, and confining effect of the quartz tube. The present model captures the important features of alumimum-water combustion and is expected to serve as the basis for future studies. It is important to understand how the burning rate changes qualitatively when the particle motion is considered. In fact, a more complex model that can handle the motion of particles was first developed. The option of neglecting particle motion was later proposed (Yetter, 2008). Particle motion lowers the volume fraction of particles, thereby resulting in lower thermal conductivity and burning rate. This might be more important for 38 nm particles as opposed to 80 and 130 nm particles. For simplicity and to ensure a common basis for comparison, this phenomenon was not given due importance thereafter.

Note that the analysis considers propagation of a thermal conduction wave and does not explicitly consider radiation heat transfer. Radiation from the particles in the reaction zone may escape into the surroundings, thereby constituting heat losses and reducing the flame temperature. The effect of such heat losses were indirectly accounted by employing the actual flame temperature in the analysis. In addition, thermal radiation can preheat the unburned, thereby assisting flame propagation. This phenomenon is discussed briefly in Appendix B. Further analysis of this subject is recommended. The primary emphasis of the present work is placed on understanding the combustion mechanism of nano-aluminum/water mixtures and physicochemical parameters that affect the flame propagation under a thermal conduction wave model. It is important that the uncertainties in the burning time of nano-aluminum particles be first resolved before radiation preheating phenomenon is studied.

5.4 Implications on Combustion Mechanism of Nano-Aluminum Particles

The analysis sheds some important light on the combustion mechanism of nano-aluminum particles. Park et al.'s experiments indicate that oxidation of nano-aluminum particles is controlled by species diffusion through the oxide layer and not by chemical kinetics (Park et al. 2005). The experiments were limited to temperatures up to 1373 K and heating rates were on the order of 10^3 K/s. It is important to note that only about 40 % of the particle was oxidized over a time period of 15 seconds. The oxidation reactions took place slowly and gradually (there is no ignition point separating slow and fast reaction regimes), which may be due to the fact that the particles were heated at relatively low heating rates and/or subjected to low temperatures. The chemical kinetics time is about two orders of magnitude greater than the gas-phase diffusion time at a particle size of 100 nm and a pressure of 1 atm. Note, however, the diffusivity in solids is more than four orders of magnitude lower than that in gases. In Park et al.'s experiment, the diffusivity was estimated to be on the order of 10^{-8} cm^2/s (gas diffusivity is on the order of 1 cm^2/s). If the oxide layer is intact, species diffusion process through the oxide layer is, thus, the rate-limiting process. It is likely that the oxide layer is not breached in Park et al.'s experiments.

In burner (Parr et al. 2003) and shock tube (Bazyn, Krier & Glumac 2006) experiments, an ignition event clearly separated the slow and fast reaction regimes. The high heating rates (> 10^6 K/s), which are representative of conditions in most practical applications, may cause the oxide layer to fracture. Molten aluminum would then seep through the cracks and reach the particle surface, where it burns under kinetically controlled conditions. This is consistent with the strong temperature and pressure dependencies of the burning time (Bazyn, Krier & Glumac 2006). At higher pressures, the diffusion time scale gains significance and diffusion limit (gas-phase) is again approached. As a result, the burning time is expected to gain particle size dependence and lose pressure and temperature dependencies at higher pressures. Henz et al. (Henz, Hawa & Zachariah 2010) conducted MD simulations of ultrafast heating of aluminum particles. The particles were heated at a rate of 10^{12} K/s. The oxide layer was intact even at high heating rates and the oxidation was characterized by species diffusion processes across the oxide layer. The calculated species diffusion coefficient in the oxide layer was on the order of 10^{-4} cm^2/s, which is four orders of magnitude greater than the Park et al.'s estimated value. Note that defects in real materials may lower the tensile strength and facilitate fracturing of the oxide layer. Further experimental evidence is needed to clarify this argument. The weak dependence of the burning time on particle size is indicative of the kinetically controlled combustion regime at 1 atm pressure. This would then imply that the integrity of the oxide layer is lost.

5.5 Summary

The major results of the analysis presented in this chapter are summarized as follows:

- A multi-zone theoretical framework is established to analyze the combustion of nano-aluminum particles in liquid water. The analysis considers conservation equations in each zone and enforces mass and energy continuities at the interfacial boundaries. The model requires input of ignition temperature and particle burning times. The predictions are compared with the experimental data. Favorable agreement is obtained, thereby indicating that the model properly accounts for the relevant physicochemical phenomena.

- The burning rate shows pressure and particle size dependencies of the form $r_b[\mathrm{cm/s}] = 98.8 \times (p[\mathrm{MPa}])^{0.32} (d_p[\mathrm{nm}])^{-1.0}$.

- A closed-form (analytical) expression for the burning rate is derived to ascertain the key physicochemical parameters that affect the burning rate of the mixture. These include thermal diffusivity of the mixture, heat of reaction, ignition temperature, and burning time of particles. The expression also provides insight on the possible rate controlling mechanism. Preliminary analysis suggests that species diffusion through the oxide layer may be the rate controlling process. This would, however, require that the integrity of the oxide layer be maintained.

- The overall analysis suggests that the d_p^{-1} law for the burning rate corresponds to diffusion controlled combustion. The observed strong particle size effect on the burning rate is contrary to the weak particle size dependence of particle reactivity at nano-scales observed at low pressures. In the literature, the latter trend is commonly attributed to the transition of combustion mode from diffusion to kinetically controlled conditions. Several explanations are proposed to resolve the apparent contradiction:

  - Firstly, the burning rate curve fit was obtained using three data points and there could be large uncertainty in the fit. The particles chosen in the present study may have inherently different burning time scales due to different characteristics (morphology, porosity, defects, composition, and other associated factors). Further measurements are necessary to ascertain the actual size dependence of the burning rate.

  - Secondly, in the pressure range of interest, the gas-phase diffusion time scale may gain significance relative to the kinetics time scale. As a result, the burning time may exhibit a stronger dependence on the particle size. The present model indicates that the strong pressure and particle size dependence may be due to the fact that both diffusion and chemical kinetics are important for conditions encountered in the present study.

- The present study indicates that the pressure dependence of the burning rate is a result of the pressure dependence of the burning time. If particle entrainment in the gas is significant, it is likely to induce an additional pressure dependence of the burning rate. This may also partly explain the differences in the burning rate pressure exponents of 38, 80, and 130 nm particles and anomalously high pressure exponent of ~1 in Zaseck et al.'s experiments on aluminum-hydrogen peroxide propellants. It is likely that the observed burning rate pressure dependence is caused by the pressure effect on the burning time and particle entrainment phenomenon.

CHAPTER 6

COMBUSTION OF BIMODAL NANO/MICRO ALUMINUM PARTICLES AND ICE (ALICE) MIXTURES

One of the main drawbacks of nano-aluminum/water mixture, the aging process caused by low-temperature reactions and evaporation of water, may be overcome by freezing the water in the mixture. This prompted the consideration of nano-aluminum and ice (ALICE) mixtures. ALICE is also a viable candidate solid propellant for space propulsion in low earth orbit (LEO) and even as in-situ propellants for lunar and Mars missions (Risha et al. 2013). A major drawback of ALICE mixture is the low active aluminum content of the particles. A simple approach to minimize the initial mass of aluminum oxide in the mixture is to replace a portion of nano-aluminum particles with micron-sized counterparts. The active aluminum content of micron-sized particles is nearly 100 %. This is expected to be beneficial for hydrogen generation applications. It is, however, important to know the effect of substitution on the burning rate of the mixture. In the present work, the combustion of ALICE mixtures with both mono-modal and bimodal particle size distributions is studied.

6.1 Theoretical Framework

The present work closely follows the theoretical framework described in Chapter 5. Figure 6.1 shows the physical model of concern and the multi-zone flame structure. The entire region is divided into four different zones based on the thermodynamic states

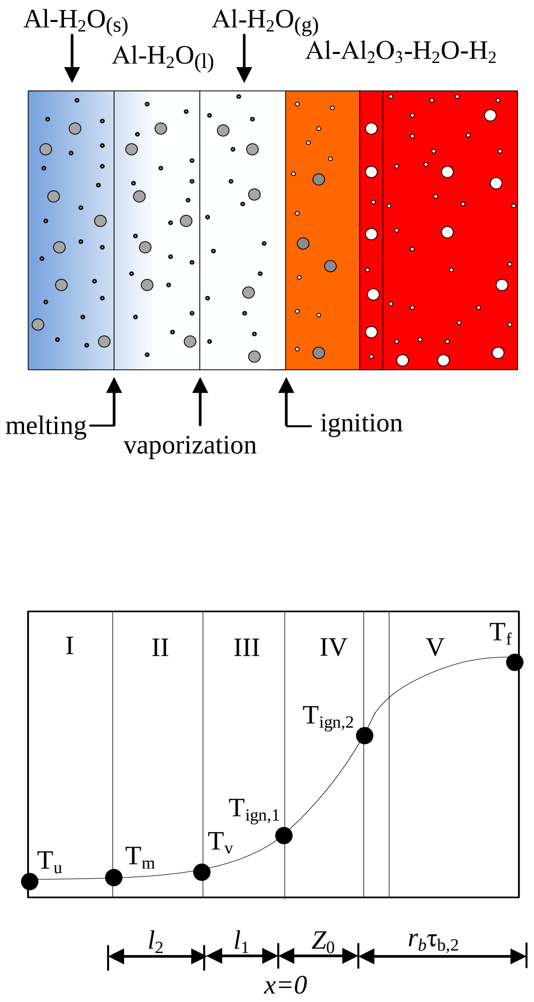

Figure 6.1: Physical model and multi-zone flame structure (◎ nano-Al, ○ Al_2O_3, ● micro-Al).

of water and Al-particle reactions. Water is initially at its solid state, and then melts and evaporates when the local temperature reaches its phase transition values, T_m and T_v, respectively. A bimodal distribution of particle sizes at nano- and micron scales is considered here; each group starts to burn at its corresponding ignition temperature, $T_{ign,1}$ or $T_{ign,2}$. No chemical reactions are assumed to occur in the preheat zones. Thermal energy is transferred to the unburned mixture by conduction.

6.1.1 Energy Balance for Aluminum-Ice Zone

The energy conservation in this region takes the form

$$\left(\rho_{Al}C_{p,Al}\Phi_{Al}+\rho_{ox}C_{p,ox}\Phi_{ox}+\rho_{I}C_{p,I}\Phi_{I}\right)r_{b}dT/dx=\lambda_{m,1}d^{2}T/dx^{2}, \tag{6.1}$$

subject to the interfacial conditions:

$$T_{x\to-\infty}=T_{u}; \qquad T_{x\to-(l_1+l_2)}=T_{m}; \tag{6.2}$$

where ρ is the density, C_p the specific heat, r_b the burning rate, T the temperature, l_1 and l_2 the thickness of the vapor and water zones, respectively, and x the space coordinate. The subscripts u and I refer to the unburned state, and ice, respectively. An analytical solution is obtained for the temperature profile:

$$T=T_{u}+\left(T_{m}-T_{u}\right)\exp\left\{k_{1}\left(x+l_{1}+l_{2}\right)\right\}, \tag{6.3}$$

where k_1 is the ratio of the burning rate to the thermal diffusivity of the ALICE mixture, defined as:

$$k_{1}=r_{b}\left(\rho C_{p}\right)_{1}/\lambda_{m,1}, \tag{6.4}$$

where $(\rho C_p)_1$ denotes the volume-averaged product of density and specific heat for the mixture. The temperature varies exponentially with the spatial coordinate, x.

6.1.2 Energy Balance for Aluminum-Water Zone

The mass conservation of water is used to derive the following energy equation:

$$\left(\rho_{Al}C_{p,Al}\Phi_{Al}+\rho_{ox}C_{p,ox}\Phi_{ox}+\rho_{I}C_{p,w}\Phi_{I}\right)r_{b}dT/dx=\lambda_{m,2}d^{2}T/dx^{2}, \tag{6.5}$$

subject to the interfacial conditions:

$$\begin{cases} x=-l_{1}:\ T=T_{v}, \\ x=-l_{1}-l_{2}:\ \lambda_{m,2}dT/dx=\lambda_{m,1}dT/dx+h_{sl}\Phi_{I}\rho_{I}r_{b}, \end{cases} \tag{6.6}$$

where h_{sl} is the enthalpy of melting of ice. The subscripts v and w refer to vaporization and water, respectively. The thickness of the liquid zone is calculated by performing the heat-flux balance at the melting front, $x = -(l_1+l_2)$:

$$l_2 = \frac{1}{k_2}\log\left(1+\frac{\lambda_{m,2}k_2\left(T_v-T_m\right)}{\lambda_{m,1}k_1\left(T_m-T_u\right)+h_{sl}\rho_I\Phi_I r_b}\right). \tag{6.7}$$

An analytical solution to Eq. (6.5) is derived by matching the temperature at the interfacial boundaries:

$$T = \frac{T_v\left(e^{k_2\left(x+l_1\right)}-e^{-k_2 l_2}\right)+T_m\left(1-e^{k_2\left(x+l_1\right)}\right)}{1-e^{-k_2 l_2}}. \tag{6.8}$$

6.1.3 Energy and Mass Balance for Aluminum-Water Vapor Zone

The vaporization of water causes water vapor to emerge at a higher velocity at the vaporization front, $x = -l_1$. Its velocity is calculated by considering the mass conservation of water:

$$\rho_I r_b = \rho_v v_g, \tag{6.9}$$

where v_g is the gas velocity and ρ_v the density of water vapor. The energy conservation equation is derived as follows:

$$\left(\rho_{Al}C_{p,Al}\Phi_{Al}+\rho_{ox}C_{p,ox}\Phi_{ox}+\rho_I C_{p,v}\Phi_I\right)r_b dT/dx = \lambda_{m,3}d^2T/dx^2, \tag{6.10}$$

subject to the interfacial conditions

$$\begin{cases} x=-l_1 : \lambda_{m,3}dT/dx = \lambda_{m,2}dT/dx + h_{fg}\Phi_I\rho_I r_b, \\ x=0 : T = T_{ign,1}, \end{cases} \tag{6.11}$$

where h_{fg} is the enthalpy of water vaporization and $T_{ign,1}$ the ignition temperature of nano-Al particles. The vapor zone thickness is obtained by balancing the heat-flux at $x = -l_1$:

$$l_1 = \frac{1}{k_3}\log\left(1+\frac{\lambda_{m,3}k_3\left(T_{ign,1}-T_v\right)}{\frac{\lambda_{m,2}k_2\left(T_v-T_m\right)}{\left(1-e^{-k_2l_2}\right)}+h_{fg}\rho_I\Phi_I r_b}\right). \tag{6.12}$$

The temperatures at the interfacial boundaries are matched to provide a closed-form solution to the energy equation:

$$T = \frac{\left[T_v\left(1-e^{k_3x}\right)-T_{ign,1}\left(e^{-k_3l_1}-e^{k_3x}\right)\right]}{1-e^{-k_3l_1}}. \tag{6.13}$$

The temperature profiles in the water and vapor zones depend on their respective thicknesses, which are not known *a priori* and must be solved for simultaneously with the burning rate and thickness.

6.1.4 Energy Balance for Reaction Zone

The water vapor reacts with Al particles to form aluminum oxide and hydrogen:

$$2\mathrm{Al}+3\mathrm{H_2O}\rightarrow \mathrm{Al_2O_3}+3\mathrm{H_2}. \tag{6.14}$$

The mixture properties are obtained by averaging their respective quantities of the reactant and product species. The reaction zone is divided into three regions: (1) nano-Al reaction region in which nano-Al particles ignite and burn (2) over-lapping reaction zone in which both nano- and micron-sized Al particles burn; and (3) micro-Al reaction zone in which only micron-sized particles continue to burn. The energy conservation can be written in the following general form:

$$\left(\sum_i \rho_i C_{p,i}\Phi_i\right) r_b dT/dx = \lambda_{m,4}d^2T/dx^2+\sum_{j=1}^{2}\eta_j\rho_{u,m}Q/\tau_{b,j}, \tag{6.15}$$

where $\rho_{u,m}$ is the unburned mixture density, η the fraction of nano/micron-sized particles, and τ_b the burning time. The subscripts i, j refer to species i and particle class j, respectively. The heat of reaction, Q, is calculated as:

$$Q - Q_v - Q_m = C_p\left(T_f - T_u\right), \tag{6.16}$$

where T_f, is the actual flame temperature, Q_v and Q_m are the enthalpies of water vaporization and ice melting per unit mass of the mixture, respectively. The actual flame temperature was chosen based on the experimental data (Diakov et al. 2007). Chemical equilibrium calculations were performed to adjust the flame temperature for the case of bimodal particle size distributions. To facilitate the analysis, the temperature and the spatial coordinate are normalized as follows:

$$\theta = T/T_u, \quad y = x/\left(r_b\tau_0\right), \tag{6.17}$$

where, τ_0 is the burning time at a reference temperature. The location $y = 0$ is the ignition point of nano particles. Substituting the normalized variables defined in Eq. (6.17), Eq. (6.15) is written as

$$d^2\theta/dy^2 - \kappa^2 d\theta/dy = -\sum_{j=1}^{2}\mu_j\kappa^2\left(\theta_{ign,j} - 1\right), \tag{6.18}$$

where $\kappa = r_b\sqrt{\tau_0/\alpha_{m,4}}$ is the normalized burning rate, with α being the thermal diffusivity. The normalized heat-release rate, μ_j, is written as

$$\mu_j = -\alpha_{m,4}\rho_{u,m}Q\eta_j/\left[\lambda_{m,4}P_j\left(T_{ign,j} - T_u\right)\right]. \tag{6.19}$$

Here, P_1 is set to unity, and P_2 is the particle burning-time ratio, $\tau_{b,2}/\tau_{b,1}$. Equation (6.18) is solved to give the temperature profile in the reaction zone:

$$\theta = \sum_{j=1}^{2}\mu_j\left(\theta_{ign,j} - 1\right)y + C_1 e^{\kappa^2 y} + C_2. \tag{6.20}$$

The normalized heat-release rates, μ_1 and μ_2, are set to zero in the micro- and nano-Al reaction zones, respectively. The burning rate is determined iteratively by matching the temperature distribution and heat flux at the interfacial boundaries. As discussed in Chapter 5, the present model requires input of the ignition temperature and burning time of aluminum particles. Schoenitz et al. (Schoenitz, Chen & Dreizin 2009) observed that the ignition temperatures of 5-10 μm aluminum particles are same as those of nano-sized aluminum particles in water. A similar trend was observed by Parr et al. (Parr et al. 2003) and Gurevich et al. (Gurevich, Lapkina & Ozerov 1970). The lower ignition temperature of micron-sized aluminum particles in water is attributed to the stabilization of γ-polymorph (Schoenitz, Chen & Dreizin 2009) and/or formation of the weaker hydroxide layer (Kuehl 1965). As a result, a single ignition temperature of 1360 K is assigned to both nano- and micron-sized (5 μm and 20 μm) aluminum particles. The burning time of micron-sized aluminum particles is readily available and is taken from the literature (Huang et al. 2009, Bazyn, Krier & Glumac 2007).

6.2 Results and Discussion

The theoretical framework is first employed to study the flame propagation of stoichiometric ALICE mixtures with mono-modal particle size distribution over a broad range of pressures. Figure 6.2 shows the temperature distribution for an ALICE mixture containing 80 nm particles at a pressure of 1 MPa. The active aluminum content is 75 % and the oxide layer thickness is 2.7 nm. The predicted temperature distribution bears close resemblance to that of nano-aluminum/water mixtures. The thickness of the reaction zone is ~ 7 μm. The vapor zone is approximately 50 μm thick. Note that in the present analysis the pressure dependence of flame temperature is considered. Chemical equilibrium calculations indicate that the flame temperature increases slightly with

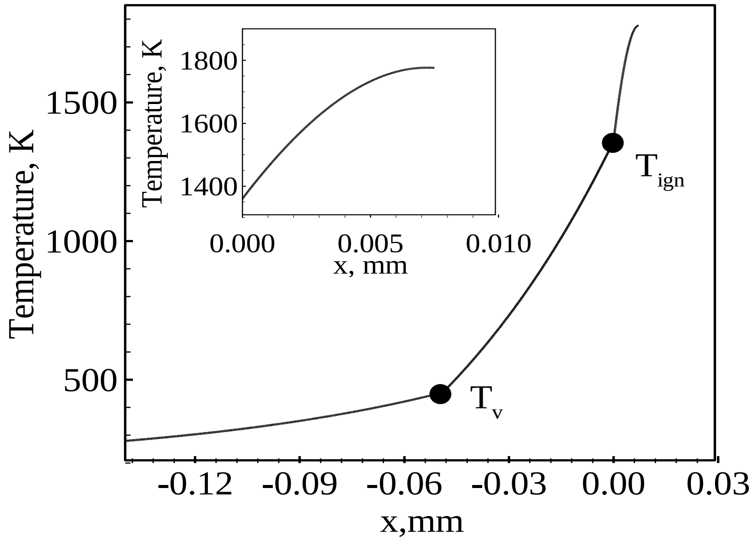

Figure 6.2: Temperature distribution for stoichiometric 80 nm ALICE mixtures at a pressure of 1 MPa.

increasing pressure. One major factor contributing to this phenomenon is the lesser energy expended for phase transitions of water at higher pressures. Figure 6.3 shows the variation of the burning rate of ALICE mixture with pressure. It increases from 1.2 to 2.5 cm/s, when the pressure increases from 1 to 10 MPa. The predicted burning-rate pressure exponent of 0.33 agrees reasonably well with the experimental data. For 80 nm aluminum/water mixture, the burning rate increases with increasing pressure, from 1.34 cm/s at 1 MPa to 2.8 cm/s at 10 MPa. As a result, it can be concluded that the aluminum-water and aluminum-ice mixtures exhibit similar burning properties. The primary distinction lies in the flame structure due to the presence of an additional preheat zone and associated enthalpy of melting of ice. The effect of the addition of micron-sized particles to the baseline nanoaluminum/ice (ALICE) mixture is studied for loading densities of micron-sized particles in the range of 0-80 %. Figure 6.4 shows the

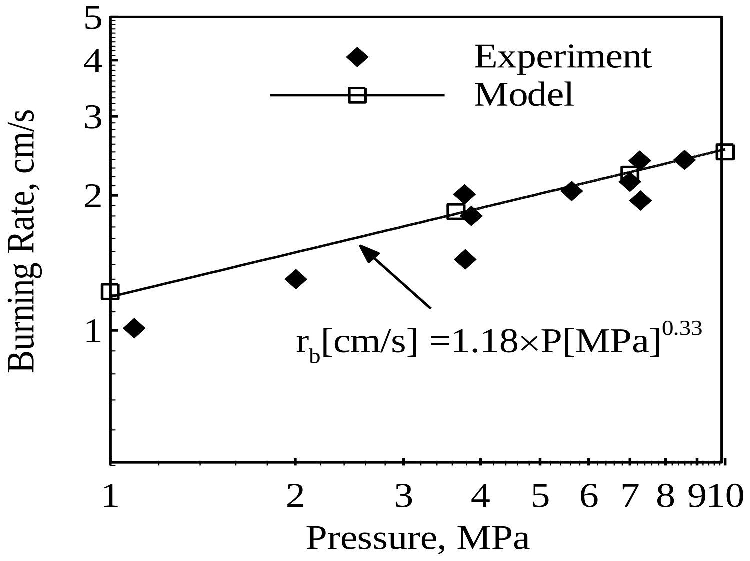

Figure 6.3: Effect of pressure on burning rates of stoichiometric 80 nm ALICE mixtures.

temperature profiles of ALICE mixtures with 80 nm and 5 μm particles at a pressure of 1 MPa for two different loading densities of 15 and 75 %. The active aluminum content of the 5 μm particle is assumed to be 100 %. The bimodal ALICE mixtures have a different flame structure, which is characterized by two overlapping particle burning regimes

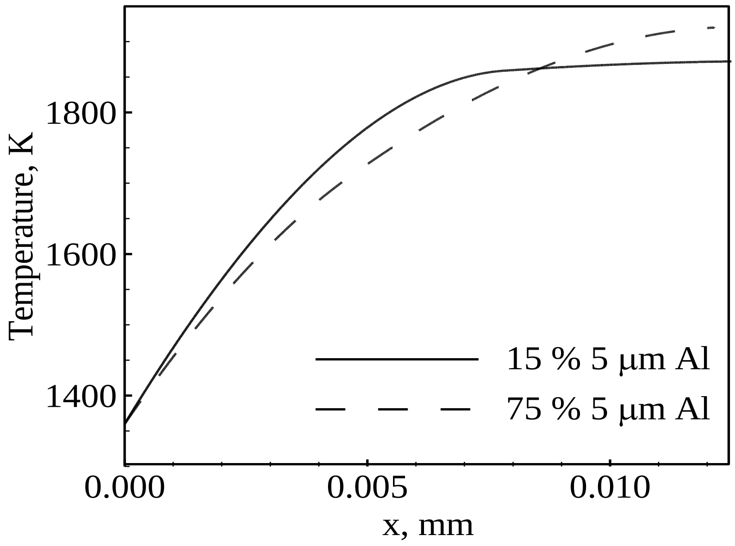

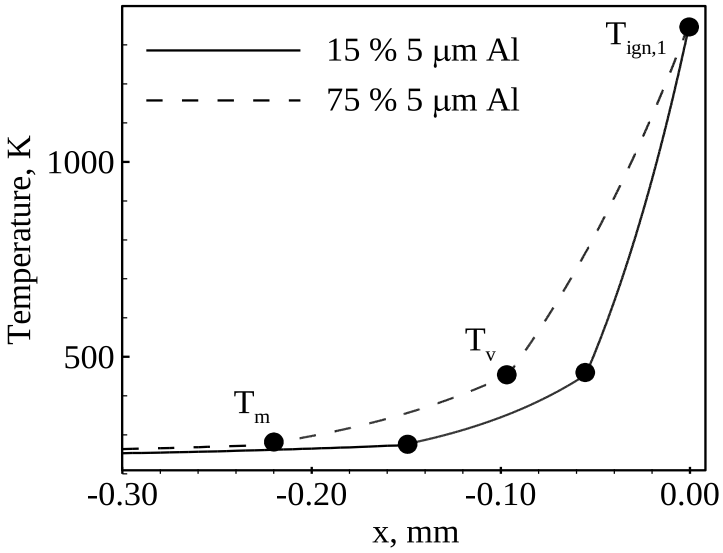

Figure 6.4: Effect of addition of 5μm Al particles on the flame structures of 80 nm ALICE mixtures in the reaction (top) and preheat (bottom) zones; P = 1 MPa.

corresponding to nano- and micron-sized particles. When the loading density is 15 % (80 nm/5 μm: 85/15 by mass), the majority of the heat release stems from the combustion of nano-Al particles. At a higher loading density, both nano- and micron-sized particles contribute significantly to the overall heat release. Note that the addition of 5 μm aluminum particles to the mixture results in higher flame temperature due to increase in the overall active aluminum content of the particle blend. It also results in thicker liquid and vapor zones due to decrease in the burning rate. Figure 6.5 shows the effect of addition of 5 μm Al particles on the burning rates of ALICE mixtures containing 80 nm particles at a pressure of 7 MPa. In spite of the longer burning time of 5 μm Al particles, the burning rate does not significantly change for loading densities less than 15 %. The addition of 5 μm Al particles increases the flame temperature, while decreasing the overall heat-release rate. These two effects counteract each other for loading densities

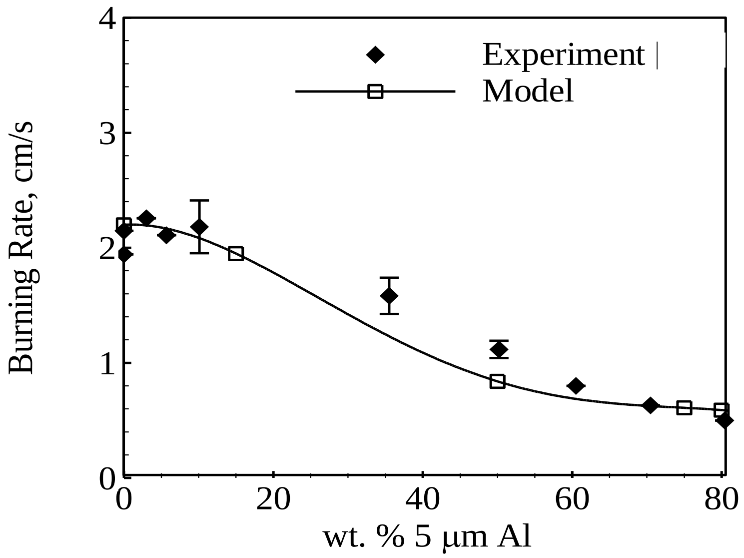

Figure 6.5: Effect of addition of 5μm Al particles on the burning rates of stoichiometric 80 nm ALICE mixtures at a P = 7 MPa.

less than 15 %. The burning rate, however, decreases to an asymptotic value of 0.6 cm/s when the loading density reaches 80 %. Reasonably good agreement with the experimental data (Connell et al. 2012) is achieved. Figure 6.6 shows the effect of pressure on the burning rates of ALICE mixtures for mono-modal distribution of 80 nm particles and bimodal distribution of 80 nm/20 μm particles. Note that the burning rate is not significantly affected when a portion of costlier nano-sized aluminum particles is replaced with cheaper 20 μm particles within the range of the loading density considered here (< 25 %). The bimodal particle size distribution can, thus, be employed to slightly increase the hydrogen yield and reduce the overall cost without significantly altering the burning rate. It is imperative to compare the burning times of 5 μm and 80 nm particles used in this study. At a pressure of 7 MPa, they are 0.21 and 2.78 ms for 80 nm and 5 μm particles, respectively. This corresponds to burn time diameter exponent slightly lower

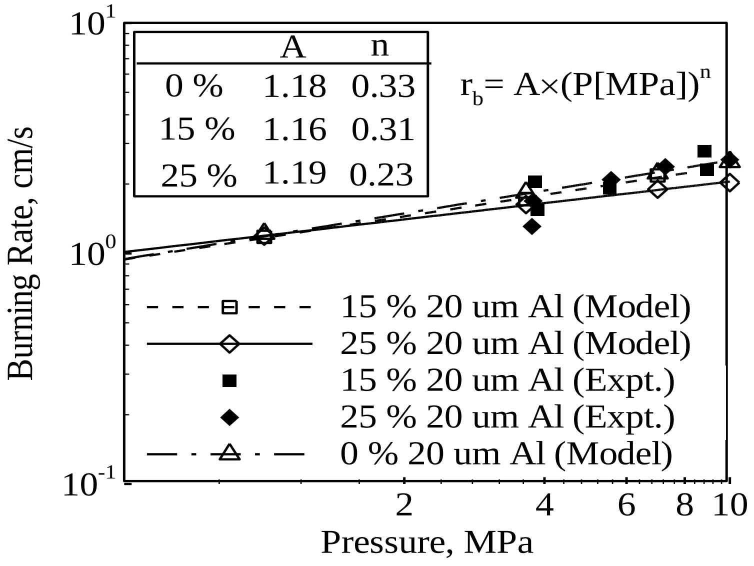

Figure 6.6: Effect of pressure on the burning rates of stoichiometric ALICE mixtures with mono-modal and bimodal size distribution of particles 80 nm/20μm.

than unity, which is consistent with the experimental data. If a d_p^2-law is used to calculate the burning time of 5 μm particles based on the reference time scale adopted in the study, the resulting burning rate is orders of magnitude lower and contradicts the experimental data. Note that the burning rate decreases from ~2 cm/s to ~ 0.5 cm/s, when the loading density of 5 μm particles increases from 0 to 80 %. This implies a weak particle size effect on the burning rate. Recent studies (Zaseck, Son & Pourpoint 2013) indicate a similar trend for micron-sized aluminum particles and hydrogen peroxide mixtures. It would then seem relevant to measure the burning rate of ALICE mixtures for a loading density of 100 %. It was, however, reported that micron-sized particles were difficult to ignite due to their higher particle heating times. As a result, water may boil out before particle ignition occurs. This may be due to the ignition system employed and further investigations are necessary (Risha et al. 2007). The theoretical analysis suggests that the burning rate is not significantly affected when the loading density increases beyond 80 %, thereby suggesting a weak particle size effect on the burning rate, representing kinetically controlled combustion regime.

6.3 Summary

The major results of the analysis presented in this chapter are summarized as follows:

- A theoretical framework is developed to study the flame propagation of aluminum-ice mixtures with both mono-modal and bimodal particle size distributions. The predicted burning rates agree reasonably well with the experimental data, thereby confirming the validity of the proposed model.

- The burning rates of aluminum-ice mixtures are similar to those of aluminum water mixtures. The primary distinction lies in the flame structure due to the presence of an additional preheat zone and associated enthalpy of melting of ice.

- The results indicate that a portion of nano-sized aluminum particles can be replaced with micron-sized particles to slightly increase the hydrogen yield and reduce the overall cost without significantly affecting the burning rate. For 5 μm particles, negligible change in the burning rate was observed for loading densities up to 15 %. The burning rate, however, decreases from 2.2 to 0.6 cm/s, when the loading density increases from 0 to 80 %. A qualitatively similar trend was observed for 20 μm particles.

- The overall analysis indicates a relative weak dependence of the burning rate on particle size representative of kinetically controlled conditions, which is consistent with the experimental data.

CHAPTER 7

PYROPHORICITY OF NASCENT AND PASSIVATED ALUMINUM PARTICLES AT NANO-SCALES

A comprehensive analysis of pyrophoricity of nascent and passivated aluminum particles is performed by taking into account transient energy balance along with accurate evaluation of physicochemical properties of nano-sized particles. The oxidation mechanism is based on a recently developed Mott-Cabrera oxidation mechanism, which is applicable for spherical nano-particles (Ermoline & Dreizin 2011). The sensitivity of the model results to the choice of physicochemical properties of the particle and gas, polymorphic state of the oxide layer, parameters of the Mott-Cabrera oxidation kinetics, and heat-transfer correlation is analyzed. Both nascent and passivated particles are considered. The temperature and pressure of the ambient environment are chosen as 300 K and 1 atm, respectively. Results from the present work are compared with those of previous theoretical and experimental studies.

7.1 Physicochemical Properties of Nano-Sized Aluminum Particles

It is important to discuss the size-dependence of the physicochemical properties of nano-aluminum particles in the context of the present analysis. This has received little attention from the combustion community. The melting point, T_m, and the enthalpy of fusion, L_{fus}, of aluminum particles can be written as (Zhang, Lu & Jiang 1999)

$$\frac{T_m(R)}{T_{m,b}} = \exp\left(-\frac{\alpha-1}{R/R_0-1}\right), \tag{7.1}$$

$$\frac{L_{fus}(R)}{L_{fus,b}} = \frac{T_m(R)}{T_{m,b}}\left[1 - \frac{1}{(R/R_0 - 1)}\right], \quad (7.2)$$

where R is the particle radius, α = 1.9186, and R_0 = 0.9492 nm. The subscript b refers to the bulk material.

Another thermophysical property of relevance to the present study is the boiling temperature, defined as the temperature at which the vapor pressure is equal to the ambient pressure. The vapor pressure of aluminum near the surface of a liquid droplet, p_D, is calculated using the Kelvin equation (Panda & Pratsinis 1995)

$$p_D = p_0 \exp\left(4\sigma v / k_B T D\right), \quad (7.3)$$

where D is the diameter of the particle, k_B the Boltzmann constant, and v the molar volume. The vapor pressure of aluminum over a flat surface, p_0, and the surface tension of aluminum, σ, are calculated respectively as follows (Hultgren et al. 1973, Rhee 1970):

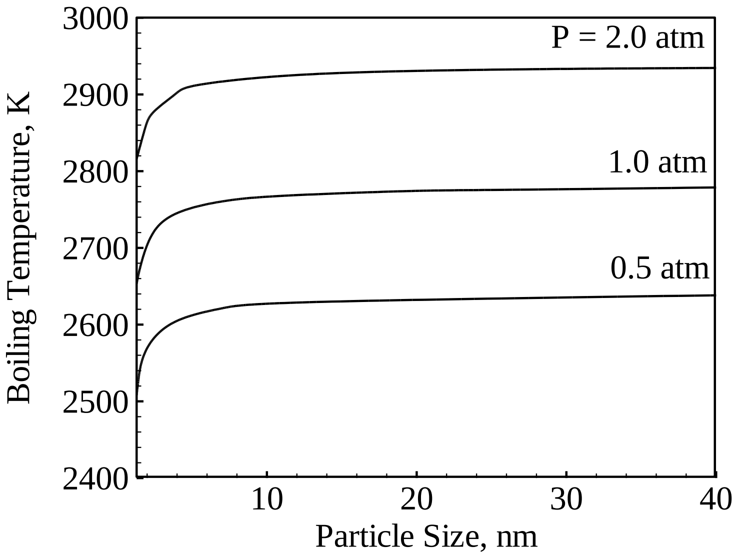

Figure 7.1: Vaporization temperature of aluminum as a function of particle size over a pressure range of 0.5-2.0 atm (Puri 2008).

$$p_0 = p\exp\left(13.07 - \frac{36373}{T}\right), \tag{7.4}$$

$$\sigma = 948 - 0.202T, \tag{7.5}$$

where p is the pressure and T the temperature. Puri (Puri 2008) solved Eqs. (7.3)-(7.5) iteratively and calculated the boiling temperature as a function of the particle size. Figure 7.1 shows the result at three different pressures of 0.5, 1, and 2 atm. The boiling temperature of aluminum increases with increasing pressure. It decreases significantly from the bulk value for particles smaller than 10 nm, a trend that is consistent with those observed for the melting temperature and enthalpy of fusion.

The heat of reaction is another physicochemical property that needs to be specified. It determines the energy release during the formation of the oxide layer on a nascent particle. The theoretical data (Chung et al. 2011) is curve-fitted to obtain a correlation for the heat of reaction of aluminum particles. The result is shown in Fig. 7.2.

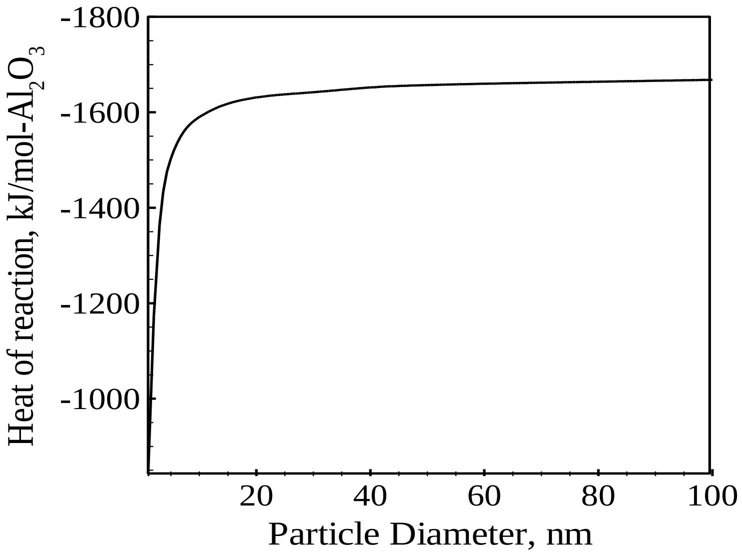

Figure 7.2: Effect of particle size on the heat of reaction of aluminum oxidation in air (Chung et al. 2011).

$$\Delta H_r = -1690 + \frac{865.1}{D^{0.87}}, \tag{7.6}$$

where ΔH_r is the heat of reaction and D the particle size in nm. The heat of reaction decreases with decreasing particle size. In other words, the oxidation reaction is less exothermic for smaller particles.

Another parameter of concern is the density of the aluminum oxide, which exists in many metastable polymorphs. The hexagonally packed α-Al_2O_3 (corundum) has a density of 4 g/cm^3 (Trunov, Schoenitz & Dreizin 2006). Other polymorphs such as γ, δ, and θ phases have face-centered cubic (FCC) structures. The initial oxide layer covering the aluminum particle is amorphous (Trunov, Schoenitz & Dreizin 2006). The density of the amorphous oxide layer is taken to be 3.05 g/cm^3 (Trunov, Schoenitz & Dreizin 2006).

7.2 Steady Homogeneous Gas-Phase Reaction Theory

The analysis performed by Glassman et al. (Glassman, Papas & Brezinsky 1992) assumes homogeneous gas-phase combustion of aluminum vapor and oxidizing species. It neglects heat losses to the ambient environment and size-dependence of physicochemical properties. Under these assumptions, the critical condition for metal pyrophoricity was obtained by equating the chemical heat release to the sum of the energies needed to heat the particle to its boiling point and vaporize the metal (Glassman, Papas & Brezinsky 1992):

$$\frac{\left(1-\left(\delta/R\right)_{cr}\right)^3}{\left\{1-\left(1-\left(\delta/R\right)_{cr}\right)^3\right\}} = \frac{\rho_{Al_2O_3}\left\{\left(-H^o_{ox}\right)-\left(H^o_{T_b}-H^o_{298}\right)\right\}_{Al_2O_3}}{\rho_{Al}\left(H^o_{T_b}-H^o_{298}+L_{vap}\right)_{Al}}, \tag{7.7}$$

where δ is the oxide layer thickness, ρ the density, T_b the boiling point of aluminum, L_{vap} the enthalpy of vaporization of aluminum, and H the enthalpy. The subscripts *ox* and *cr*

Table 7.1: Thermo-physical properties of bulk aluminum and alumina (JANAF Thermodynamic Tables 1981).

Property	**Value**
Density of alumina	4000 kg/m^3
Density of aluminum	2700 kg/m^3
Heat release during oxidation, $-H^o_{298,ox}$	1675 kJ/mol
$H^o_{T_b} - H^o_{298}$	454 kJ/mol
$H^o_{T_b} - H^o_{298} + L_v$	381.67 kJ/mol
Aluminum melting point	940 K
Aluminum boiling point	2740 K
Alumina melting point	2327 K
Alumina volatilization temperature	4000 K

refer to oxidation and critical condition, respectively. For the sake of comparison, bulk values of thermophysical properties are employed. They are obtained from the JANNAF tables and are given in Table 7.1 (JANAF Thermodynamic Tables 1981). Figure 7.3 shows the calculated energy budget of the oxidation process for different particle sizes. The thickness of the oxide layer is chosen as 2.5 nm. The curves corresponding to the total absorbed and released energies intersect at a particle size of 28 nm. The predicted critical particle size agrees reasonably with the value of 28.6 nm reported in Glassman et al.'s work (Glassman, Papas & Brezinsky 1992), thereby demonstrating the accuracy of

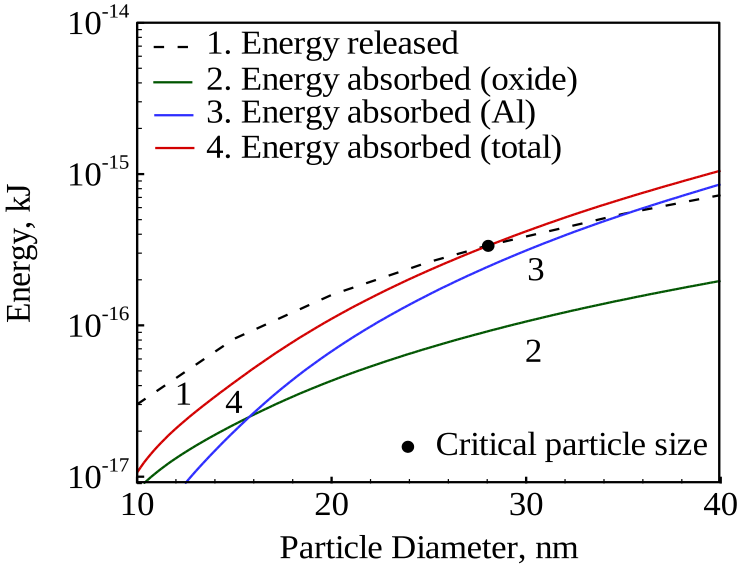

Figure 7.3: Energy distribution for the oxidation of aluminum particles with an oxide layer thickness of 2.5 nm: homogeneous gas-phase reaction theory with bulk properties.

the present calculation.

The size-dependent physicochemical properties discussed in Section 7.1 are used to obtain a revised estimate of the critical particle size. The density of the oxide layer is taken as 3.05 g/cm^3. Figure 7.4 shows the variation of the critical pyrophoricity ratio, $(\delta/R)_{cr}$ and particle size with the oxide layer thickness. The former decreases with increasing oxide layer thickness. It takes a value of 0.217 for an oxide layer thickness of 2.5 nm. The corresponding critical particle diameter (inclusive of the oxide layer) is 23 nm, which is lower than the value of 28 nm predicted using the constant-property assumption. The effect of pressure on the critical particle size is also studied in the range of 0.5-2 atm. Pressure plays a negligible role in the range of 0.5-2 atm. Note that the above estimates only serve as a guideline, since the analysis neglects the effects of heat losses and kinetics of oxidation of aluminum particles.

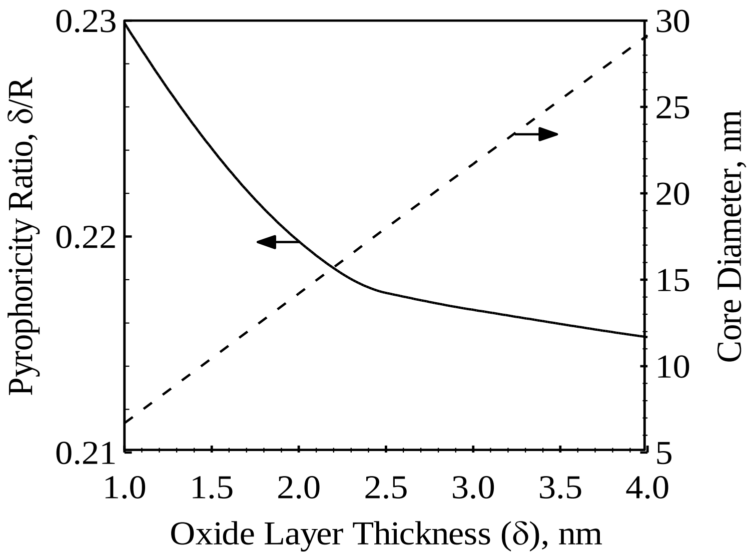

Figure 7.4: Critical pyrophoricity ratio and core diameter as a function of the oxide layer thickness: steady homogeneous gas-phase reaction theory with size-dependent properties.

7.3 Transient Heterogeneous Surface Reaction Theory

7.3.1 Theoretical Framework

When a nascent particle is exposed to the oxidizing gas, the temperature, oxide layer thickness, and core diameter vary continuously with time. As a result, the steady-state assumption is not valid. Particle ignition is a transient process, and the corresponding ignition delay can be characterized by the point at which temperature runaway occurs. During ignition, the rate of chemical energy release competes with that of heat loss to the oxidizing gas. An unsteady energy balance is thus required to obtain an accurate estimate of the critical particle size for pyrophoricity. The analysis follows the approach adopted by Mohan et al. (Mohan, Ermoline & Dreizin 2012), but is extended to include the size and temperature dependencies of particle physicochemical properties.

Application of the energy conservation leads to the following equation:

$$mC_p \frac{dT}{dt} = \dot{h}_{ox} - \dot{q}_{out}, \tag{7.8}$$

where m is the mass of the particle, C_p the specific heat of the particle, T the temperature, t the time, $\dot{h}_{ox}$ the rate of chemical energy release. The density and specific heat are calculated as a function of the particle temperature. The rate of heat loss to the surrounding gas, $\dot{q}_{out}$, consists of contributions from conduction and radiation, denoted by the subscripts c and r, respectively, as follows:

$$\dot{q}_{out} = \dot{q}_c + \dot{q}_r. \tag{7.9}$$

In the continuum regime, the conductive heat transfer between the particle and surrounding gas is controlled by energy diffusion, given by (Filippov & Rosner 2000)

$$\dot{q}_c = 4\pi R \lambda_g \left(T - T_e\right), \tag{7.10}$$

where R is the particle radius and λ_g the thermal conductivity of the gas. The subscript e refers to the ambient condition. For nano-sized particles, the particle size is much smaller than the mean-free-path of oxygen molecules. As a result, the continuum heat transfer correlation ceases to be valid. In the free-molecular regime, the conductive heat-flux is replaced by the molecular heat flux, $\dot{q}_{mol}$, given by (Filippov & Rosner 2000):

$$\dot{q}_{mol} = \alpha \pi R^2 \frac{p_e \sqrt{8k_B T_e / \pi M}}{2} \left(\frac{\gamma^* + 1}{\gamma^* - 1} \right) \left(\frac{T}{T_e} - 1 \right), \tag{7.11}$$

where M is the mass of the oxygen molecule, γ^* the adiabatic constant calculated at a temperature $T^* = (T+T_e)/2$, and $\alpha = 0.85$ the accommodation coefficient (Saxena & Joshi 1989). The radiation heat transfer can be calculated using the Stefan-Boltzmann relation:

$$\dot{q}_r = \varepsilon A\sigma\left(T^4 - T_e^4\right), \tag{7.12}$$

where A is the particle surface area, σ the Stefan-Boltzmann constant, and ε = 0.2 the emissivity of the oxidized aluminum surface (Lide 2003). Equation (7.12) is strictly not valid for nano-sized particles. The Stefan-Boltzmann relation is not expected to be valid at nano-scales and the nano-particle radiation follows T^5-law as opposed to the classical T^4-law (Martynenko & Ognev 2005). The size and temperature dependencies of the particle emissivity must be considered in the analysis. Figure 7.5 shows the effect of particle size on the emissivity of aluminum particles at different temperatures calculated using the magnetic dipole approximation theory (Martynenko & Ognev 2005). The emissivity of nano-sized aluminum is several orders of magnitude lower than its bulk value. A more accurate value of the particle emissivity can be obtained by considering

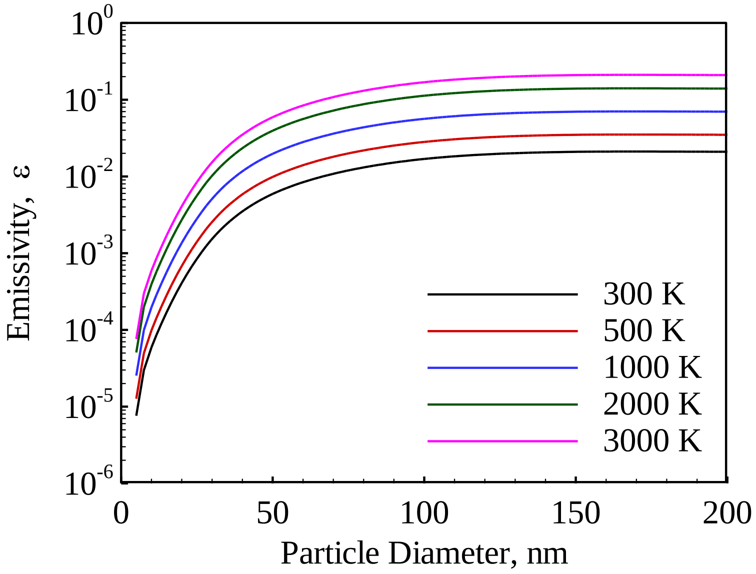

Figure 7.5: Effect of particle size on emissivity of aluminum nano-particles at different temperatures obtained using the magnetic dipole approximation theory (Martynenko & Ognev 2005).

the electrical dipole contribution, which may become significant at higher temperatures (Rosenberg, Smirnov & Pigarov 2008). The present analysis, however, indicates that the model results are insensitive to changes in the particle emissivity.

The heat-release term is calculated using the Mott-Cabrera oxidation kinetics (Jeurgens et al. 2002, Cabrera & Mott 1949). An essential feature of this model is that the metal electrons transverse the thin oxide layer either by thermionic emission or tunneling. The electrons ionize the adsorbed oxygen atoms to create an electrostatic potential between the oxide-oxidizer and oxide-metal interfaces. Figure 7.6 shows the induced electric field in the particle, which significantly lowers the energy barrier for metal ion diffusion, resulting in higher oxidation rates. Ermoline and Dreizin (Ermoline & Dreizin 2011) incorporated the electric-field correction and effects of volume changes in a growing oxide layer and a shrinking aluminum core, and derived the following equations for spherical particles:

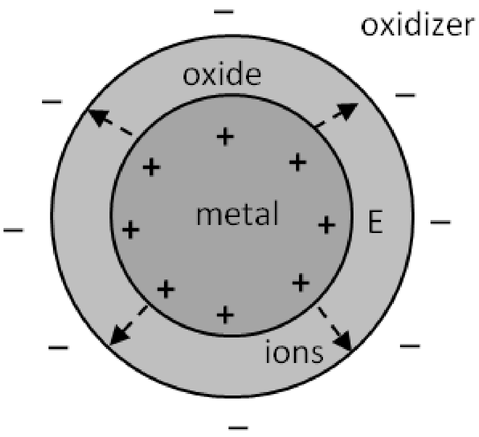

Figure 7.6: Schematic illustrating the Mott-Cabrera oxidation mechanism.

$$\begin{aligned}\frac{d\delta}{dt}&=\left[\left(\Omega_1+\Omega_2\right)\left(\frac{R_c}{R}\right)^2-\Omega_1\right]nv\exp\left(-\frac{W}{k_BT}\right)\exp\left(-\frac{qa\phi_M}{k_BT}\frac{R}{R_c\delta}\right),\\\frac{dR_c}{dt}&=\Omega_1 nv\exp\left(-\frac{W}{k_BT}\right)\exp\left(-\frac{qa\phi_M}{k_BT}\frac{R}{R_c\delta}\right),\end{aligned}\tag{7.13}$$

where R_c is the core radius and δ the oxide layer thickness. The model constants are given in Table 7.2. The rate of chemical heat release can be written as

$$\dot{h}_{ox}=4\pi R_c^{\,2}\rho_{Al}h_r\frac{dR_c}{dt},\tag{7.14}$$

where h_r is the heat of reaction. Equations (7.13) and (7.14) require the presence of an oxide layer on the particle. The formation of the monomolecular oxide layer on a nascent particle is extremely fast and can be treated as an adiabatic process. A detailed justification is given by Mohan et al. (Mohan, Ermoline & Dreizin 2012). Our calculations indicate that the growth of the oxide layer is adiabatic up to a thickness of

Table 7.2: Constants in Mott-Cabrera equations.

Constant	Value
n	10 nm^{-2}
v	10^{12} s^{-1}
a	0.12 nm
φ_m	-1.6 V
W	2.6 eV
q	3e
Ω_1	-0.0166 nm^3
Ω_2	0.023 nm^3

0.3 nm. This further demonstrates the validity of the assumption. As a result, chemical equilibrium analysis can be performed to calculate the particle temperature upon the formation of the 0.3 nm thick (monomolecular) oxide layer. No such calculation is necessary for passivated particles. The energy balance based on chemical equilibrium analysis can be written as

$$\left(m_{Al}C_{p,Al}+m_{ox}C_{p,ox}\right)\left(T_f-300\right)+m_{Al}L_{fus,Al}=-m_{ox}h_{ox}, \tag{7.15}$$

where T_f is the final temperature.

7.3.2 Results and Discussion

The theoretical framework is used to analyze the pyrophoricity of nascent and passivated aluminum particles at nano scales. Initially, the nascent particle is assumed to be devoid of the oxide layer. For passivated particles, the initial values of the oxide layer thickness in the range of 0.3-0.5 nm are considered.

7.3.2.1 Nascent aluminum particles

The growth of an oxide layer on a nascent aluminum particle is divided into two stages. In the first stage, a 0.3 nm thick monomolecular oxide layer is formed. As stated in the previous section, a chemical equilibrium analysis is performed to calculate the particle temperature after the formation of the oxide monolayer. A companion transient energy balance analysis employing the Mott-Cabrera kinetics is conducted to determine the minimum ignition temperature for particles encapsulated with a 0.3 nm thick oxide layer. Ignition is assumed to be achieved when the particle temperature increases monotonically beyond the melting point of the oxide film. If the ignition temperature is lower than the result of chemical equilibrium analysis, the particle can self-ignite due to heterogeneous oxidation reactions beginning at 300 K. It is, thus, considered to be pyrophoric. Figure 7.7 shows the variations of the temperature and oxide layer thickness

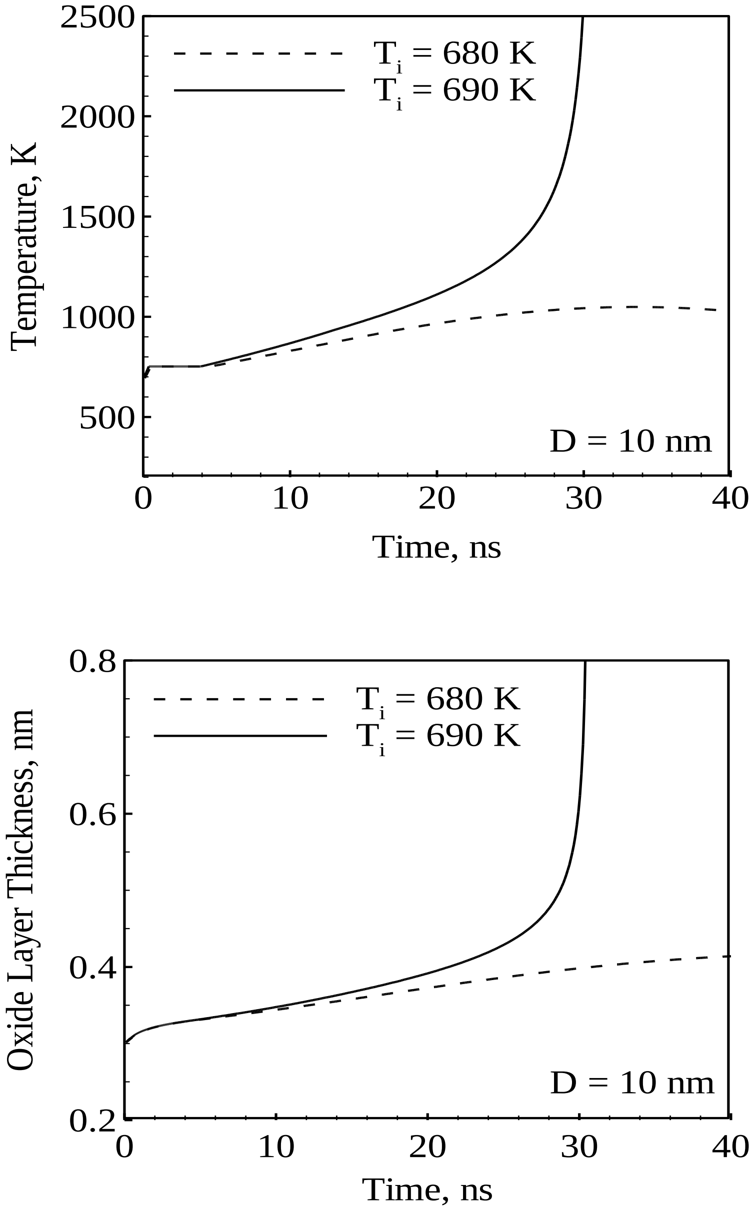

Figure 7.7: Variations of particle temperature and oxide thickness with time for a core diameter of 10 nm and oxide layer thickness of 0.3 nm.

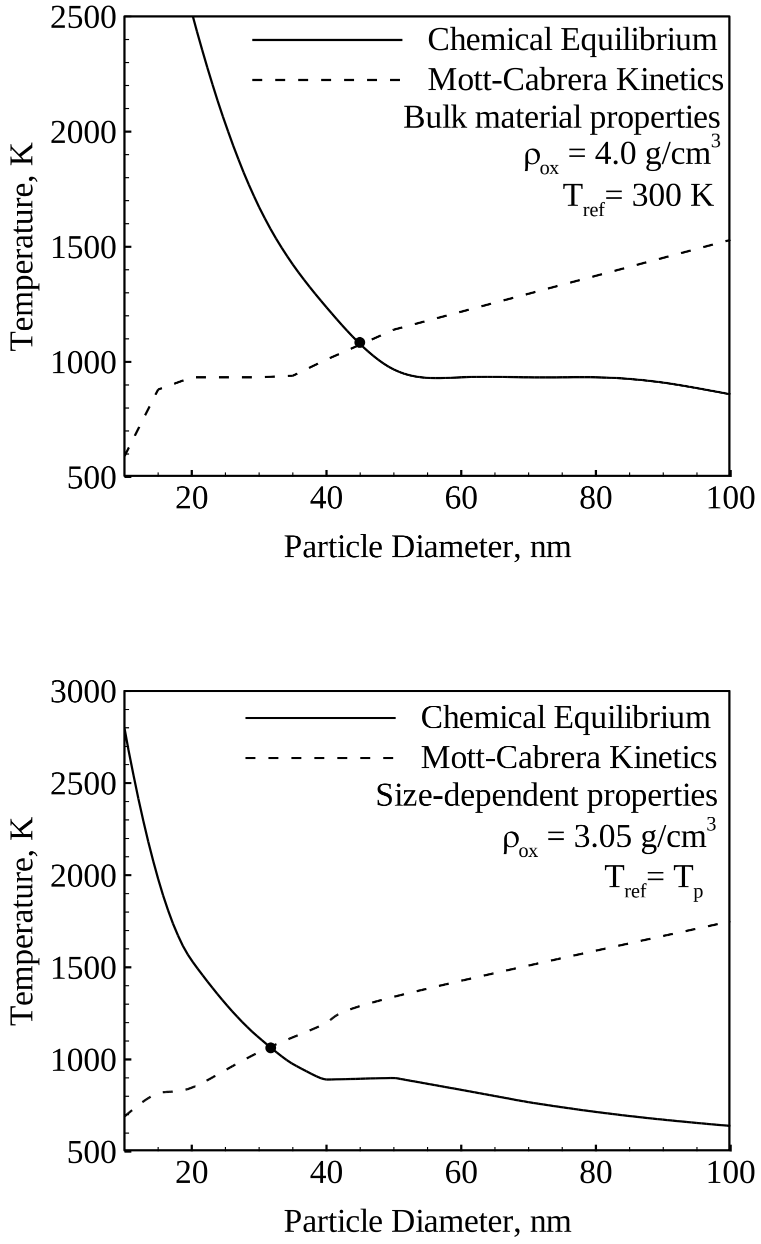

Figure 7.8: Comparison of the particle temperature after the growth of 0.3 nm thick oxide layer and the minimum temperature necessary for ignition for (a) crystalline oxide layer and bulk material properties calculated at room temperature; (b) amorphous oxide layer with temperature and size dependent material properties.

with time for a particle with a core diameter of 10 nm. For an initial temperature of 680 K, the rate of chemical heat-release is not sufficient to balance the heat loss to the ambient environment. As a result, temperature runaway does not occur. The isotherm corresponds to the melting of the core at 750 K, which is lower than the bulk melting point of aluminum by 183 K. The oxide layer thickness follows a similar trend. When the initial temperature is chosen as 690 K, the temperature and oxide layer thickness increase sharply after a time period of 20 ns. The rate of chemical energy release is significantly greater than that of heat loss to the ambient environment. The same phenomenon takes place for all temperatures greater than 690 K. For a particle with a 10 nm core, the minimum ignition temperature is, thus, taken as 690 K. The sensitivity of the results to the ambient temperature stems from the fact that the reaction rate bears an exponential dependence on temperature. A similar analysis is performed for different particle sizes and the corresponding minimum ignition temperature is determined. Figure 7.8 shows the comparison of the results of chemical equilibrium and transient energy balance analyses for two different cases. In the first case, bulk material properties calculated at room temperature are employed. A crystalline aluminum oxide layer with a density of 4.0 g/cm^3 is assumed to cover the active aluminum surface. In the second case, size and temperature dependent properties are used and an amorphous oxide layer with a density of 3.05 g/cm^3 is considered. The chemical equilibrium analysis indicates that the final particle temperature decreases with increasing particle size, since more energy is spent to heat a larger particle. The transient energy balance analysis, on the other hand, suggests that the minimum ignition temperature increases with increasing particle size, since the rate of heat loss to the oxidizing gas is proportional to the particle surface area. The plateau-like feature indicates that the corresponding particles need to be pre-heated to the melting point of the core. These two curves intersect at the critical particle size, the specific value of which is different for the two cases. For the first case, the calculated value is 45 nm. For the second case, the critical particle size is predicted to be 32 nm. Note that the predicted value is more than half the value of 68 nm predicted in the previous study, thereby underlying the importance of accurate evaluation of material properties. The model results are sensitive to the changes in the parameters of the Mott-Cabrera oxidation kinetics. For example, increasing the Mott potential from 1.6 to 1.75 V resulted in an increase in the critical particle size by 18 %. In the above analysis, thermal accommodation coefficient was taken as 0.85. In reality, the accommodation coefficient is a temperature dependent parameter (Altman 1999). Figure 7.9 shows the result when temperature dependence of the thermal accommodation coefficient is considered. The

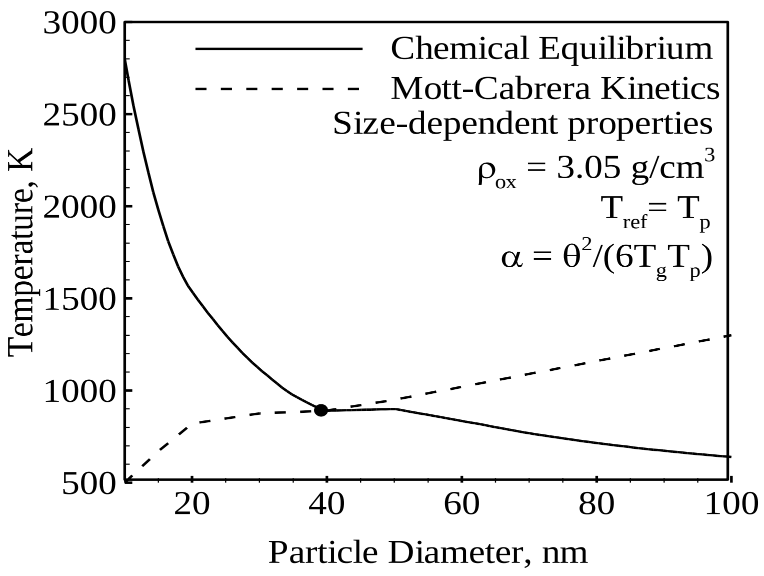

Figure 7.9: Critical particle size predicted using the free-molecular heat transfer correlation in conjunction with temperature dependent accommodation coefficient.

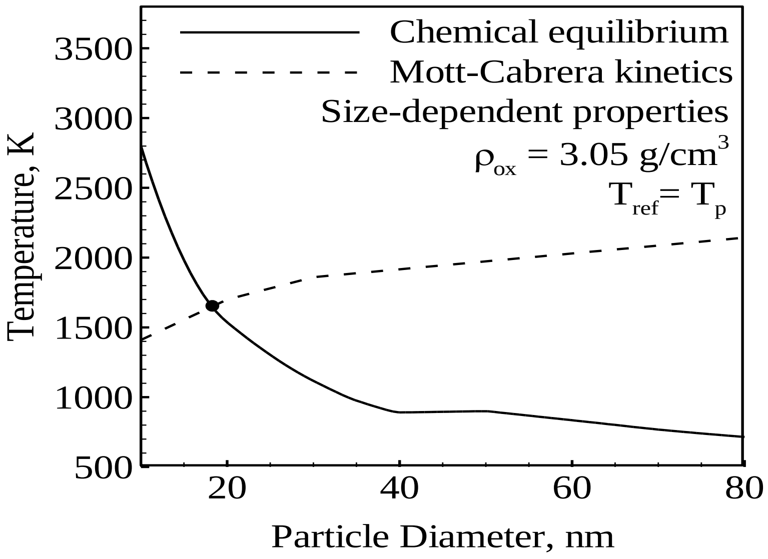

Figure 7.10: Critical particle size predicted using the continuum heat transfer correlation.

accommodation coefficient decreases with increasing temperature and a result the critical particle size increases from 32 nm to 40 nm. In the above analyses, the free-molecular regime heat transfer model is employed. Figure 7.10 shows the result when the continuum hypothesis is invoked. It overestimates the heat losses to the ambient environment. As a result, particles need to be heated to higher temperatures for ignition to occur. The calculated critical particle size of 18 nm is significantly lower than the value obtained using the model for the free-molecular regime. The continuum heat transfer correlation gives inadequate description of ignition and combustion of nano-sized particles. Table 7.3 shows the comparison between the predictions of different models and experimental data. Results from the present analysis exhibit reasonably good agreement with experimental data (Glassman, Papas & Brezinsky 1992), thereby confirming the validity of the proposed model.

Table 7.3: Critical particle size predicted by different models and their comparison with experimental data.

Model			**Critical particle size, nm**
Steady-state, homogeneous gas-phase reaction theory	Constant properties		23
	Size-dependent properties		18
Transient heterogeneous surface reaction theory	Diffusion oxidation model		20
	Mott-Cabrera kinetics	Free molecular	32
		Continuum	18
Experimental data			30

7.3.2.2 Passivated aluminum particles

The same approach is adopted for passivated aluminum particles, except that the chemical equilibrium analysis is not employed. The oxide layer thickness is varied in the range of 0.3-0.5 nm. Figure 7.11 shows the temporal evolution of the temperature for particles with a core diameter of 3.8 and 6 nm along with an oxide layer thickness of 0.3 nm. At 300 K, temperature runaway is observed only when the particle size is 3.8 nm and, thus, the critical particle size is 3.8 nm. Figure 7.12 shows the temperature evolution for a core diameter of 3.8 nm and shell thickness in the range of 0.3-0.5 nm. Particles with 0.4 and 0.5 nm thick oxide layers remain stable at 300 K, suggesting that oxide layers thicker than 0.3 nm render the particle to be non-pyrophoric. Aluminum particles

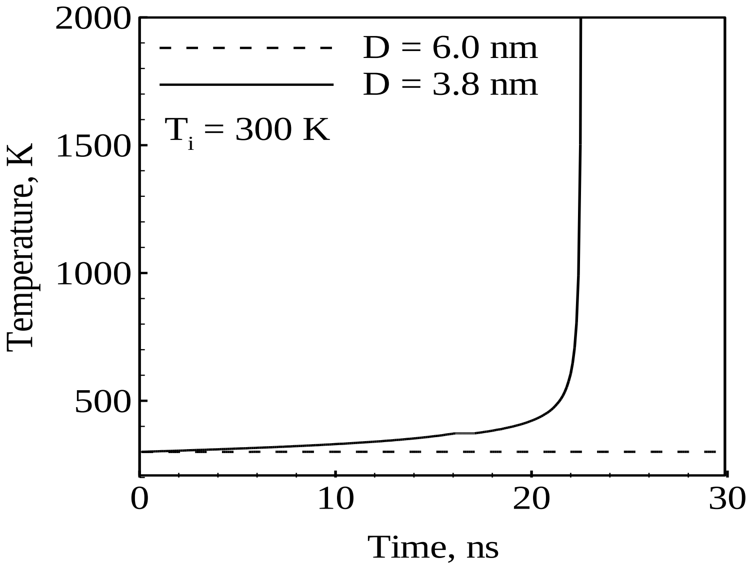

Figure 7.11: Variation of particle temperature with time for core diameters of 3.8 and 6 nm and oxide layer thickness of 0.3 nm.

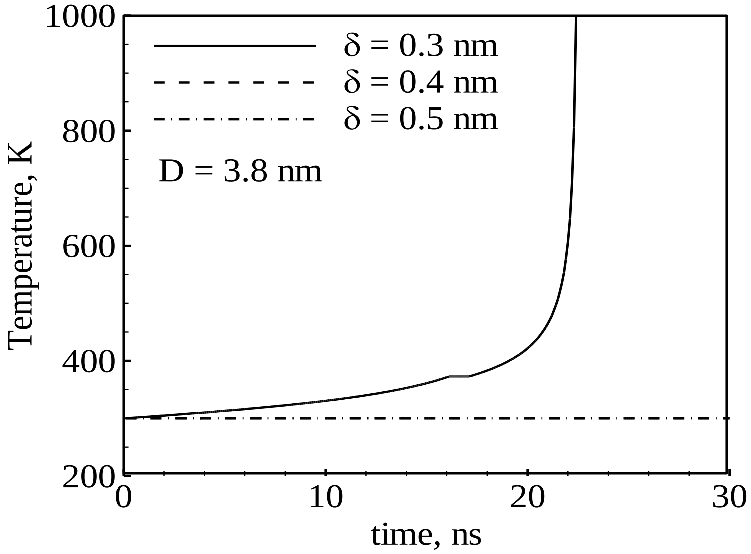

Figure 7.12: Variation of particle temperature with time for a core diameter of 3.8 nm and oxide layer thickness of 0.3, 0.4, and 0.5 nm.

are typically covered by an oxide layer, which can have thickness in the range of 0.5-4 nm (Trunov, Schoenitz & Dreizin 2006). Moreover, particles smaller than 3.8 nm are not of practical interest. As a result, commercially available passivated particles are found to be non-pyrophoric.

7.4 Summary

The major results of the analysis presented in this chapter are summarized as follows:

- Pyrophoricity of nascent and passivated aluminum particles is studied using homogeneous gas-phase reaction and heterogeneous surface reaction theories. The study incorporates accurate evaluation of material properties including the size dependence of physicochemical properties of the particle at nano-scales. Free-molecular heat transfer effects are also considered.

- The homogeneous gas phase reaction theory indicates that particles smaller than 18 nm are pyrophoric. The predicted value is, however, expected to serve only as a guideline, since the analysis neglects the important effects of heat losses and kinetics of aluminum oxidation at nano-scales.
- The heterogeneous oxidation theory predicts a critical particle size of 32 nm, which is substantially lower than the previously predicted value of 68 nm. The predicted value agrees reasonably well with the experimental data. The results underline the importance of accurate evaluation of material properties including the size dependence of physicochemical properties of the particle and polymorphic state of the oxide film.

- The continuum heat transfer model significantly overestimates the heat losses and predicts a lower critical particle size of 18 nm. Free-molecular effects are, thus, important for analysis of particle ignition at nano-scales.

- The critical particle size predicted for aluminum particles passivated with a 0.3 nm thick oxide layer is 3.8 nm. Thicker oxide layers render the particle to be non-pyrophoric. As a result, commercially available nano-aluminum particles which have oxide layer thickness in the range of 2-4 nm are predicted to be thermally stable.
- The model results are found to be sensitive to the choice of physicochemical properties, polymorphic state of the oxide film, and parameter of the Mott-Cabrera kinetics. The critical particle size increases by 40 %, when bulk material properties evaluated at room temperature are used and oxide layer is assumed to be in crystalline form. It increases by 18 %, when the Mott potential increases from 1.6 to 1.75 V.

CHAPTER 8

IGNITION OF PASSIVATED ALUMINUM PARTICLES

8.1 Knudsen Number Analysis

Theoretical analysis of ignition and combustion of metal particles are typically based on continuum heat transfer model. The results indicate that the ignition delay and burning time follow d^2-law. For nano-sized particles, the continuum hypothesis is not valid. The mean free path, λ, of oxygen molecules can be expressed as

$$\lambda = \frac{RT}{\sqrt{2}\pi D^2 N_A p}, \tag{8.1}$$

where R is the universal gas constant, T the temperature, p the pressure, N_A the Avogadro's number and D the diameter of the gas molecule. The Knudsen number, *Kn*, is the ratio of the mean free path to the particle diameter, d. The continuum hypothesis is

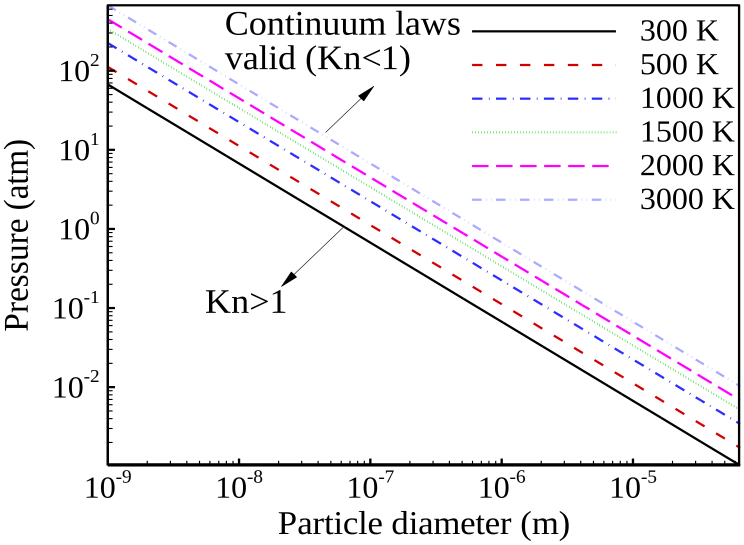

Figure 8.1: Knudsen limits as a function of particle diameter and pressure at different temperatures (Puri 2008).

not valid, when the Knudsen number is greater than unity. This is typically achieved for smaller particles, higher temperatures, and lower pressures. Equation (8.1) can be used to construct the regime diagram, so that the exact conditions of validity of the continuum hypothesis could be ascertained. This is shown in Fig. 8.1 (Puri 2008). At a pressure of 1 atm and combustion temperature of 3000 K, the continuum hypothesis breaks down at a particle size of 700 nm. As a result, free-molecular effects must be considered when studying ignition and combustion of nano metallic particulates. The results are naturally expected to be different.

8.2 Ignition Delay of Aluminum Particles

In the present study, an energy balance analysis is performed to calculate the ignition delay of aluminum particles for different particle sizes. The energy balance can be written as

$$m_p C_p \frac{dT}{dt} = \dot{h}_{ox} - \dot{q}_{out}, \tag{8.2}$$

where m is the mass, C_p the specific heat, T the temperature, t the time, and $\dot{h}_{ox}$ the chemical energy release rate. The subscript p refers to the particle. The rate of heat exchange between the particle and gas is given by

$$\dot{q}_{out} = \dot{q}_c + \dot{q}_r, \tag{8.3}$$

where the subscripts c and r denote conduction and radiation, respectively. In the continuum regime, the rate of conduction heat transfer is given by (Filippov & Rosner 2000)

$$\dot{q}_c = 4\pi r \lambda_g \left(T - T_g\right). \tag{8.4}$$

Here, r is the particle radius and λ the thermal conductivity. The subscript g refers to the gas. The conduction heat transfer rate is linearly proportional to the particle size and is independent of the gas pressure. In the free-molecular regime, the conductive heat transfer term is replaced by the molecular counterpart (Filippov & Rosner 2000)

$$\dot{q}_{mol} = \alpha \pi r^2 \frac{p_g \sqrt{8k_B T_g / \pi M}}{2} \left(\frac{\gamma + 1}{\gamma - 1} \right) \left(\frac{T}{T_g} - 1 \right), \tag{8.5}$$

where M is the mass of the oxygen molecule, k_B the Boltzmann constant, γ the adiabatic constant, p the pressure, and α the accommodation coefficient. The molecular heat transfer rate bears a quadratic dependence on the particle size and depends on the gas pressure. For simplicity, the radiation heat transfer is modeled using the Stefan-Boltzmann relation

$$\dot{q}_r = \varepsilon A \sigma \left(T^4 - T_g^4 \right), \tag{8.6}$$

where A is the particle surface area, σ the Stefan-Boltzmann constant, and ε the emissivity

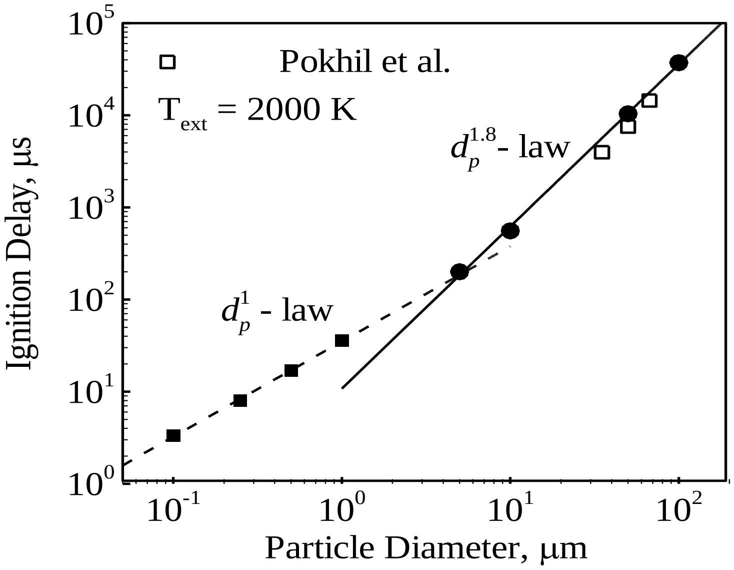

Figure 8.2: Ignition delay as a function of particle size calculated using a thermal model based on Mott-Cabrera kinetics.

of the oxidized aluminum surface. The oxidation rate is calculated using the Mott-Cabrera oxidation kinetics (Ermoline & Dreizin 2011). Ignition delay is defined as the time delay until temperature runaway is observed. Figure 8.2 shows the calculated ignition delay as a function of diameter of aluminum particles. For micron-sized particles, the ignition delay bears a quadratic dependence on the particle size. Reasonably good agreement with the experimental data is achieved. At nano-scales, the particle size exerts relatively weak effect on the ignition delay. It is satisfactory to note that the analysis qualitatively captures the trend shown in Fig. 1.15. The predicted diameter exponent is, however, greater than the experimental value of 0.25. One possible reason is that the present study deals with an isolated particle, whereas the experiments consider a collection of particles that could undergo sintering and agglomeration (Young et al. 2009). The present analysis suggests that the change in the size dependence of the ignition delay is primarily caused by the transition of the heat transfer mode from the continuum to free-molecular regime. A similar trend was observed for magnesium particles (Mohan, Trunov, & Dreizin 2008). The authors, however, did not discuss the particle size effect on the ignition delay.

8.3 Ignition Temperature of Aluminum Particles

It is important to calculate the size dependence of the ignition temperature of aluminum particles by considering free-molecular heat transfer effects. The ignition analysis is based on the theory of polymorphic phase transformations proposed by Trunov et al. (Trunov, Schoenitz & Dreizin 2006). In the previous study, the predicted values were greater than the experimental data. For example, the ignition temperature of 100 nm aluminum particle was predicted to be 1250 K, which is greater than the experimental value by ~300 K. The disparity was attributed to the fact that the measured ignition temperatures correspond to a collection of particles (powder) rather than an isolated particle. In the present study, the energy balance analysis is similar to the one described in the previous section, except for the heat release term, which is written as (Trunov, Schoenitz & Dreizin 2006)

$$\dot{q}_{ch} = H_{ox}\left(\rho_{am}\frac{dV_{am}}{dt} + \rho_{\gamma}\frac{dV_{\gamma}}{dt} + \rho_{\alpha}\frac{dV_{\alpha}}{dt}\right), \tag{8.7}$$

where H_{ox} is the enthalpy of oxidation and ρ the density. The subscripts *am*, γ, and α refer to amorphous, gamma, and alpha polymorphs of the oxide, respectively. The chemical energy release is due to the net increase in the mass of the oxide layer. Detailed description of the terms and approach employed to calculate the heat release term (Trunov, Schoenitz & Dreizin 2006) are given in Appendix A. The particle, which is assumed to be covered by an amorphous oxide layer of thickness 2.5 nm, is initially at 300 K. The gas pressure is taken as 1 atm. The temperature and oxide layer thickness are calculated as a function of time. The particle is considered to ignite if its temperature

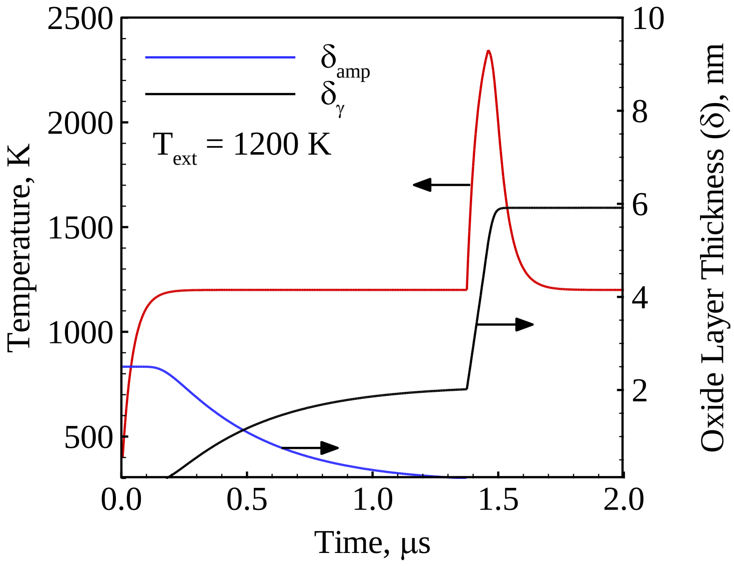

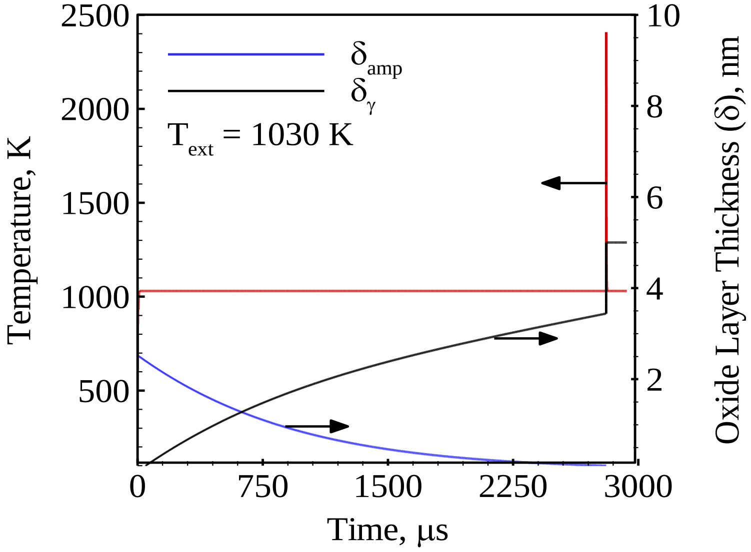

Figure 8.3: Variation of temperature and oxide layer thickness with time for a particle with a diameter of 100 nm and oxide layer thickness of 2.5 nm; (a) continuum-regime model, (b) free-molecular regime model.

reaches the oxide melting point, 2350 K. Figure 8.3 shows the variation of the temperature and oxide layer thickness with time for a 100 nm particle. The thickness of the amorphous oxide layer decreases due to amorphous-gamma polymorphic phase transformation. The amorphous oxide layer disppears before polycrystalline γ-alumina (thickness greater than 5 nm) is formed. As a result, the newly formed γ-alumina crystallites offer negligible diffusion resistance and the oxidation is controlled by gas-phase diffusion to the particle surface. This results in a sharp increase in the oxidation rate, thereby causing the particle temperature to reach a value of 2350 K. For the continuum heat transfer model, the ignition temperature is predicted to be 1200 K, which agrees reasonably well with the prediction of Trunov et al. Ignition is, however, observed at a temperature of 1030 K, when free-molecular heat transfer effects are

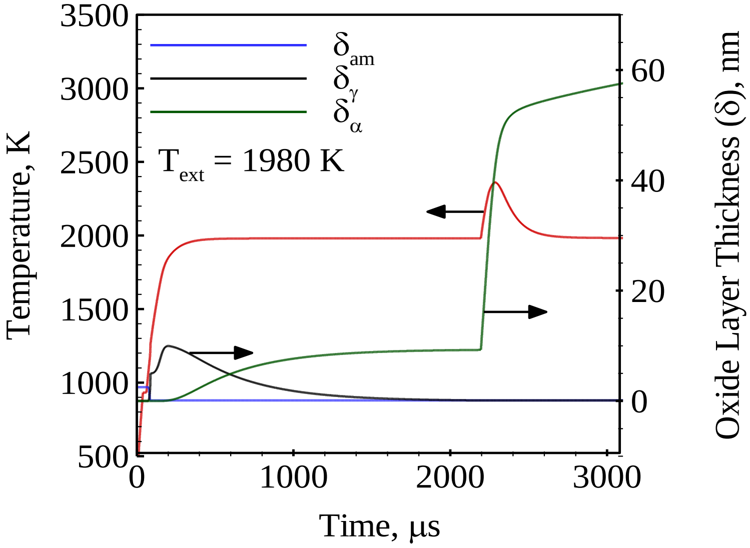

Figure 8.4: Variation of temperature and oxide layer thickness with time for a particle with a diameter of 5 μm and oxide layer thickness of 2.5 nm; free-molecular regime model.

considered. The disparity between the values predicted by Trunov et al. and experimental data is thus not due to multi-particle effect. The analysis demonstrates that an isolated nano-aluminum particle can ignite at ~1000 K. The continuum heat transfer model over predicts the heat losses, thereby resulting in higher ignition temperatures. Figure 8.4 shows the temperature and oxide layer thickness as a function of time for a particle diameter of 5 μm. Note that low-temperature physicochemical processes (such as amorphous–gamma phase transformation) provide insufficient thermal energy for ignition. Ignition is achieved due to gamma-alpha phase transformation at 1980 K. Figure 8.5 shows the effect of particle size on the ignition temperature of aluminum particles in oxygenated environments. The ignition temperature increases from 1000 to 2350 K, when the particle size increases from 100 nm to 100 μm. Reasonably good agreement

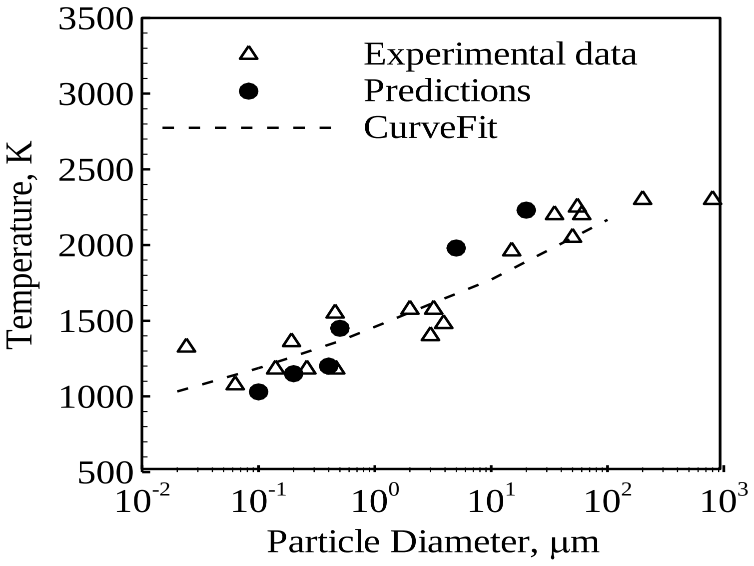

Figure 8.5: Effect of particle size on ignition temperature of aluminum particles in oxygenated environments.

with the experimental data of Huang et al. (Huang et al. 2009) is achieved. The above analysis underlines the importance of free-molecular effects in the ignition analysis of nano-sized aluminum particles.

8.4 Summary

The major results of the analysis presented in this chapter are summarized as follows:

- An energy balance analysis based on Mott-Cabrera oxidation kinetics is performed to determine the effect of particle size on the ignition delay of aluminum particles. For micron-sized particles, the ignition delay bears a quadratic dependence on the particle size. At nano-scales, a linear dependence is predicted. The change in the particle size effect is primarily attributed to the transition of the heat transfer mode from continuum to free-molecular regime.

- The effect of particle size on the ignition temperature of aluminum particles is calculated based on the theory of polymorphic phase transformations developed by Trunov et al. In the present study, free-molecular heat transfer effects are considered. The predicted ignition temperature of isolated nano-aluminum particle is 1030 K, which is significantly lower than the value obtained using the continuum heat transfer model (~1250 K). The calculated ignition temperatures agree reasonably well with the experimental data for a wide range of particle sizes.

CHAPTER 9

SUMMARY AND RECOMMENDATIONS FOR FUTURE WORK

9.1 Summary

The present work addressed several unresolved issues concerning the fundamental physicochemical properties of metal-based nano-energetic materials through appropriate modeling strategies. Both single particles and particle-laden mixtures were considered. Atomistic scale simulations were performed to investigate the properties of monometallic and bimetallic particles with diameters lower than 20 nm. Classical energy and mass balance analyses were employed to treat larger particles and study more complex phenomena.

The size dependence of the melting temperature of nascent aluminum and nickel particles and thermo-chemical behavior of nickel-aluminum particles in the size range of 3-18 nm were studied using molecular dynamics simulations (Sundaram, Puri & Yang, 2013). Emphasis was placed on the effects of core size and shell thickness on the particle melting behavior, diffusion characteristics, and inter-metallic reactions. The melting temperature of the core was strongly dependent on the nature of the shell. For nickel–coated aluminum particles, the core was superheated above the melting temperature of a nascent particle due to the cage-like effect imposed by the solid nickel shell. For aluminum-coated nickel particles, no such phenomenon was observed, since the shell melted before the core. The melting temperatures of the core and shell increased with increasing core size and shell thickness, respectively. The diffusion process, which became prominent upon melting, was followed by inter-metallic reactions that self-heated the particle due to the formation of low-energy nickel-aluminum species. The adiabatic reaction temperature was strongly dependent on the core diameter and shell thickness. Estimates of the diffusion coefficient of aluminum and nickel atoms were also obtained. These are likely to be useful for the development of macro-scale models for the ignition and combustion of nickel-aluminum particles. The study demonstrated that the dimensions of the core and shell can be varied so as to tailor the physicochemical properties of these particles.

A theoretical model was developed to investigate the combustion of nano-aluminum particles and liquid water/ice mixture for particles in the size range of 38-130 nm and over a pressure range of 1-10 MPa (Sundaram et al. 2013). A multi-zone framework was established to predict the burning properties and flame structure by solving the conservation equations in each zone and enforcing the mass and energy continuities at the interfacial boundaries. Emphasis was placed on the effects of particle size and pressure on the temperature distribution and burning rate. An analytical expression for the burning rate was also derived. Key parameters that dictated the burning rate were identified as thermal diffusivity, heat of reaction, ignition temperature, and burning time. The pressure dependence of the burning rate stemmed from the dependence of the particle burning time on pressure at nano-scales. The disparities in the measured burning rate pressure exponents were attributed to the changes in the consistency of the mixture. The study revealed that the inverse dependence of the burning rate on particle size was a result of the quadratic dependence of the burning time on particle size. Based on time-scale arguments, the rate-controlling mechanism was hypothesized to be species diffusion processes across the oxide layers of the particles. The sensitivity of the burning rate to changes in the thermal diffusivity, flame temperature, and burning time was also determined. The impact of some of the assumptions (such as negligible particle entrainment and agglomeration) on the model predictions was briefly discussed. The study also revealed that freezing the water negligibly affects the burning properties of the mixture. The effect of bimodal particle size distribution on the burning rate was explored. The analysis revealed a weak dependence of the burning rate on particle size, which was indicative of kinetically-controlled burning regime. The validity of inverse relationship between the burning rate and particle size (observed at nano-scales) is thus limited and cannot be directly extrapolated for larger (or micron-sized) particles.

Energy balance analyses were performed to study the ignition characteristics of nascent and passivated aluminum particles (Sundaram et al. 2013). Emphasis was placed on the determination of the critical particle size at which nano-aluminum particles become pyophoric. The work employed transient energy balance with accurate evaluation of material properties, effects of free-molecular and radiation heat losses, and Mott-Cabrera oxidation mechanism. Nascent aluminum particles smaller than 32 nm were predicted to be pyrophoric. For an oxide layer thickness of 0.3 nm, the critical particle size was estimated to be 3.8 nm. Oxide layers thicker than 0.3 nm rendered the particle to be non-pyrophoric. The effect of particle size on the ignition temperature and ignition delay of aluminum particles was also studied. The weak dependence of the ignition delay on particle size at nano-scales was attributed to the transition from continuum to free-molecular heat transfer regime.

9.2 Recommendation for Future Work

Metals such palladium are more beneficial than nickel from a purely energy perspective. The thermo-chemical behavior of such inter-metallic systems could be investigated using molecular dynamics simulations. It would be also useful to develop a classical flame propagation model and study the flame propagation characteristics of nickel-coated nano-aluminum powders.

The present study captures the important features of the combustion of nano-aluminum and water mixtures. Favorable agreement with experimental data was achieved. A more advanced multi-phase model that considers particle-particle interactions, inertial and gravitational forces acting on the particles, and confining effect of the quartz tube may be developed to understand complex phenomena such as aggregation, agglomeration, and convective motion of the particles. The issue of radiation preheating may also be studied. From an experimental point of view, further measurements of the burning rate for larger particle sizes are necessary to solidify the particle size dependence of the burning rate. The proposed model can also be employed to study the combustion characteristics of nano-aluminum particles and hydrogen peroxide mixture.

The weak dependence of the burning time on particle size at nano-scales is not completely understood. It is speculated that transition of the heat and mass transfer modes from continuum to free-molecular regime, sintering and agglomeration of particles, and finite-rate kinetics are responsible for the observed trend. It would most helpful to develop a theoretical model to study the heterogeneous combustion of nano-sized aluminum particles. Further measurements of the burning time of nano-aluminum particles at elevated pressures and temperatures and for different oxidizers are also desired.

APPENDIX A

EVALUATION OF REACTION RATE TERM FOR THE IGNITION ANALYSIS

The approach is based on semi-empirical formulation developed by Trunov et al. (Trunov, Schoenitz & Dreizin 2006). The mass of the oxide layer polymorph changes due to oxidation reactions and polymorphic phase transformation. The rate of mass change of the oxide polymorph due to oxidation is given by

$$\dot{m}_i^{ox} = \frac{C_i \exp\left(-E_i / RT_p\right)}{1/r_{i-1} - 1/r_i}, \tag{A.1}$$

where m is the mass, r the radius, E the activation energy, C the pre-exponential constant, and T_p the particle temperature. The subscripts i and i-1 refer to the old and new oxide polymorph, respectively. The constants are given in Table A.1. The rate of mass change of the oxide polymorph due to polymorphic phase transformation is expressed as

$$m_{(i-1)\to i}^{tr} = 4\pi r_{i-1}^2 \rho_{i-1} F_{(i-1)\to i} T_p \exp\left(-\frac{E_{(i-1)\to i}}{RT_p}\right)\left\{1 - \exp\left(-\frac{K_{(i-1)\to i} h_{i-1}}{RT_p}\right)\right\}, \tag{A.2}$$

where ρ is the density and R the gas constant. Note that Eq. (A.1) is used for a regular polycrystalline oxide layer (oxide layer thickness greater than h_e). Note that the oxide layer offers negligible resistance for thickness lower than transition value, h_m. The transition oxide layer thickness is taken as 5 nm and 30 nm for γ and α polymorphs, respectively. For oxide layer thickness between h_m and h_e, the pre-exponential constant is given by

Table A.1: Kinetic parameters for the ignition model of aluminum particles.

Parameter	**Value**
E_{am}	120 kJ/mol
E_{γ}	227 kJ/mol
E_{α}	306 kJ/mol
C_{am}	5.098×10^{-8} kg/m/s
C_{γ}	4.0784×10^{-3} kg/m/s
C_{α}	2.3791×10^{-2} kg/m/s
$E_{am\rightarrow\gamma}$	458 kJ/mol
$E_{\gamma\rightarrow\alpha}$	394 kJ/mol
$K_{am\rightarrow\gamma}$	1×10^{12} J/mol/m
$K_{\gamma\rightarrow\alpha}$	1×10^{8} J/mol/m
$F_{am\rightarrow\gamma}$	2×10^{15} m/s/K
$F_{\gamma\rightarrow\alpha}$	5×10^{16} m/s/K

$$C_i' = C_i\left[X_i - \left(X_i - 1\right)\frac{h_1 - h_i^m}{h_i^e - h_i^m}\right], \tag{A.3}$$

$$h_i^e = 2h_i^m + G_i \exp\left(-L_i\beta\right), \tag{A.4}$$

where $G_\gamma = 7.71$ nm, $G_\alpha = 116$ nm, $L_\gamma = 1.066$ s/K, $L_\alpha = 0.439$ s/K, and β the heating rate. For oxide layer thickness lower than $h_{m,}$ the oxidation rate was assumed to be controlled by diffusion of oxidizer molecules to the particle surface

$$m_{\gamma,O_2}^{ox} = -\log\left(1-\chi\frac{\mu_{O_2}}{\mu_{gas}}\right)\frac{8\pi\mu_{Al_2O_3}}{3\mu_{O_2}}\rho D r_p f, \tag{A.5}$$

where D is the diffusion coefficient of oxygen in air, r_p the particle radius, ρ the gas density μ the molar mass, f the fraction of exposed core area, and χ the mole fraction of oxygen in gas. The fraction of open surface area is taken as 0.17 for amorphous-gamma transformation and 0.083 for gamma-alpha phase transformation.

APPENDIX B

RADIATION HEAT TRANSFER IN PARTICLE LADEN MIXTURES

It is important to discuss the role of radiation heat transfer during the flame propagation of particle laden mixtures. For the problem of interest, the mixture consists of multi-phase chemically reacting, emitting, absorbing, and scattering media surrounded by a solid enclosure (quartz tube). There are two conceivable effects of radiation heat transfer. Radiation from reaction and post combustion zones can preheat the unburned mixture and increase the flame propagation rate. Radiation heat transfer from surfaces may also lower the flame temperature, thereby reducing the flame speed. In the present work, the flame temperature was taken to be equal to the actual flame temperature to incorporate the effects of heat losses and incomplete combustion. The preheating effect however needs additional consideration.

The general equation for the radiation heat transfer is (Howell & Siegel 2002)

$$\frac{dI}{dx} = K_a I + K_s I - K_a I_b, \tag{B.1}$$

where K_s, K_a, and I are the scattering coefficient, absorption coefficient, and radiation intensity, respectively. Note that the actual RTE (radiation transport equation) is an integro-differential equation. For simplicity, the contribution of multiple scattering (which could be important) is not considered here. Equation (B.1) states that the radiation intensity increases due to absorption and scattering and decreases due to emission. The absorption and scattering coefficients can be written as

$$K_a = \frac{3Q_a B}{2\rho_p d_p}, \tag{B.2}$$

$$K_s = \frac{3Q_s B}{2\rho_p d_p}, \tag{B.3}$$

where Q is the absorption/scattering efficiency, B the mass density of particles, ρ_p the particle density, and d_p the particle diameter. In the reaction zone, the temperature reaches a value as high as ~2000 K. Accordingly, the wavelength of radiation is greater than or equal to about 1 μm, which is significantly greater than the particle size. An important parameter is $\alpha = \pi d/\lambda$, which is lower than unity in the present study. In this regime, the absorption and scattering efficiencies can be expressed as (Rosenberg, Smirnov & Pigarov 2008):

$$Q_a = \frac{24nk\alpha}{\left(n^2 - k^2 + 2\right)^2 + 4n^2k^2}, \tag{B.4}$$

$$Q_s = \frac{8\alpha^4}{3} \frac{36n^2k^2 + \left(2n^2k^2 - k^2 + n^2 - 2 + n^4 + k^4\right)^2}{\left(\left(n^2 - k^2 + 2\right)^2 + 4n^2k^2\right)^2}, \tag{B.5}$$

where $m = n - ik$ is the complex index of refraction. If one assumes that in the preheat zones the radiation intensity is only converted into internal energy through absorption (i.e., neglecting emission), the radiation heat transport equation in preheat zone can be written as

$$\frac{dI}{dx} = K_t I, \tag{B.6}$$

where $K_t = K_a + K_s$ is the total extinction coefficient. If the radiation intensity at ignition front ($x = 0$) is taken as I_f, the radiation intensity at any location in the preheat zone can be written as

$$I = I_f \exp\left(K_t x\right). \tag{B.7}$$

The heat source term in the energy equation then becomes

$$q_r = K_a I_f \exp\left(K_t x\right). \tag{B.8}$$

Thermal energy of the unburned mixture is increased due to absorption of radiation intensity in the preheat zone. In the flame zone, emission must be also considered and the corresponding radiation transport equation can be written as

$$\frac{dI}{dx} = K_t I - K_a I_b. \tag{B.9}$$

If I_0 is the radiation intensity originating at the end of post combustion zone (taken as origin in this analysis), the intensity at any location downstream can be calculated by solving the above differential equation

$$I = \frac{K_a}{K_t} I_b \left(1 - \exp\left(-K_t x\right)\right) + I_0 \exp\left(-K_t x\right). \tag{B.10}$$

For small values of $K_t x$, the intensity is approximately equal to $I_{0.}$ The intensity at the ignition front may be taken as

$$I_f = \frac{K_a}{K_t} I_{bf}\ , \tag{B.11}$$

$$I_{bf} = \frac{\sigma T_f^4}{\pi}. \tag{B.12}$$

For the multi-phase mixture, the total absorption coefficient may be defined as

$$K_a = K_{a,g}\left(1 - \frac{4}{3}\pi r_p^3 N_p\right) + K_{a,p}, \tag{B.13}$$

where r_p and N_p are the radius and number density of the particles. The subscripts g and p refer to gas and particle, respectively. The complex index of refraction of materials and attenuation coefficient of gases are functions of wavelength and are available in the literature. At a wavelength of 1 μm, the real and imaginary parts of refractive index of aluminum oxide are 1.75 and 10^{-6}, respectively. For liquid water and ice, the attenuation coefficient is on the order of 10 m^{-1} at 1 μm and varies significantly with the wavelength. The available data can be used to calculate the total absorption and extinction coefficients of the mixture, which is an important parameter in Eq. (B.8). With the new source term in the energy equation in the preheat zone, the temperature distributions in the preheat zones are given by

Aluminum-Ice zone

$$T = T_u + \left(T_m - T_u\right)\exp\left(k_1\left[x + t_1 + t_2\right]\right) - \frac{K_a I_f}{\lambda_1\left(K_t^2 - k_1 K_t\right)}\left(\exp\left(K_t x\right) - \exp\left(k_1 x + \left[t_1 + t_2\right]\left[k_1 - K_t\right]\right)\right) \tag{B.14}$$

Aluminum-Water zone

$$T = T_{vap} + \frac{\left(T_{vap} - T_m\right)}{1 - \exp\left(-k_2 t_2\right)}\left[\frac{\exp\left(k_2 x\right)}{\exp\left(-k_2 t_1\right)} - 1\right] - \frac{K_a I_f}{\lambda_2\left(K_t^2 - k_2 K_t\right)}\left(\begin{array}{l}\exp\left(K_t x\right) + \exp\left(-K_t t_1\right)\left[\dfrac{1 - \exp(-K_t t_2)}{1 - \exp(-k_2 t_2)} - 1\right] - \\ \exp\left(-K_t t_1 + k_2(x + t_1)\right)\left[\dfrac{1 - \exp(-K_t t_2)}{1 - \exp(-k_2 t_2)}\right]\end{array}\right) \tag{B.15}$$

Aluminum-Water Vapor zone

$$T = T_{ign} + \frac{\left(T_{ign} - T_{vap}\right)}{1 - \exp\left(-k_3 t_1\right)}\left[\exp\left(k_3 x\right) - 1\right] - \frac{K_a I_f}{\lambda_3\left(K_t^2 - k_3 K_t\right)}\left(\begin{array}{l}\exp\left(K_t x\right) + \exp\left(-k_3 x\right)\left[\dfrac{1 - \exp(-K_t t_1)}{1 - \exp(-k_3 t_1)}\right] + \\ \left[\dfrac{1 - \exp(-K_t t_1)}{1 - \exp(-k_3 t_1)} - 1\right]\end{array}\right) \tag{B.16}$$

Note that the equations become exceedingly complex with the introduction of radiation in the analysis. The thickness of liquid and vapor zones needs to be calculated iteratively by matching the heat flux at the interfacial boundaries, since an analytical form is almost impossible to obtain. By enforcing continuity of heat flux and temperature at the ignition front, the burning rate of the mixture can be calculated.

REFERENCES

Aita KS. Aluminum Combustion: A Model for Nano-Sized Particles. M.S. Thesis. University of Illinois at Urbana-Champaign; 2005.

Alexander CA, Ogden JS, Risser SM, Wood VE. Thermodynamic Characterization of NiAl. Journal of Chemical Thermodynamics. 2009;41(5):610-616.

Allen MP, Tildesley DJ. Computer Simulation of Liquids. New York: Oxford University Press; 1989.

Altman IS. On Heat Transfer between Nanoparticles and Gas at High Temperatures. Journal of Aerosol Science. 1999; 30: S423-S424.

Andersen HC. Molecular Dynamics Simulations at Constant Pressure and/or Temperature. Journal of Chemical Physics. 1980;72(4):2384-2393.

Andrzejak TA, Shafirovich E, Varma A. Ignition Mechanism of Nickel-Coated Aluminum Particles. Combustion and Flame. 2007;150(1-2):60-70.

Aruna ST, Mukasyan AS. Combustion Synthesis and Nanomaterials. Current Opinion in Solid State and Materials Science. 2008;12(3-4):44-50.

Badiola C, Dreizin EL. Combustion of Micron-Sized Particles of Titanium and Zirconium. Proceedings of the Combustion Institute. 2012;34(2):2237-2243.

Badiola C, Gill RJ, Dreizin EL. Combustion Characteristics of Micron-Sized Aluminum Particles in Oxygenated Environments. Combustion and Flame. 2011;158(10):2064-2070.

Badrinarayan B, Barlow JW. Prediction of the Thermal Conductivity of Beds Which Contain Polymer-Coated Metal Particles. In: Proceedings of the Solid Freeform Fabrication Symposium; 1990; Austin. p. 91-98.

Bazyn T, Krier H, Glumac N. Combustion of Nanoaluminum at Elevated Pressure and Temperature Behind Reflected Shock Waves. Combustion and Flame. 2006;145(4):703-713.

Bazyn T, Krier H, Glumac N. Evidence of the Transition from the Diffusion-Limit in Aluminum Particle Combustion. Proceedings of the Combustion Institute. 2007;31(2):2021-2028.

Beckstead MW. Correlating Aluminum Burning Times. Combustion, Explosion, and

Shock Waves. 2005;41(5):533-546.

Beckstead MW, Puduppakkam K, Thakre P, Yang V. Modeling of Combustion and Ignition of Solid-Propellant Ingredients. Progress in Energy and Combustion Science. 2007;33(6):497-551.

Brandes EA, Brook GB. Smithells Metals Reference Handbook. Oxford: Butterworth-Heinemann Ltd; 1992.

Brennen CE. Fundamentals of Multiphase Flow. New York: Cambridge University Press; 2005.

Brooks KP, Beckstead MW. Dynamics of Aluminum Combustion. Journal of Propulsion and Power. 1995;11(4):769-780.

Bucher P, Ernst L, Dryer FL. Detailed Studies on the Flame Structure of Aluminum Particle Combustion. In: Yang V, Brill TB, Ren WZ, editors. Solid Propellant Chemistry, Combustion, and Motor Interior Ballistics. Reston: AIAA; 2000. p. 689-719.

Buckmaster J, Jackson TL. An Examination of the Shrinking-Core Model of Sub-Micron Aluminum Combustion. Combustion Theory and Modelling. 2013; 17(2):335-353.

Buyco EH, Davis FE. Specific Heat of Aluminum From Zero To Its Melting Temperature and Beyond. Equation for Representation of the Specific Heat of Solids. Journal of Chemical and Engineering Data. 1970;15(4):518-523.

Cabrera N, Mott NF. Theory of the Oxidation of Metals. Reports on Progress in Physics. 1949;12(1):163-184.

Choe JI, Kim B. Determination of Proper Time Step for Molecular Dynamics Simulation. Bulletin of the Korean Chemical Society. 2000;21(4):419-424.

Chowdhury S, Sullivan K, Piekiel N, Zhou L, Zachariah MR. Diffusive vs Explosive Reaction at the Nanoscale. Journal of Physical Chemistry C. 2010; 114:9191-9195.

Chung SW, Guliants EA, Bunker CE, Jelliss PA, Buckner SW. Size-Dependent Nanoparticle Reaction Enthalpy: Oxidation of Aluminum Nanoparticles. Journal of Physics and Chemistry of Solids. 2011;72(6):719-724.

Cleri F, Rosato V. Tight-Binding Potentials for Transition Metals and Alloys. Physical Review B. 1993;48(1):22-33.

Connell Jr. TL, Risha GA, Yetter RA, Young G, Sundaram DS, Yang V. Combustion of Alane and Aluminum with Water for Hydrogen and Thermal Energy Generation. Proceedings of the Combustion Institute. 2011;33(2):1957-1965.

Connell Jr. TL, Risha GA, Yetter RA, Yang V, Son SF. Combustion of Bimodal Aluminum Particles and Ice Mixtures. International Journal of Energetic Materials and Chemical Propulsion. 2012;11(3):259-273.

Daw MS, Baskes MI. Embedded-Atom Method: Derivation and Application to Impurities, Surfaces, and Other Defects in Metals. Physical Review B. 1984;29(12):6443-6453.

Delogu F. Demixing Phenomena in NiAl Nanometre-Sized Particles. Nanotechnology. 2007;18(6):065708.

Delogu F. Numerical Simulation of the Thermal Response of Al core/Ni shell Nanometer-Sized Particles. Nanotechnology. 2007;18(50):505702.

Diakov V, Diwan M, Shafirovich E, Varma A. Mechanistic Studies of Combustion-Stimulated Hydrogen Generation from Sodium Borohydride. Chemical Engineering Science. 2007;62(18-20):5586-5591.

Dreizin EL. Experimental Study of Stages in Aluminum Particle Combustion in Air. Combustion and Flame. 1996;105(4):541-556.

Dreizin EL. Metal-Based Reactive Nanomaterials. Progress in Energy and Combustion Science. 2009;35(2):141-167.

Eckert J, Holzer JC, Ahn CC, Fu Z, Johnson WL. Melting Behavior of Nanocrystalline Aluminum Powders. Nanostructured Materials. 1993;2(4):407-413.

Ermoline A, Dreizin EL. Equations for the Cabrera-Mott Kinetics of Oxidation for Spherical Nanoparticles. Chemical Physics Letters. 2011;505(1-3):47-50.

Farber L, Klinger L, Gotman I. Modeling of Reactive Synthesis in Consolidated Blends of Fine Ni and Al Powders. Materials Science and Engineering A. 1998;254(1-2):155-165.

Filippov AV, Rosner DE. Energy Transfer Between an Aerosol Particle and Gas at High Temperature Ratios in the Knudsen Transition Regime. International Journal of Heat and Mass Transfer. 2000;43(1):127-138.

Foley TJ, Johnson CE, Higa KT. Inhibition of Oxide Formation on Aluminum Nanoparticles by Transition Metal Coating. Chemistry of Materials. 2005;17(16):4081-4091.

Foote JP, Thompson BR, Lineberry JT. Advances in Chemical Propulsion. CRC Press; 2002. p. 133-145.

Gale WF, Totemeier TC. Smithells Metals Reference Book. Elsevier; 2004.

Gezelter JD, Rabani E, Berne BJ. Can Imaginary Instantaneous Normal Mode Frequencies Predict Barriers to Self-Diffusion? Journal of Chemical Physics. 1997;107(12):4618-4627.

Glassman I. Combustion. 3rd ed. Orlando: Academic; 1996.

Glassman I, Papas P, Brezinsky K. A New Definition and Theory of Metal Pyrophoricity. Combustion Science and Technology. 1992;83(1-3):161-165.

Gurevich MA, Lapkina KI, Ozerov ES. Ignition Limits of Aluminum Particles. Combustion, Explosion, and Shock Waves. 1970;6(2):154-157.

Hammond WE. Design Methodologies for Space Transportation Systems. Reston: AIAA; 2001.

Henz BJ. Molecular Dynamics Studies of Metallic Nanoparticles. Ph.D. Thesis. University of Maryland; 2009.

Henz BJ, Hawa T, Zachariah M. Molecular Dynamics Simulation of the Energetic Reaction Between Ni and Al Nanoparticles. Journal of Applied Physics. 2009;105(12):124310.

Henz BJ, Hawa T, Zachariah MR. On the Role of Built-In Electric Fields on the Ignition of Oxide Coated Nanoaluminum: Ion Mobility Versus Fickian Diffusion. Journal of Applied Physics. 2010;107(2):024901-024901-9.

Howell JR, Siegel R. Thermal Radiation Heat Transfer. New York:Taylor and Francis;2002.

Huang Y, Risha GA, Yang V, Yetter RA. Combustion of Bimodal Nano/Micron-Sized Aluminum Particle Dust in Air. Proceedings of the Combustion Institute. 2007;31(2):2001-2009.

Huang Y, Risha GA, Yang V, Yetter RA. Effect of Particle Size on Combustion of Aluminum Particle Dust in Air. Combustion and Flame. 2009;156(1):5-13.

Hu R, Nash P. The Enthalpy of Formation of NiAl. Journal of Materials Science. 2005;40(5):1067-1069.

Hultgreen R, Desai PD, Hawkins DT, Gleiser M, Kelley KK. Selected Values of

Thermodynamic Properties of the Elements. Ohio: American Society of Metals; 1973.

Hunt EM, Plantier KB, Pantoya ML. Nano-Scale Reactants in the Self-Propagating High-Temperature Synthesis of Nickel Aluminide. Acta Materilia. 2004;52(11):3183-3191.

Ivanov VG, Gavrilyuk OV, Glazkov OV, Safronov MN. Specific Features of the Reaction Between Ultrafine Aluminum and Water in a Combustion Regime. Combustion, Explosion, and Shock Waves. 2000;36(2):213-219.

Ivanov VG, Leonov SN, Savinov GL, Gavrilyuk OV, Glazkov OV. Combustion of Mixtures of Ultradisperse Aluminum and Gel-Like Water. Combustion, Explosion, and Shock Waves. 1994;30(4):569-570.

JANAF Thermodynamic Tables. 3rd ed. American Chemical Society; 1981.

Jeurgens LPH, Sloof WG, Tichelaar FD, Mittemeijer EJ. Growth Kinetics and Mechanisms of Aluminum-Oxide Films formed by Thermal Oxidation of Aluminum. Journal of Applied Physics. 2002;92(3):1649-1656.

Kittel C. Introduction to Solid State Physics. 8th ed. Wiley; 2004.

Klabunde KJ, Stark J, Koper O, Mohs C, Park DG, Decker S, Jiang Y, Lagadic I, Zhang D. Nanocrystals as Stoichiometric Reagents with Unique Surface Chemistry. Journal of Physical Chemistry. 1996;100(30):12142-12153.

Kotov YA. Electric Explosion of Wires as a Method For Preparation of Nanopowders. Journal of Nanoparticle Research. 2003;5(5-6):539-550.

Kubaschewski O, Alcock CB, Spencer PJ. Materials Thermochemistry. 6th ed. New York: Pergamon Press; 1993.

Kuehl DK. Ignition and Combustion of Aluminum and Beryllium. AIAA Journal. 1965;3(12):2239-2247.

Lai SL, Carlsoon JRA, Allen LH. Melting Point Depression of Al Clusters Generated During the Early Stages of Film Growth: Nanocalorimetry Measurements. Applied Physics Letters. 1998;72(9):1098-1100.

Lemmon EW, Huber ML, McLinden MO. Reference Fluid Properties. National Institute of Standards and Technology; 2007.

Levchenko EV, Evteev AV, Riley DP, Belova IV, Murch GE. Molecular Dynamics Simulation of the Alloying Reaction in Al-Coated Ni Nanoparticle.Computational

Materials Science. 2010;47(3):712-720.

Levenspiel O. Chemical Reaction Engineering. New York: John Wiley and Sons; 1962.

Levitas VI. Burn Time of Aluminum Nanoparticles: Strong effect of the Heating Rate and Melt-Dispersion Mechanism. Combustion and Flame. 2009;156(2):543-546.

Levitas VI, Asay BW, Son SF, Pantoya M. Mechanochemical Mechanism for Fast Reaction of Metastable Intermolecular Composites Based on Dispersion of Liquid Metal. Journal of Applied Physics. 2007;101(8):083524-083524-20.

Levitas VI, Samani K. Coherent Solid/Liquid Interface with Stress Relaxation in a Phase-Field Approach to the Melting/Solidification Transition. Physical Review B. 2011;84(14):140103.

Levitas VI, Samani K. Size and Mechanics Effects in Surface-Induced Melting of Nanoparticles. Nature Communications. 2011;2:284.

Li HP. An Investigation of the Ignition Manner Effects on Combustion Synthesis. Materials Chemistry and Physics. 2003; 80(3):758-767.

Lide DR. Handbook of Chemistry and Physics. New York: CRC Press; 2003.

Liu W, Dupont JN. In-Situ Reactive Processing of Nickel Aluminides by Laser-Engineered Net Shaping. Metallurgical and Materials Transactions A. 2003;34(11):2633-2641.

Lu K, Jin ZH. Melting and Superheating of Low-Dimensional Materials. Current Opinion in Solid State and Materials Science. 2001;5(1):39-44.

Luo S, Ahrens TJ. Superheating Systematics of Crystalline Solids. Applied Physics Letters. 2003;82(12):1836-1838.

Martynenko YV, Ognev LI. Thermal Radiation from Nanoparticles. Technical Physics. 2005;50(11):1522-1524.

Massalski TB. Binary Phase Diagrams. Ohio: ASM International; 1992.

Mcbride BJ, Gordon S. Reference Publication 1311. NASA; 1996.

Mei QS, Lu K. Melting and Superheating of Crystalline Solids: From Bulk to Nanocrystals. Progress in Materials Science. 2007;52(8):1175-1262.

Mills B. 2009 http://en.wikipedia.org/wiki/File:TNT-from-xtal-1982-3D-balls.png.

Mohan S, Ermoline E, Dreizin EL. Pyrophoricity of Nano-Sized Aluminum Particles. Journal of Nanoparticle Research. 2012;14(2):723-728.

Mohan S, Trunov MA, Dreizin EL. Heating and Ignition of Metal Particles in the Transition Heat Transfer Regime.2008;130(10):104505.

Mohan S, Trunov MA, Dreizin EL. On Possibility of Vapor Phase Combustion for Fine Aluminum Particles. Combustion and Flame. 2009;156(11):2213-2216.

Morsi K. Review: Reaction Synthesis Processing of Ni-Al Intermetallic Materials. Materials Science and Engineering: A. 2001;299(1-2):1-15.

Munro M. Evaluated Material Properties for a Sintered Alpha-Alumina. Journal of the American Ceramic Society. 1997;80(8):1919-1928.

Nose S. A Unified Formulation of the Constant Temperature Molecular Dynamics Methods. Journal of Chemical Physics. 1984;81(1):511-519.

Panda S, Pratsinis SE. Modeling the Synthesis of Aluminum Particles by Evaporation-Condensation in an Aerosol Flow Reactor. Nanostructured Materials. 1995;5(7-8):755-767.

Papanicolaou NI, Chamati H, Evangelakis GA, Papaconstantopoulos DA. Second-Moment Interatomic Potential for Al, Ni, and Ni-Al Alloys, and Molecular Dynamics Application. Computational Materials Science. 2003;27(1-2):191-198.

Park K, Lee D, Rai A, Mukherjee D, Zachariah MR. Size-Resolved Kinetic Measurements of Aluminum Nanoparticle Oxidation With Single Particle Mass Spectrometry. Journal of Physical Chemistry B. 2005;109(15):7290-7299.

Parr TP, Johnson C, Hanson-Parr D, Higa K, Wilson K. Evaluation of Advanced Fuels for Underwater Propulsion. In: 39th JANNAF Combustion Subcommittee Meeting; 2003.

Plimpton S. Fast Parallel Algorithms for Short Range Molecular Dynamics. Journal of Computational Physics. 1995;117(1):1-19.

Pokhil PF, Belyaev AF, Frolov YV. Combustion of Powdered Metals in Active Media. Izdatel'stvo Nauka, Moscow 1972.

Press WH, Teukolsky SA, Vetterling WT, Flannery BP. Numerical Recipes in Fortran 77: The Art of Scientific Computing. New York: Cambridge University

Press; 1992.

Price EW, Sigman RK. Combustion of Aluminized Solid Propellants. In: Yang V, Brill TB, Ren WZ, editors. Solid Propellant Chemistry, Combustion, and Motor Interior Ballistics. Reston (VA): AIAA Progress in Aeronautics and Astronautics; 2000.

Puri P. Multi Scale Modeling of Ignition and Combustion of Micro and Nano Aluminum Particles. Ph.D. Thesis. University Park: The Pennsylvania State University; 2008.

Puri P, Yang V. Effect of Particle Size on Melting of Aluminum at Nano Scales. Journal of Physical Chemistry C. 2007;111(32):11776-11783.

Qi Y, Cagin T, Johnson WL, Goddard WA. Melting and Crystallization in Ni Nanoclusters: The Mesoscale Regime. Journal of Chemical Physics. 2001;115(1):385-394.

Rai A, Park K, Zhuo L, Zachariah MR. Understanding the Mechanism of Aluminium Nanoparticle Oxidation. Combustion Theory and Modeling. 2006;10(5):843-859.

Rauscher M, Dietrich S. Nanofluids of Thin Liquid Films. In: Sattler KD, editor. Handbook of Nanophysics. Boca Raton: CRC Press; 2011.

Rhee SK. Wetting of Ceramics by Liquid Aluminum. Journal of American Ceramic Society. 1970;53(7):386-389.

Risha GA, Connell TL, Sundaram DS, Yetter RA, Yang V. Combustion of Frozen Nano-Aluminum and Water Mixtures. Journal of Propulsion and Power. 2013, In Press.

Risha GA, Sabourin JL, Yang V, Yetter RA, Son SF, Tappan BC. Combustion and Conversion Efficiency of NanoAluminum-Water Mixtures. Combustion Science and Technology. 2008;180(12):2127-2142.

Risha GA, Son SF, Yetter RA, Yang V, Tappan BC. Combustion of Nano-Aluminum and Liquid water. Proceedings of the Combustion Institute. 2007;31(2):2029-2036.

Rosenberg M, Smirnov RD, Pigarov AY. On Thermal Radiation From Heated Metallic Dust Grains. Journal of Physics D: Applied Physics. 2008;41(1):015202.

Sabourin JL, Yetter RA, Asay BW, Lloyd JM, Sanders VE, Risha GA, Son SF, Effect of Nano-Aluminum and Fumed Silica Particles on Deflagration and Detonation of Nitromethane. Propellants, Explosives, Pyrotechnics. 2009; 34(5):385-

393.

Saxena SC, Joshi RK. Thermal Accommodation and Absorption Coefficient of Gases. New York: Hemisphere; 1989.

Schlick T. Molecular Modeling and Simulation: An Interdisciplinary Guide. New York: Springer; 2010.

Schoenitz M, Chen C, Dreizin EL. Oxidation of Aluminum Particles in the Presence of Water. Journal of Physical Chemistry B. 2009;113(15):5136-5140.

Sengers JV, Watson JTR. Improved International Formulations for the Viscosity and Thermal Conductivity of Water Substance. Journal of Physical and Chemical Reference Data. 1986;15(4):1291-1314.

Shafirovich E, Diakov V, Varma A. Combustion of Novel Chemical Mixtures for Hydrogen Generation. Combustion and Flame. 2006;144(1):415-418.

Shafirovich E, Escot Bocanegra P, Chauveau C, Gokalp I, Goldshleger U, Rosenband V, Gany A. Ignition of Single Nickel-Coated Aluminum Particles. Proceedings of the Combustion Institute. 2005;30(2):2055-2062.

Shibuta Y, Suzuki T. A Molecular Dynamics Study of Cooling Rate during Solidification of Metal Particles. Chemical Physics Letters. 2011; 502:82-86.

Sundaram DS, Huang Y, Yang V, Risha GA, Yetter RA. Effects of Particle Size and Pressure on Combustion of Nano-Aluminum Particles and Liquid Water. Combustion and Flame, http://dx.doi.org/10.1016/j.combustflame.2013.04.025.

Sundaram DS, Puri P, Yang V. A Phenomenological Theory of Ignition and Combustion of Aluminum Particles. Combustion and Flame, 2013, to be submitted.

Sundaram DS, Puri P, Yang V. Pyrophoricity of Nascent and Passivated Aluminum Particles at Nano-scales. Combustion and Flame, http://dx.doi.org/10.1016/j.combustflame.2013.03.031.

Sundaram DS, Puri P, Yang V. Thermo-Chemical Behavior of Nano-Sized Aluminum-Coated Nickel Particles. Journal of Physical Chemistry C, to be submitted.

Sundaram DS, Puri P, Yang V. Thermo-Chemical Behavior of Nickel-Coated Nanoaluminum Particles. Journal of Physical Chemistry C. 2013;117(15):7858-7869.

Sundaram DS, Yang V, Connell TL, Risha GA, Yetter RA. Flame Propagation of Nano/Micron-Sized Aluminum Particles and Ice (ALICE) Mixtures. Proceedings of the Combustion Institute. 2013;34(2):2221-2228.

Sutton GP, Biblraz O. Rocket Propulsion Elements. New Jersey: John Wiley & Sons; 2010.

Swihart MT. Vapor-Phase Synthesis of Nanoparticles. Current Opinion in Colloid & Interface Science. 2003;8(1):127-133.

Theofanous TG, Chen X, Di Piazza P, Epstein M, Fauske HK. Ignition of Aluminum Droplets Behind Shock Waves in Water. Physics of Fluids. 1994;6(11):3513.

Thiers L, Mukasyan AS, Varma A. Thermal Explosion in Ni-Al System: Influence of Reaction Medium Microstructure. Combustion and Flame. 2002; 131(1-2):198-209.

Ticha G, Pabst W, Smith DS. Predictive Model for the Thermal Conductivity of Porous Materials with Matrix-InclusionType Microstructure. Journal of Materials Science. 2005;40(18):5045-5047.

Tillotson TM, Gash AE, Simpson RL, Hrubesh LW, Satcher Jr. JH, Poco JF. Nanostructured Energetic Materials using Sol-Gel Methodologies. Journal of Non-Crystalline Solids. 2001; 285(1-3):338-345.

Trunov MA, Schoenitz M, Dreizin EL. Effect of Polymorphic Phase Transformations in Alumina Layer on Ignition of Aluminum Particles. Combustion Theory and Modeling. 2006;10(4):603-623.

Tuckerman M. Statistical Mechanics: Theory and Molecular Simulation. USA: Oxford University Press; 2010.

Turkevich J, Stevenson PC, Hillier J. A Study of the Nucleation and Growth Processes in the Synthesis of Colloidal Gold. Discussions of the Faraday Society. 1951;11:55-75.

Umbrajkar SM, Schoenitz M, Dreizin EL. Exothermic Reactions in Al-CuO Composites. Thermochimica Acta. 2006;451(1-2):34-43.

Von Grosse AV, Conway JB. Combustion of Metals in Oxygen. Industrial Engineering and Chemistry. 1958;50(4):663-672.

Woolridge MS. Gas-Phase Combustion Synthesis of Particles. Progress in Energy and Combustion Science. 1998;24(1):63-87.

Yang V. Solid Propellant Chemistry, Combustion, and Motor Interior Ballistics. American Institute of Aeronautics and Astronautics; 2000.

Yetter RA. Private Communication, 2008.

Yetter RA, Dryer FL. Metal Particle Combustion and Classification. In: Ross HD, editor. Micro-Gravity Combustion:Fire in Free Fall. Academic Press; 2001. p. 419-478.

Yetter RA, Risha GA, Son SF. Metal Particle Combustion and Nanotechnology. Proceedings of the Combustion Institute. 2009;32(2):1819-1838.

Young G, Sullivan K, Zachariah M, Yu K. Combustion Characteristics of Boron Nanoparticles. Combustion and Flame. 2009;156(2):322-333.

Zaseck CR, Son SF, Pourpoint TL. Combustion of Micron-Aluminum and Hydrogen Peroxide Propellants. Combustion and Flame. 2013; 160(1):184-190.

Zhang Z, Li JC, Jiang Q. Modelling for Size-Dependent and Dimension-Dependent Melting of Nanocrystals. J. Phys. D: Appl. Phys. 2000;33(20):2653-2656.

Zhang Z, Lu XX, Jiang Q. Finite Size Effect on Melting Enthalpy and Melting Entropy of Nanocrystals. Physica B. 1999;270(3-4):249-254.

Zhuo Y, Karplus M, Ball KD, Berry RS. The Distance Fluctuation Criterion for Melting: Comparison of Square Well and Moore Potential Modes for Clusters and Homo Polymers. Journal of Chemical Physics. 2002;116(5):2323-2329.